

2014

Dielectrophoretic (DEP) Tweezers: New Tool for Molecular Force Spectroscopy

Peng Cheng
Lehigh University

Follow this and additional works at: <http://preserve.lehigh.edu/etd>



Part of the [Chemistry Commons](#)

Recommended Citation

Cheng, Peng, "Dielectrophoretic (DEP) Tweezers: New Tool for Molecular Force Spectroscopy" (2014). *Theses and Dissertations*. Paper 1456.

This Dissertation is brought to you for free and open access by Lehigh Preserve. It has been accepted for inclusion in Theses and Dissertations by an authorized administrator of Lehigh Preserve. For more information, please contact preserve@lehigh.edu.

Dielectrophoretic (DEP) Tweezers: New Tool for Molecular Force Spectroscopy

by

Peng Cheng

A Dissertation

Presented to the Graduate and Research Committee

of Lehigh University

in Candidacy for the Degree of

Doctor of Philosophy

in

Chemistry

Lehigh University

May 2014

© 2014 Copyright
Peng Cheng

Approved and recommended for acceptance as a dissertation in partial fulfillment of the requirements for the degree of Doctor of Philosophy in Chemistry.

“Dielectrophoretic (DEP) Tweezers: New Tool for Molecular Force Spectroscopy,”

by Peng Cheng

April 18th, 2014

Date

Dmitri Vezenov, Dissertation Advisor

Accepted Date

David T. Moore, Committee Member

Jebrell Glover, Committee Member

Daniel Ou-Yang, Committee Member

Table of Contents

List of Figures	vii
List of Tables	xii
Abstract	1
Chapter 1 : Next Generation Sequencing and Highly Parallel Single Molecule Force Spectroscopy	2
1.1 Motivation for development of new single molecule research tool: next generation sequencing	2
1.2 Principle of operation	3
1.3 DEP tweezers as highly parallel molecular force spectroscopy platform	5
1.4 Project goals	9
Chapter 2 : Fabrication and Characterization of Magnetic Fluorescent Polymer Particles using Membrane Emulsification	10
2.1 Introduction	10
2.2 Material and methods	13
2.2.1 Materials	13
2.2.2 Synthesis of Iron-Oleate Complex.	14
2.2.3 Synthesis of Iron Oxide Nanoparticles.	15
2.2.4 Synthesis of CdSe Quantum Dots (QDs)	15
2.2.5 Synthesis of Core/Shell	16
2.2.6 Synthesis of Core/Double Shell	16
2.2.7 Synthesis of Magnetic Fluorescent Polymer Particles Using Membrane Emulsification	16
2.2.8 Characterization	18
2.2.9 Reaction with Surface Carboxyl Groups.	19
2.3 Results and discussion	20
2.3.1 Membrane emulsification	20
2.3.2 Tuning the size of the particles	25
2.3.3 Surface smoothness	26
2.3.4 Fluorescence	27
2.3.5 Super-paramagnetic	29
2.3.6 Surface charges and density of surface functional groups	29
2.3.7 Changing the magnetite concentration	33
2.4 Conclusions	33
Chapter 3 : Single-Molecule-Bead Assemblies for Parallel Single Molecule Force Spectroscopy	35
3.1 Introduction	35
3.2 Approach	37
3.2.1 Control of DNA surface density via competitive binding	39
3.2.2 Tuning the reaction conditions to attach single bead to single molecule	40

3.3 Methods	45
3.3.1 Materials	45
3.3.2 Au NPs synthesis and labeling with a primer	46
3.3.3 Samples for 39-mer DNA attachment via competitive binding	47
3.3.4 Samples for 142-mer DNA attachment and further hybridization	47
3.3.5 Probe binding assays	48
3.3.6 Analysis of fluorescence images	49
3.4 Results and discussion	50
3.4.1 Competitive binding of 39-mer ssDNA with MutEG	50
3.4.2 Fluorescence measurements	51
3.4.3 Surface MutEG/DNA ratio as a function of solution ratio	53
3.4.4 Probe binding assay	55
3.4.5 Ordered single-molecule-bead assemblies	59
3.5 Conclusions	60
Chapter 4 : Dielectrophoretic Tweezers as a Platform for Molecular Force Spectroscopy in a Highly Parallel Format	62
4.1 Introduction	62
4.2 Theoretical background of DEP	64
4.3 System Design	71
4.4 Numerical simulation	74
4.5 Experimental methods	79
4.5.1 Fabrication of the DEP chip	79
4.5.2 Probe fabrication and activation	80
4.5.3 End-modification of DNA	81
4.5.4 Substrate Preparation	82
4.5.5 DEP cell assembly and microscope setup	83
4.6 Results and Discussion	85
4.6.1 Voltage dependence of DEP force	86
4.6.2 Effect of the spacing between two electrodes	87
4.6.3 Frequency dependence of the DEP forces	89
4.6.4 Voltage dependence of the DEP force on probes in microwells	92
4.6.5 Changes in the DEP force magnitude with position of the probe	93
4.6.6 Normal forces.	94
4.6.7 Lateral forces.	98
4.6.8 Measurements of molecular extension	99
4.6.9 Electric field distribution inside a round well in Geometry D.	100
4.6.10 Stretching of single stranded DNA molecules using DEP tweezers	101
4.7 Conclusions	105
4.8 Future directions	107
4.8.1 Reducing the size of force probes.	107
4.8.2 Low magnification objective enables large sample area observation	111
Chapter 5 DEP force calibration and stretching of single DNA molecule	113
5.1 Introduction	113

5.2 Theory	114
5.2.1 Using TIRFM to measure the particle-wall separation distance	114
5.2.2 Potential energy profile	116
5.2.3 Freely jointed chain model of macro-molecule	117
5.3 Methods	120
5.3.1 Evanescent illumination and detection	120
5.3.2 Direct measurement of potential profile	121
5.3.3 Force spectroscopy	121
5.3.4 Data Capture and Analysis	122
5.4 Results and Discussion	122
5.4.1 Force calibration from experimental potential energy profile	122
5.4.2 Calculation of h_m	124
5.4.3 Magnetic Tweezers for DEP force calibration	126
5.4.4 Highly parallel SMFS and analysis of ssDNA stretching	129
5.5 Conclusions	131
Chapter 6 Conclusions	133
References	140
Curriculum Vitae	148

List of Figures

Figure 1.1 In a sequencing-by-synthesis scheme, a base in unknown sequence can be identified by adding a complementary base (A) or short oligomer (B) to a primer resulting in incremental change in the amount of the double stranded DNA by one (A) or 6-9 (B) bases. The sequence is built by controlling the composition of the buffer that contains only one (out possible four) matching substrate (e.g., only ATP in (A) or only NNNANNNN in (B), where N is every combination of DNA bases).	4
Figure 1.2 The forces on the DNA molecule can be generated using either magnetic (top) or DEP (bottom) tweezers. The DNA molecule is immobilized on the surface and bound to the surface of the bead. The contour length of the DNA can be measured at high applied forces. A primer is bound to the ssDNA, which is then polymerized in a stepwise manner. After elongation of the complementary strand, either by using polymerase (single nucleotide addition) or by using ligase (oligomer addition), in the target genomic DNA, the contour length (L_C) of the partially hybridized DNA molecule decreases. n_{primer} is the number of bases in the primer; $n_{oligomer}$ is the number of bases of the oligomer; Δl is the difference in length per base between ssDNA and dsDNA.	6
Figure 2.1 SPG membrane emulsification apparatus setup (right). Cross section view of droplets formation on the pore outlets and flow in continuous phase with applied pressure (left).	18
Figure 2.2 SEM image and fluorescent microscopy image of polymer particles by membrane emulsification (left). Typical distribution of diameters for polymer beads (usually 500 total particles were counted to build the distributions). The fits are the Gaussian distributions.	20
Figure 2.3 Dispersed phase is pressed through the membrane with applied pressure (right). After the droplet has formed on the pore outlet, there are five forces balanced on the droplet.	23
Figure 2.4 Critical pressure decreases with the increases of the mean diameter of the pore size (left). Large not non-spherical particle had been made with too high pressure applied to the system (right).	25
Figure 2.5 (A-C) Microspheres that were made with 4.7 % weight percent of polymer using different pore diameter membranes. (D, F) Microspheres that were made with 2.4 % weight percent of polymer using different pore diameter membranes. When pore diameter decreases, the size of the microsphere decreases. (A & D), (C & F) Microspheres that were made with same pore diameter but different weight percentage of polymer. Lower polymer concentration produces smaller sized particles. A typical size distribution of polymer microspheres with a Gaussian fit.	26
Figure 2.6 (A) Atomic force microscope image of assembled microspheres on the surface of glass slide. (B) A cross-section profile of one of the microspheres.	27
Figure 2.7 Fluorescence spectra of <i>CdSe</i> , <i>CdSe/ZnSe</i> , <i>CdSe/ZnSe/ZnS</i> QDs in toluene (left). Appearance of QD solutions under irradiation with (right top) visible or (right bottom) UV light (325 nm UV lamp) for <i>CdSe</i> , <i>CdSe/ZnSe</i> , <i>CdSe/ZnSe/ZnS</i> QDs.	28
Figure 2.8 (A) The isolated intensity of the beads with organic dye inclusion exponentially decays over time (B) The fluorescent intensity of the beads with quantum dots inclusion drastically increases to the maximum value in a short period of time and follows an much slower exponential decay compared to organic dye.	28
Figure 2.9 There is no observable hysteresis (a). Reconstructed relationship between force and applied field (b & c).	29
Figure 2.10 (A) A reaction scheme to demonstrate that surface functional groups for beads made from (PMMA-MAA) are available for covalent attachment. We used fluorescent dye bearing amino group (tetramethylrhodamine (TAMRA) 5- (and 6-) carboxamide cadaverine) to render nanospheres fluorescent after reaction coupling surface carboxyl groups with amine groups of the dye molecules from aqueous solution. (B) Beads with bulk fluorescence. (C) No fluorophore containing particles reacted to the amino terminated dye molecule on the surface of the particles. Error! Bookmark not defined.	
Figure 2.11 Total intensity is as a function of particle diameter for both bulk fluorescent polymer particle (left) and surface fluorescent polymer particle (right).	32
Figure 2.12 Zeta potential exponentially decreases as a function of increased pH value.	32

- Figure 2.13** Microspheres with 20% (A), 26% (B) and 36% (C) weight percent of magnetite inclusion (A-C). The surface of the microspheres become rougher with the increase of the concentration of magnetite. Particle surfaces remain smooth when concentration of magnetite if not larger than 20%.33
- Figure 3.1** Schematic of minimum spacing of DNA molecules allowable using magnetic tweezers. a) A probe with a diameter of 1 μm and a DNA molecule with a radius of gyration of 11 nm (200-mer ssDNA) would require an intermolecular spacing of approximately 400 nm or greater to ensure only one DNA is attached to the probe. b) Intermolecular spacing can be achieved by competitively binding the DNA with a blocking molecule.36
- Figure 3.2** Chemistry of attachment of a force probe to DNA oligomers anchored at a solid surface. A double stranded DNA (a) is end-modified, denatured, and combined with a thiol blocking molecule for reaction with a gold coated substrate (b). A carboxyl terminated probe is then activated and allowed to come in contact with the probe (c). When in the vicinity of the DNA molecules one of three outcomes may occur (shaded area): (i) the probe and surface will be too attractive and the probe sticks to the substrate, (ii) the probe and surface will be too repulsive and the probe is unable to bind, or (iii) the probe will come close enough to the DNA and covalently link, while not adhering to the surface.38
- Figure 3.3** Representation of a force profile for a probe (microsphere) approaching a surface. To bind to the DNA molecule, the probe must interact with the amine terminal group by passing into the area represented by the blue-gray shaded box. If the probe comes in contact with the surface, it will most likely adhere strongly, so it must not pass completely through the region indicated by a shaded box. The graph shows three representative force-distance profiles as the probe approaches the surface. The repulsive electrostatic force can be too strong and prevent the probe from approaching the target molecule. Conversely, the van der Waals attractive forces can be too strong and cause the probe to stick irreversibly to the surface. If the forces become balanced, the probe will be attracted to the point where it may bind to the DNA, but is repelled at a very close proximity to the surface.41
- Figure 3.4** The effects of tuning the parameters of the system based on DLVO interactions between a polymer bead (4.5 μm diameter) and an organic layer (thiol monolayer) on gold in water. The zero distance is set at the organic layer/water interface. The black curves in each graph represent a standard set of conditions, where ionic strength = 100 mM, zeta potential = 35 mV, blocking layer thickness = 2 nm, the blocking layer-water-probe Hamaker constant = 2 zJ, and the substrate-water-probe Hamaker constant of 15 zJ. The effects of zeta potential (a), ionic strength (b), substrate-water-probe Hamaker constant (c), and the blocking layer thickness (d) were evaluated.45
- Figure 3.5** Microscope images of fluorescent TAMRA-labeled DNA competitively adsorbed with MutEG on an optically-transparent gold substrate followed by passivation by MutEG. Ratios indicate the relative concentration of MutEG to DNA for each image. In the pure DNA sample (0:1), essentially no fluorescent signal is seen before addition of MutEG. A reduction of overall fluorescence signal, a decrease in the size of the peaks, and a decrease in the number of peaks are observed as the MutEG concentration is increased. Images were flattened by fitting the background areas to a 2-D second-order polynomial and subtracting the result from the whole image.52
- Figure 3.6** Scanning Electron Microscopy (SEM) images of competitive adsorption of MutEG and DNA. The relative MutEG and DNA concentrations are 10 (a), 200 (b) and 2000 (c) respectively. The scale bar is 1 μm54
- Figure 3.7** Experiment of competitive adsorption of MutEG and DNA. Competitive kinetics of both mechanism 1 (black-line) and mechanism 2 (red-line) are shown. (a) Plot of DNA parking area versus relative MutEG and DNA concentration. (b) Log plot of nearest neighbor distance versus relative MutEG and DNA concentration.54
- Figure 3.8** Distribution of the single ssDNA oligomers(142 bases) immobilized on Au surfaces is visualized using fluorescent (A) and tapping mode AFM (B) imaging after hybridization with a Cy5-labeled primer (21 bases, complementary to the end opposite to immobilization site). The density of ssDNA is comparable in both images.55
- Figure 3.9** Representative images from bead binding assay. The probes were allowed to settle onto the surface via gravity (left image) and a permanent magnet was used to remove the probes (right image).

This particular experiment was conducted on a SAM of MHDA on gold in a solution of pH 7.0 phosphate buffer with an ionic strength of 1 mM.	56
Figure 3.10 The effects of changing the pH with a constant ionic strength of 1 mM on an MHA surface (a), the solutions ionic strength with a constant pH of 7 on an MHA surface (b), and the surface potential with constant pH of 7 and ionic strength of 1 mM (c). The results of the probe binding assays (c) show the levels of adhesion for the different thicknesses in a series of carboxyl-terminated SAMs (formed by HS-(CH ₂) _n -COOH, n=2, 5, 10, 15) at pH 3.	58
Figure 3.11 Proposed scheme for a force spectroscopy array comprises an array of wells accommodating a single magnetic bead per well, with each bead in turn attached to a single oligomer. Application of a permanent magnet readily forces magnetic beads inside the wells. Plots of intensity (decreasing with distance) vs. current for magnetic tweezers or voltage squared for DEP tweezers (proportional to force) are generated for individual beads. Uneven brightness of the beads in large area images reflects Gaussian intensity distribution in the laser beam illuminating the sample. Variations in the intensity of the neighboring beads reflect differences in their size and exact positioning inside the well.	59
Figure 4.1 Net force on a small physical dipole.	64
Figure 4.2 A small physical dipole suspended in medium with permittivity ϵ_1 . r_+ and r_- are the radius reference to an arbitrary point.	66
Figure 4.3 Dielectric particle with radius R and permittivity ϵ_2 is suspended in dielectric medium with permittivity ϵ_1	67
Figure 4.4 Calculated frequency dependence of the real part of the Clausius-Mossotti factor for a dielectric particle typical to our system ($\epsilon_m/\epsilon_0 = 78, \sigma_m = 10^{-5} \text{S} \cdot \text{m}^{-1}$; $\epsilon_p/\epsilon_0 = 3.0, \sigma_p = 10^{-3} \text{S} \cdot \text{m}^{-1}$). The probe experiences a positive DEP force when the frequency is below 1 MHz, while a negative DEP force acts on a probe when the frequency of applied AC field is above 1 MHz.	70
Figure 4.5 Various cell designs for DEP tweezers. (a) Geometry A: A probe above a flat electrode. (b) Geometry B: A probe in a shallow microwell fabricated on top of an electrode (well depth $h_1 <$ bead diameter). (c) Geometry C: A probe inside a deep microwell fabricated on top of an electrode (well depth $h_2 >$ bead diameter). (d) Geometry D: A microwell on top of a thick gold layer (thickness $t_1=135$ nm), whose primary purpose is to block the light from entering the photoresist layer making layout suitable for TIRFM detection. The thin gold layers (thickness $t_2=14$ nm) act as the electrodes. The standard dimensions for all wells used in this work had $w=4.2 \mu\text{m}$ and $s=24 \mu\text{m}$ (unless varied on purpose). The center-to-center distance for the wells was $44.2 \mu\text{m}$	73
Figure 4.6 Geometry of simulations for a square well in full 3D (a, c) and a round well in reduced 3D (b, c) simulations.	76
Figure 4.7 DEP forces for beads in Geometry C calculated using EDA and MST methods are plotted versus the mesh sizes for 3D simulation with a round well (a) and square well (b). The potential was set to 10 V (peak to peak).	77
Figure 4.8 Both of EDA and MST methods are used for calculation of the DEP force. (a) The DEP force varies as a function of applied potential while the electrode separation was set at $20 \mu\text{m}$. (b) Change in the DEP force with respect to the distance between two electrodes while the applied potential was set at 10 V.	78
Figure 4.9 (a) DEP cell assembly and (b) setup in an optical microscope. The microwell pattern (green) is fabricated on top of the Au-coated glass cover slip (yellow). A sample is sealed with an elastomeric gasket (orange) against Au-coated electrode (yellow) and both are connected to a function generator via copper foil (rectangular yellow pieces). (b) The illumination in transmission mode helped to identify the edges of the microwells. CCD camera captures fluorescent images of the probes from a commercial TIRF setup integrated with a 638 nm laser. (c) Microscope image ($10\times$) of the fluorescent probes assembled inside the microwells.	85
Figure 4.10 Simulation results of DEP force as a function of the electrode separation for probes placed 50 nm above the surface of a flat substrate (\circ), Geometry A, or the bottom of the microwell (\bullet), Geometry C. The parameters used for the simulation were 10 V peak-to-peak voltage with a $3 \mu\text{m}$ diameter probe. The curves represent the power law $F_{DEP} \propto 1/s^2$ for a Geometry A, where $n=1.987\pm 0.001$, and the square of a function in equation (4-23) for a Geometry B.	87

Figure 4.11 The number of polystyrene microspheres remaining on the surface of the electrode as the frequency of the applied AC field is changed from 1 MHz to 1 kHz in DI water or phosphate buffer. The number of probes is normalized to the maximum detected during a given sweep. In the negative DEP regime (high frequency), the number of probes slowly increases in the course of the experiment as more probes approach the surface from the bulk of the solution and accumulate at the surface due to attractive DEP forces. (left inset) TIRF image of a sample of probes when 10 V potential is applied at 200 kHz. The probes overcome the electrical double layer repulsion and land on the surface when the field is turned on. The intensity is high, indicating a close proximity to the surface. (right inset) Image of the same sample at a frequency of 10 kHz (10 V potential). Probes are no longer visible using TIRF microscopy.....	91
Figure 4.12 Simulation results of DEP force acting on a probe which is 50 nm away from the surface as a function of potential applied between two parallel electrodes separated by 24.5 μm for Geometry A (\bullet) and C (\circ). For Geometry A, the line is a power law fit $F_{\text{DEP}}=2.22V^{2.00}$ (where F is in piconewtons, V is volts, standard deviation for both coefficients is $< 0.003\%$). For Geometry C, the line is a power law fit $F_{\text{DEP}}=9.41V^{2.00}$ (where F is in piconewtons, V is volts, standard deviation for both coefficients is $< 0.003\%$).	93
Figure 4.13 Electric field distributions in Geometry A (a-c), Geometry B (d-f), and Geometry C (g-l) for a 3 μm diameter probe at 50 nm (a, d, g, and j) and 3 μm (b, e, h, and k) above the surface of the electrode. When close to the surface, the probe is pulled up ($F_{\text{DEP}} > 0$) by the positive DEP force in (a), (g), and (j), and by the negative DEP in (d). The red streamlines represent the electric field. The surface plots are E^2 and all six graphs share the same scale. (c), (f), (i), and (l) The DEP forces versus distance from the surface when the 3 μm probe is moving away from the electrode.	95
Figure 4.14 Epi-fluorescence images of the probes assembled in wells with Geometry C. (a) The probes are pushed toward the surface by a negative DEP force at high frequency (100 kHz) and (b) levitated above the surface by a positive DEP force at low frequency (1 kHz) ($V_{\text{pp}}=10$ V). The probes go slightly out of focus as indicated by their intensity profiles (c) when the frequency is switched from high (a) to low (b). Small bright spots are beads settled on top of the SU-8 surface between wells. Their positions do not change (c). The solid lines in (c) represent the profiles for 100 kHz AC field, while the dashed lines correspond to 1 KHz.	96
Figure 4.15 (a) The ratio of lateral forces to normal forces as functions of lateral displacement of the probes from the well axis for microwell DEP cell with Geometry B (Figure 2b, \blacktriangle), Geometry C (Figure 2c, \circ), and Geometry D (Figure 2d, \bullet). (b) Blue dashed outlines show the centered position of the probes and the blue arrows show the direction of the normal and lateral forces acting on the probe in each situation (positive or negative DEP). These forces were calculated using a 2D well to reduce calculation time.	98
Figure 4.16 Electric field intensity distribution (\log_{10} scale) inside a well.	101
Figure 4.17 Reaction scheme of the probe and ssDNA attachment to gold electrode.	102
Figure 4.18 (a) TIRF image extracted from a movie of the beads bound to ssDNA molecules attached at low density at the bottom of the wells. The image was taken at 0V (i.e. when the probes were closest to the surface). (b) When the AC voltage amplitude changes from 0 V to 10 V, the brightness of the probe drops approximately 50%, consistent with the probe being pulled away from the surface and the DNA molecule being stretched. (c) Applied potential and raw fluorescence intensity data (normalized to a maximum intensity observed in a given trace) versus time for three beads circled in part (a). Intensity traces are shifted with respect to each other for clarity.	104
Figure 4.19 The DEP forces versus distance from the surface when the 40 nm probe is moving away from the electrode.	108
Figure 4.20 SMFS using Au nanoparticles in a DEP fluid cell. (A) Thiol terminated cDNA primers are first introduced on the surface using competitive binding chemistry. Gold nanoparticles, functionalized with the target DNA strand, are then added to a surface containing cDNA. (B) After hybridization, a DEP force can be used to stretch the single DNA strand, while measuring its extension using TIR-scattering from the Au nanoparticle. (C) Experimental image of a dilute solution of 17 nm diameter gold nanoparticles in a fluid cell (20x magnification, TIR-illumination).	111

Figure 4.21 (A) The incident light undergoes total internal reflection at glass-water interface in a planar-waveguide implementation of a force spectroscopy array. Forward scattering of the evanescent field by dielectric microspheres maps their distance from the surface of the waveguide. (B) We used 10× objective to capture the intensity of light scattered by beads.	112
Figure 5.1 When transmitted angle is larger than critical angle, evanescent wave is generated. The intensity of electric field drops exponentially as a function of the distance from the interface.	115
Figure 5.2 Many Kuhn segments freely jointed as a chain. Every segment has can be freely rotated.	118
Figure 5.3 Two conformations of DNA backbone.	119
Figure 5.4 Histogram of fluorescent intensity (left) and potential energy profile (right).	123
Figure 5.5 Autocorrelation function of fluorescent intensity (left) and apparent diffusion coefficient as a function of most probable position (right).	126
Figure 5.6 The forces on the DNA molecule can be generated using either magnetic (A) or DEP (B) tweezers. The 200-base long ssDNA molecule is immobilized on the surface and bound to the surface of the bead. When the magnetic or DEP force is applied (via coil current or AC voltage amplitude changes – top panels), the brightness of the probe fluorescence in the evanescent field drops by approximately 50%, consistent with the probe being pulled away from the surface and the DNA molecule being stretched.	127
Figure 5.7 Direct comparison of the DNA stretching curves obtained with DEP tweezers (A) and magnetic tweezers (B) using the same superparamagnetic bead-ssDNA pair. Both experiments used a bead positioned inside a microwell and illuminated by the evanescent wave. Since the decrease in the probe intensity for both DEP and magnetic tweezers is the same, the range of forces achieved in the two molecular tweezers arrangements should also be the same.	128
Figure 5.8 Force spectroscopy of ssDNA conducted using DEP tweezers on a system optimized using design principles based on results from this paper. Force probes tethered to DNA in wells before (a) and after (b) they were exposed to a DEP force. Free force probes settled in wells before (c) and after (d) the DEP force was applied. The brightness of the probes (a-d) varies due to Gaussian profile of the illumination laser beam and variations in the bead sizes. (e) A single frame from a movie of the probes, showing the indexing of the force probes for data analysis. (f) A representative intensity vs. voltage plot for one probe. (g) Fits of the data from the plot in part f.	130

List of Tables

Table 6.1 Comparison of current single-molecule force spectroscopy methods with DEP Tweezers.....	135
--	-----

Abstract

Many recent advances in DNA sequencing technology have taken advantage of single-molecule techniques using fluorescently-labeled oligonucleotides as the principle mode of detection. In spite of the successes of fluorescent-based sequencers, avoidance of labeled nucleotides could substantially reduce the costs of sequencing. This dissertation will describe the development of an alternative sequencing method, in which unlabeled DNA can be manipulated directly on a massively parallel scale using single molecule force spectroscopy. We demonstrated that a combination of a wide-field optical detection technique (evanescent field excitation) with dielectrophoretic (DEP) tweezers could determine the amount of the double-stranded character of DNA. This thesis discusses all aspects of the implementation of DEP tweezers, including the principle of operation, making of polymer force probes, numerical modeling of various designs, fabrication of electrode and disposable chip, force calibration, and the assembly of the device. The feasibility of this technique was demonstrated by conducting force spectroscopy on single DNA molecules using DEP tweezers. The development of such a single molecule force spectroscopy technique shows great potential for genome sequencing and other analytical applications that employ direct manipulation of biomolecules.

Chapter 1 : Next Generation Sequencing and Highly Parallel Single Molecule Force Spectroscopy

1.1 Motivation for development of new single molecule research tool: next generation sequencing

The progress in DNA sequencing technology has been remarkable in the past decade, largely driven by the potential medical importance of the availability of low cost human genomes for use in personal genomics.¹⁻³ Low cost rapid sequencing requires miniaturization of the sequencing platforms, which, in turn, leads to orders of magnitude reductions in the amounts of reagents and time needed to run sequencing reactions. The ultimate sample size in any analysis is represented by a single molecule. It is natural, therefore, to see single molecule based techniques at the heart of many emerging sequencing technologies.⁴⁻¹²

The two most widely used general approaches in analysis or detection of single molecules are the measurements of fluorescence and forces (i.e. force spectroscopy). In addition, sensing of DNA translocation through nanopores has received a lot of attention in the context of genome sequencing.¹³⁻¹⁶ So far only the fluorescence in various formats has been exploited for the purposes of the next generation sequencing technology.^{4, 6, 7, 17} This disparity is due to the fact that fluorescence is a wide-field technique, whereas most advanced high resolution force spectroscopy techniques use a serial, one-molecule-at-a-time approach (for example, as in atomic force microscopy, where a molecule is manipulated by a nanoscopically-sharp probe controlled by a system of relatively

complicated electronics and motion hardware that requires involved alignment and noise isolation).¹⁸⁻²³ Highly localized detection volumes require long processing time of many experiments, making this approach not suitable for the manipulation of the millions of segments of DNA required to sequence the 3 billion base pair human genome.

Use of non-fluorescence approaches will eliminate specially designed, and often costly, DNA-processing enzymes and fluorescently labeled reagents in favor of common natural enzymes and substrates and should contribute to lowering the final cost of sequencing. We have proposed a sequencing strategy that uses force spectroscopy to detect the conformational changes of DNA in the course of a stepwise polymerization reaction (either via addition of a single base or ligation of a short oligomer). This approach queries the composition of the DNA strand by mechanically stretching individual molecules to determine the success or failure of the addition of a base pair complement (as in sequencing by synthesis) through differentiation of the physical characteristics of double and single stranded DNA. To ensure that such analysis can be practiced on systems of many molecules, we developed a highly-parallel single molecule force spectroscopy platform using dielectrophoretic (DEP).^{24, 25} In this chapter, we review the principles of proposed mechanical sequencing of DNA, and the fundamental components of DEP tweezers.

1.2 Principle of operation

Mechanical approaches to sequencing exploit the physical differences in conformations of single and double stranded DNA.^{26, 27} The molecular size (contour

length) of the single stranded DNA (ssDNA) is dramatically different from the double stranded DNA (dsDNA): 0.58 nm versus 0.34 nm per base, e.g. replicating a 200 base long strand results in a change of the end-to-end distance of about 35-40 nm, if measured at high loading forces (>20 pN). Therefore, addition of complementary nucleotides by polymerase or complementary DNA oligomers by ligase could be detected by acquiring a force-extension curve and determining the number of bases in a double stranded form that would be required to describe the elastic properties of a given DNA molecule. Consequently, instead of observing a specific fluorescent label during successful incorporation of a complementary base, one can quantify the double-stranded character of a single DNA molecule and detect events of binding a single nucleotide (or oligomer) by repeatedly recording single molecule stretching curves (Figure 1.1).

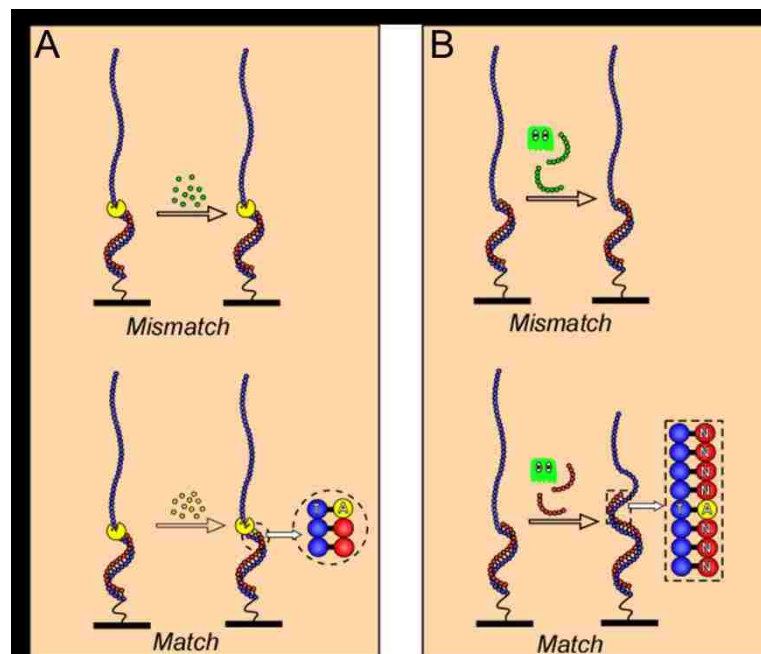


Figure 1.1 In a sequencing-by-synthesis scheme, a base in unknown sequence can be identified by adding a complementary base (A) or short oligomer (B) to a primer resulting in incremental change in the amount of the double stranded DNA by one (A) or

6-9 (B) bases. The sequence is built by controlling the composition of the buffer that contains only one (out possible four) matching substrate (e.g., only ATP in (A) or only NNNANNNN in (B), where N is every combination of DNA bases).

1.3 DEP tweezers as highly parallel molecular force spectroscopy platform

To achieve manipulation of many molecules, one can attach a microscopic force probe (polymer bead with surface functionality) to each DNA strand and apply a force field, to pull on these probes, thus generating force versus extension curves for multiple DNA molecules in parallel. A uniform magnetic field gradient,^{28, 29} which is typically used for this purpose, can be set up over relatively large areas (0.01-1 mm²). An electric field gradient can, in principle, even be set up on flat electrodes and, therefore, uniform force field can be generated over even larger areas (cm²). A response from multiple force probes can be observed simultaneously using wide field microscopy. Given that the differences in the contour length of DNA on the order of 0.3 nm must be detected, the detection system should be highly sensitive (at sub-nanometer level) and differential (i.e. measuring the distance between two termini of the molecule rather than absolute positions of the two ends) to avoid problems of mechanical noise and drift. The system for force application and size measurement should ideally be self-referencing to remove concerns about calibration and repeatability.

We have combined evanescent wave excitation scheme with magnetic tweezers to build such a highly parallel force spectroscopy platform.³⁰ The sequencing scheme using magnetic tweezers (Figure 1.2 top left) is based on detection of a decrease in the overall contour length of the target strand being sequenced. When the magnetic field is applied to

superparamagnetic probes, the probes move vertically and the movements of the probes are measured by integrating the fluorescent intensity of the probes that are presented in the evanescent field. When the molecules are extended by the probe, the changes in the distance of the bead from the surface manifest themselves as changes in intensity of the fluorescent bead image (i.e. a lower intensity indicates a lower magnitude of the evanescent field and, therefore, a greater distance). The exponential distance dependence of the evanescent field, on the one hand, makes this technique extremely sensitive to small changes in conformations, on the other hand, it limits the method to relatively short molecules (<200 nm), setting the upper limit for the length of a DNA molecule of interest at several hundred bases (300-400).

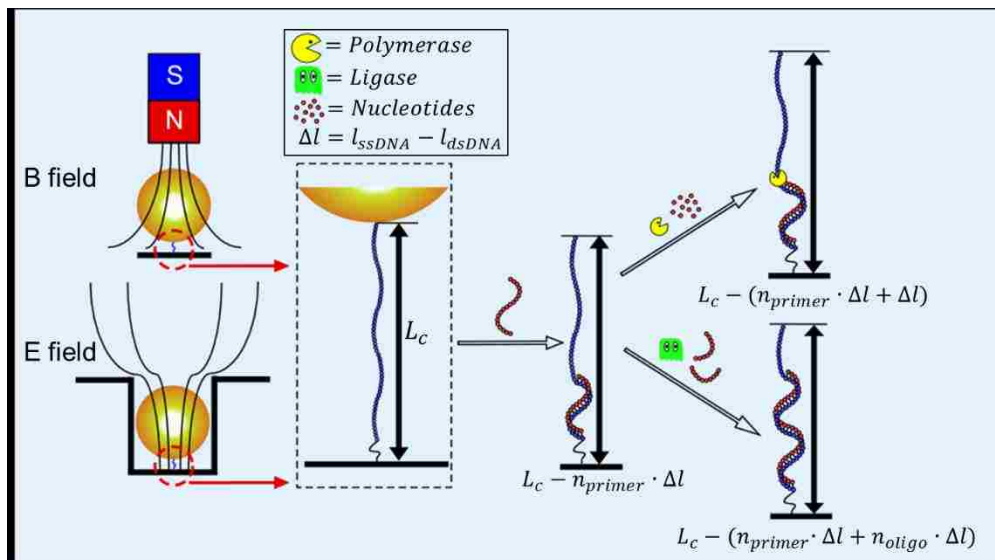


Figure 1.2 The forces on the DNA molecule can be generated using either magnetic (top) or DEP (bottom) tweezers. The DNA molecule is immobilized on the surface and bound to the surface of the bead. The contour length of the DNA can be measured at high applied forces. A primer is bound to the ssDNA, which is then polymerized in a stepwise manner. After elongation of the complementary strand, either by using polymerase (single nucleotide addition) or by using ligase (oligomer addition), in the target genomic DNA, the contour length (L_c) of the partially hybridized DNA molecule decreases.

n_{primer} is the number of bases in the primer; n_{oligo} is the number of bases of the oligomer; Δl is the difference in length per base between ssDNA and dsDNA.

We chose evanescent wave excitation, because it does not require imaging the force probes with high lateral resolution and, in principle, can be implemented with low magnification objectives and with only a few pixels dedicated to each molecule-probe pair (since one needs integrated intensity, low lateral resolution is actually a benefit, because integration is then implemented in the hardware). The method is inherently differential by design (measures difference in position of the bead with respect to the solution-solid interface), thus, negating adverse drift effects for short acquisition times.

The main challenge in building a sequencing platform based on direct manipulation of single DNA molecules as envisioned above is developing a highly parallel single molecule force spectroscopy platform (SMFS). Since genomic DNA is 3 billion base pairs long, sequencing would require the analysis of approximately 10 million DNA strands in parallel. A force spectroscopy platform designed for this purpose would require immense scalability. The second arises with the length change of only 0.24 nm/base pair with the addition of a single base. A system must be designed in which the lowest amount of bases could be ligated at once while staying within the limits of detection for the technique.

To meet the need of “true” highly parallel for genome sequencing purpose, we developed an approach to direct manipulation of nano- or microscopic probes using dielectrophoresis (DEP). DEP refers to the force exerted on the induced dipole moment

of a dielectric particle by a nonuniform electric field. The magnitude and direction of DEP force can be manipulated by controlling the amplitude and frequency of the electric field. In DEP tweezers, the force on the microscopic probes is applied evenly to all the probes in the system. This effect is achieved by *perturbing the homogeneous electric field with dielectric microstructures* in order to generate DEP forces, up to several hundred piconewtons, acting on microscopic probes across a macroscopic (cm²) sample area. Fabrication of the interdigitated microelectrodes is not required.

The other critical aspect in building a sequencing platform based on direct manipulation of single DNA molecules is the fabrication of high-density arrays of DNA-force probe assemblies to ensure parallelism. The array is constructed by attaching the DNA strands with one end to the surface of a rigid support and, at the opposite termini, to the microscopic force probe. We chose covalent chemistry to assemble single-molecule with single-probe. We fabricated fluorescent polymer beads with surface functionality to covalently bind the beads to one end of the DNA molecules. The other end of the DNA molecules are bound to the surface using self-assembled monolayer. We tune the surface chemistry and reaction conditions for bead attachment to fabricate a high efficiency, high density single-molecule-bead array.

While there are many potential applications of the proposed approach to single molecule interrogation, we will only discuss a representative demonstrations, detection of ssDNA elasticity, while focusing on methodological aspects of enabling the science behind this approach. The scope of this dissertation is to understand the fundamental

design criteria of the DEP tweezers platform for SMFS where one obtains statistically significant large data sets at low cost and high speed without jeopardizing the resolution.

1.4 Project goals

This dissertation will discuss all aspects of the implementation of DEP tweezers in the following chapters. Including: i) fabrication and characterization of multifunctional force probes; ii) an optimized method for single-molecule-bead assembly; iii) numerical modeling and fabrication of various designs; iv) calibration of DEP force and a demonstration of force-extension curves on ssDNA molecules. We will finally discuss other potential applications of DEP tweezers in the conclusions chapter.

Chapter 2 : Fabrication and Characterization of Magnetic Fluorescent Polymer Particles using Membrane Emulsification

2.1 Introduction

Molecular force spectroscopy is a widely used single molecule analysis method for studying inter/intra molecular forces.³¹⁻³³ Magnetic tweezers is one of the most popular methods due to its low cost and promise of parallel format.^{30, 34, 35} Several classes of nano- and microscale particles with combined functionality, such as magnetism,³⁶⁻³⁸ variable refractive indices, and fluorescence³⁹ have been proposed for use as force probes in magnetic tweezers setup. In addition, these multi-functional particles are currently receiving wide-spread attention because of their potential new applications in biosensing, diagnostics, and delivery of therapeutic agents.

There are several desired characteristics for nano- and microscopic particles as force probes in magnetic tweezers setup. 1) The surface of the particle needs to be smooth. Since the sizes of the single molecules are much smaller than the sizes of the force probes, rough surface of the force probe can offset the measurement of molecular size. 2) The concentration of magnetite included in the particle needs to be maximized. The magnitude of the magnetic force applied to the force probe is proportional to the field gradient and total magnetite loading. 3) To achieve high spatial resolution, one can use fluorescent particles and total internal reflection fluorescence (TIRF) to detect changes of molecular extension from probe position. 4) Tunable surface chemistry is required for binding different molecules to the surface of the probe. 5) Ability to fabricate

various particles of different diameters having low distribution width can offer us flexibility in the design of magnetic tweezers and other applications.

Typical approaches to fabrication of such complex probes rely on a bottom-up synthetic strategy: start with a nanoparticle having desired properties and then grow a shell of a second material. Alternatively, one can disperse a reactant in a liquid matrix, which is then solidified by polymerization and in *situ* nanoparticles synthesis to encapsulate several types of nanoparticles in a single complex particle. The surface of the matrix can be modified further, for example, for the purposes of chemical conjugation to biological targets. Micro- and nanoparticles based on polymers,⁴⁰⁻⁴⁶ and inorganic oxides^{47, 48} (such as seen a major focus of such synthetic approaches, because polymers and oxides can serve as inert vehicles for nanoparticles and optically active organic molecules in biologically relevant applications. These methods, while diverse, have the disadvantage of being elaborate, using long (from several hours to days) polymerization time, and having limited range of control of the ultimate composition and properties of the probes. Versatility of future applications of these complex probes will benefit from synthetic methods that are readily accessible and general.

In this chapter, I describe a one-step approach to fabrication of polymer micro-particles that contain both fluorescent and magnetic inclusions. We have developed a new reaction scheme that relies on a top-down “mix and squeeze” approach to produce, in a matter of tens of minutes, gram quantities of high-quality polymer micro-particles of predesigned composition and properties. We used membrane emulsification to produce micron sized poly(methyl methacrylate) (PMMA) particles that contain magnetic and

fluorescent components – magnetite (Fe_3O_4) nanoparticles and core-shell quantum dots (CdSe/CdS or CdSe/ZnSe/ZnS) or organic dyes. These composite particles were prepared in high yields from solutions of the bulk polymers and have diameters ranging from 800 nm to several micrometers depending on the porous membrane used in the synthesis.

Dispersion of magnetite nanoparticles in solid matrix renders the particles superparamagnetic, i.e. they exhibit large magnetization, but only in the presence of a magnetic field. Oxides have an advantage over zero valent ferromagnetic metals (e.g. Fe) due to their stability in an ambient environment, whereas metal nanocrystals can undergo rapid oxidation into a non-ferromagnetic form. Magnetite nanoparticles have been demonstrated for applications ranging from biomolecular separations⁴⁹ and medical applications⁵⁰ to materials for data storage media.⁵¹

Quantum dots have unique optical and electronic properties such as emission of light with size-tunable wavelength, improved brightness and resistance to photobleaching compared to organic fluorophores, and allow for simultaneous excitation of multiple fluorescent colors (each from a population of QDs of different size or composition). These properties are well suited for applications in multiplexed optical encoding,⁵² living cell biology⁵³, sensing⁵⁴, and microelectronics.⁵⁵

Polymers can provide a rigid matrix to embed a controllable and easily variable amount of these nanomaterials (e.g. nanoparticles, nanotubes, and nanowires) or molecular species (e.g. organic fluorophores) uniformly throughout the volume of the nano- or microsphere. Surprisingly, to date there are only a handful of reports that describe simultaneous embedding of fluorescent and magnetic materials in a polymer

matrix. Recently, Sun *et al.* reported the fabrication of fluorescent and magnetic polystyrene microspheres with carboxyl termination. Emulsion and seed polymerization were used in making those microbeads followed by extraction to generate pores for nanoparticles; however, the procedure took over 5 days and resulted in beads with rough surfaces.

Our composite micro-particles with narrow size distribution have several advantages compared to those reported previously or available from commercial sources: 1) they possess smooth surfaces; 2) they are easily prepared from bulk polymers with reaction times on the order of tens of minutes; 3) they have tunable composition and the method is readily extendable to multiple components for encapsulation (i.e. more than two distinct inclusions described here); 4) several terminal functional groups on the particle surface can be introduced by means of the appropriate choice of the polymer. We use these multi-functional micro-particles in our magnetic/DEP tweezers experiments and they are suited for other potential applications requiring multifunctionality (magnetic and fluorescence)

2.2 Material and methods

2.2.1 Materials

Tri-n-octylphosphine oxide (TOPO), Tri-n-octylphosphine (TOP), octadecylamine (ODA), 1-Octadecene (ODE), Cadmium oxide (CdO), di-n-octyleamine (DOA), selenium power (325 meshes) and sulfur were purchased from Alfa-Aesar. Zinc undecylenate ($Zn(UD)_2$) was purchased from Pfalt & Bauer. Stearic acid (SA),

poly(methyl methacrylate) (PMMA MW=15000), poly(methyl methacrylate co-methacrylic acid) (PMMA co MAA, MW=34000), *N*-hydroxysuccinimide (NHS), dimethylaminopropyl)-*N*'-ethylcarbodiimide (EDC), iron chloride($\text{FeCl}_3 \cdot 6\text{H}_2\text{O}$), fluorescence, Rhodamine 6G and oxazine-1 were purchased from Aldrich. 4-dimethylamino-4'-nitrostilbene, sodium oleate, oleic acid, 1-octadecene, and perylene was purchased from VWR. Sodium dodecyl sulfate (SDS) was purchased from J.T.Baker. Tetramethylrhodamine 5 - (and - 6) – carboxamide cadaverine (NH_2 -TAMRA-C) was purchased from AnaSpec Inc. Commercial ferrofluid (MagnaView Fluid) - a colloidal suspension of magnetite nanoparticles (~10 nm diameter) in hexane was purchased from United Nuclear Scientific. Magnetite was purified from unknown organic residue. The magnetite nanoparticles were precipitated with ethanol and washed with hexane and chloroform. The magnetite was repeated several times and then dried under high vacuum at room temperature. All other chemicals used were of reagent grade.

2.2.2 Synthesis of Iron-Oleate Complex.

The metal–oleate complex was prepared by reacting metal chlorides and sodium oleate. In a typical synthesis of iron–oleate complex, 10.8 g of iron (III) chloride ($\text{FeCl}_3 \cdot 6\text{H}_2\text{O}$, 40 mmol) and 36.5 g of sodium oleate (120 mmol) was dissolved in a mixed solvent composed of 80 mL ethanol, 60 mL distilled water, and 140 mL hexane. The resulting solution was heated to 70 °C and kept at that temperature for four hours. When the reaction was completed, the upper organic layer containing the iron–oleate complex was washed three times with 30 mL of distilled water in a separation funnel.

After washing, hexane was evaporated off, resulting in iron–oleate complex in a waxy solid form.

2.2.3 Synthesis of Iron Oxide Nanoparticles.

The following is a typical synthetic procedure for monodisperse iron oxide (magnetite) nanocrystals with a particle size of 12 nm. 36 g (40 mmol) of the iron-oleate complex synthesized as described above and 5.7 g of oleic acid (20 mmol) were dissolved in 200 g of 1-octadecene at room temperature. The reaction mixture was heated to 320 °C with a constant heating rate of 3.3 °C min⁻¹, and then kept at that temperature for 30 min. When the reaction temperature reached 320 °C, a severe reaction occurred and the initial transparent solution became turbid and brownish black. The resulting solution containing the nanocrystals was then cooled to room temperature, and 500 mL of ethanol was added to the solution to precipitate the nanocrystals. The nanocrystals were separated by centrifugation.

2.2.4 Synthesis of CdSe Quantum Dots (QDs)

The synthesis of the photoluminescent core/shell nanoparticles was adopted from a reported procedure.⁵⁶ Before reaction, the flasks and the condenser were purged with N₂ gas and the synthesis was conducted under a dry N₂ environment. 257.0 mg (2.0 mmol) of CdO and 2.775 g (8.0 mmol) of stearic acid were heated to 250 °C. The heated mixture formed transparent solution with pale yellow color. The mixture was cooled to room temperature, and then 80 mL of 1-octadecene, 10 g of TOPO, and 10g of octadecylamine were added. The mixture was then heated to 300 °C. 10 mL of 1.0 M TOPSe prepared by

mixing 10 mL TOPO and 789.0 mg of Se powder in glove box was injected into the mixture with a syringe. The temperature was decreased to 280 °C and maintained for 5 min for the growth of the core. After cooling the mixture to RT, about 10 mL of the crude mixture was extracted for characterization.

2.2.5 Synthesis of Core/Shell

CdSe/ZnSe QDs. Without separation of the core QDs, the CdSe core reaction mixture was cooled to RT and 0.4 M Zn(UD)₂ dissolved in 50 mL of DOA was quickly injected. The temperature of the mixture was slowly increased to 240 °C and maintained for 30 min to grow ZnSe shell. Then the mixture was cooled to RT, and about 10 mL of the crude mixture was extracted.

2.2.6 Synthesis of Core/Double Shell

CdSe/ZnSe/ZnS QDs. After cooling CdSe/ZnSe core/shell crude reaction mixture to RT, 3.0 mmol of sulfur dissolved in 50 mL of ODE was quickly injected. The temperature was increased to 240 °C, and the shell growth was allowed to proceed for 2 hrs.

2.2.7 Synthesis of Magnetic Fluorescent Polymer Particles Using Membrane

Emulsification

The scheme of an apparatus is shown in Figure 2.1. The dispersed oil phase was prepared by mixing the following stock solution: 3 mL of 4.7% (w/w) of poly(methyl methacrylate co-methacrylic acid) (PMMA co MAA, MW=34000), 1 mL of 166 g/L solution of magnetite in chloroform, and 0.1 mL of 4.12 g/L of solution of quantum dots

in chloroform (or 0.01 mL of 0.005 M of organic dye in chloroform). The dispersed phase was homogenized using Vortex and/or bath sonicator. The prepared chloroform solution was immediately transferred to the oil tank on the SPG membrane emulsification apparatus (SPG Technology Co., Ltd, Miyazaki-city, Japan).

To find the critical pressure (P_c), we set the pressure to a high value (above P_c) and closed the pressure gauge in order to obtain a closed system. Then we recorded the pressure of the system through time until the pressure was relatively steady. We used the steady state value, as an estimate of critical pressure, since it is the minimum pressure, which can push the dispersed phase from the oil tank through the membrane into continuous phase.

The SPG membrane emulsification was initiated by setting the pressure above the oil phase with nitrogen gas so that the critical pressure was exceeded by 2~5 kPa. The dispersion phase was created in a 300 mL beaker containing 200 mL of a 1 % sodium dodecyl sulfate (SDS, T.J.Baker) aqueous solution and heated in the 40 °C water bath subject to mechanical stirring. Reaction time depended on the initial volume of the dispersed phase (from 0.9 ml to 5 ml). After completion of reaction, the mixture was stirred for additional 1 hour without heating to ensure removal of chloroform. The suspension of the particles remains stable in 1% surfactant solution for weeks and months. For further analysis of these particles, excessive amount of surfactant was removed by washing the reaction mixture several times with 1%, 0.1 % SDS solution, and deionized water with separation of beads by centrifugation in each step.

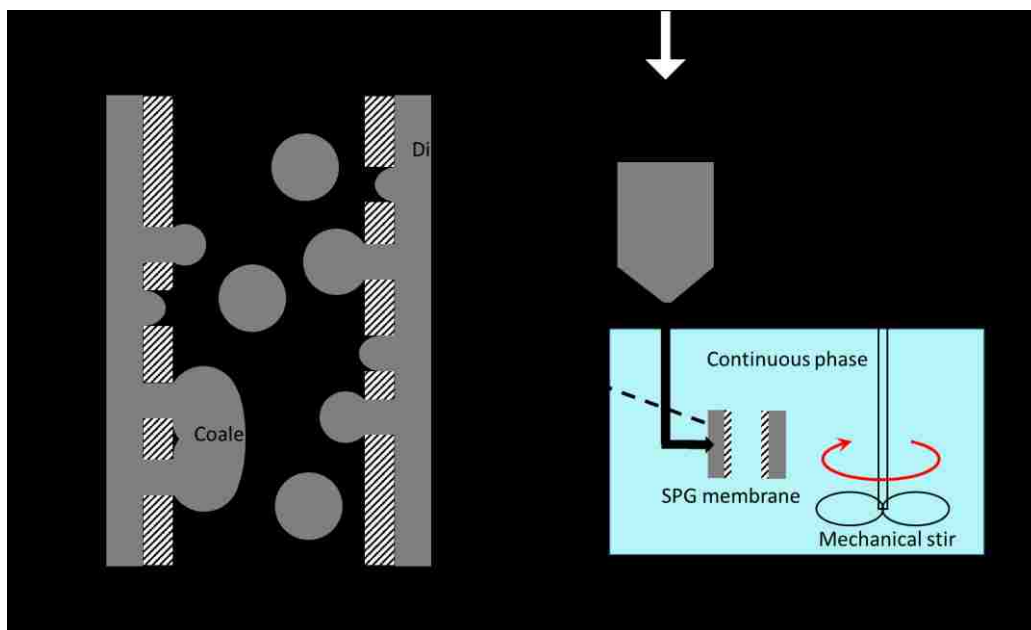


Figure 2.1 SPG membrane emulsification apparatus setup (right). Cross section view of droplets formation on the pore outlets and flow in continuous phase with applied pressure (left).

2.2.8 Characterization

The morphology and surface smoothness of the product were examined, respectively, by the field-emission scanning electron microscopy (FESEM) (Hitachi 4300 at an accelerating voltage of 3-5 kV) and atomic force microscopy (Asylum Research, MFP3D-BIO).

Fluorescence and UV-VIS spectrophotometry (Cary Eclipse, Varian, and UV-2101 PC, Shimadzu) were used to take the fluorescence or adsorption spectra of quantum dots. An epi-fluorescence microscope (Olympus IX 71) was used to observe fluorescence of the products using Fluorescein Iso-ThioCyanate (FITC) and Tetramethyl Rhodamine Iso-ThioCyanate (TRITC) filter cubes. A ZetaPALS Zeta Potential Analyzer (with zeta

cell cuvettes) from Brookhaven Instrument Corporation was used for measuring zeta potentials of polymer particles. We used vibrating sample magnetometer (Lake Shore Cryotronics, Inc) to characterize hysteresis loop of the magnetic fluorescent polymer particles.

2.2.9 Reaction with Surface Carboxyl Groups.

After removing extra SDS from the PMMA-COOH non-fluorescent particles by washing with distilled water several times, 10 mg of 1mM solution of *N*-hydroxysuccinimide (NHS) and *N*-(3-dimethylaminopropyl)-*N'*-ethylcarbodiimide (EDC) were added into the particle suspension in water. The mixture was shaken for 1 hour. EDC reacts with a carboxyl groups on the particle's surface, forming an amine-reactive *O*-acylisourea intermediate. The addition of NHS (1 mM) stabilizes the amine-reactive intermediate by converting it to an amine-reactive NHS ester, thus, increasing the efficiency of EDC-mediated coupling reactions. This amine-reactive NHS ester reacts with an amine of NH₂-TAMRA-C dye. After washing with water several times to remove unreacted reagent, the *O*-acylisourea intermediate particles were reacted with 1 mM of NH₂-TAMRA-C for 1 hour with gentle shaking. After washing with distilled water several times, the particles were characterized by fluorescent microscopy. In a control experiment, PMMA-COOH particles without EDC and sulfo-NHS activation were examined with the same procedure.

2.3 Results and discussion

Using membrane emulsification method, we encapsulated magnetic and fluorescent nanoparticles in the PMMA-based polymer particles. Figure 2.2 shows typical SEM and fluorescent microscopy images of the fabricated polymer macro-particles. The beads are uniformly round with smooth surfaces and have a range of diameters from 2.8 μm to 3.2 μm . In analysis of the size distribution, instead of using model sensitive methods (e.g. dynamic light scattering), we opted for counting the particles in the SEM images to avoid ambiguity. The shape of the size histogram in Figure 2B is best described by Gaussian distribution. Polydispersity values D_n/D_v (ratio of number average to volume diameters) clustered around 1.2.

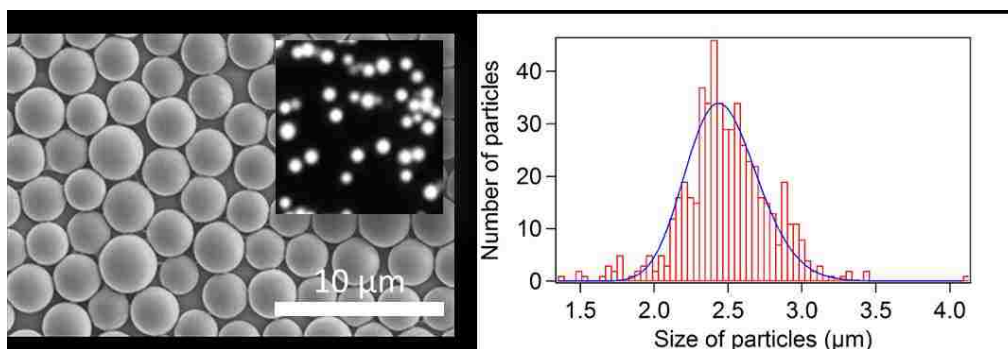


Figure 2.2 SEM image and fluorescent microscopy image of polymer particles by membrane emulsification (left). Typical distribution of diameters for polymer beads (usually 500 total particles were counted to build the distributions). The fits are the Gaussian distributions.

2.3.1 Membrane emulsification

The general idea of membrane emulsification is to applying a relatively low pressure to force the dispersed phase to permeate through a micro-porous membrane into

the continuous phase. Compared to other emulsification methods, where droplets are formed by forcing turbulent droplet break-up, the unique feature of membrane emulsification is that the droplet size is mainly determined by the pore size of the membrane. This method can be used to generate both oil-in-water (O/W) and water-in-oil (W/O) emulsions by choosing membranes of different hydrophobicity.

As we indicated on Figure 2.1, the droplets can be merge on the surface of the membrane. Thus, the droplet size distribution is determined not only by the pore size, but also the degree of coalescence, both on the surface of a membrane and in the continuous phase.

We chose to use a Shirasu Porous Glass (SPG) membrane, which is known to have uniform micro-pores and low porosity. The spacing between the pores increases when the porosity decreases. The lower the porosity, the lower are the chances for emulsion coalescence on the membrane surface. The SPG membrane body is mainly composed of Al_2O_3/SiO_2 , which provides extremely high mechanical strength that can withstand high pressure applications. The chemical resistance of the membrane also offers the opportunity to use it with a variety of solvents.

As shown in Figure 2.1, for our particular system, all the desired components, such as the polymer, organic dye, and NPs are suspended in a volatile organic solvent used as the dispersed phase. The emulsifier is dissolved in aqueous solution that serves as the continuous phase. The dispersed phase is forced through the pores while the continuous phase flows along the membrane surface. We used a hydrophilic membrane to generate O/W emulsions. In this case, the dispersed phase will not wet the membrane

which offers better control of the shapes and sizes of the droplets during their formation. Initially, the droplets are held at the pore by interfacial tension. The droplets grow at the pore outlets and tend to stay spherical in shape to reduce the surface tension. When the diameter of the droplets attached to the pore increase to a certain threshold value, the droplets detach from the membrane wall. While the droplets flow in the continuous phase, the volatile organic solvent (chloroform) slowly diffuses into water and eventually evaporate. Finally, the droplets solidify and all the components are encapsulated inside the polymer matrix. Since the solubility of organic solvent in water is very low, there is sufficient time for the emulsifiers to rearrange on the surface of the droplets to minimize the free energy thus maintaining surface smoothness of the droplets.

As shown in Figure 2.3, there are five forces exerted on the droplets: buoyance force F_B , interfacial tension forces F_γ , the driving pressure $F_{\Delta p}$, and the drag force F_D from the flowing continuous phase.^{57, 58} The drag force plays an important role in detaching the droplets from the membrane surface. When the velocity of the continuous phase increases, the shear stress near membrane wall increases. The droplet size decreases dramatically as the wall shear stress drops until the velocity of the continuous phase flow does not influence the size of the droplets. We generate our droplets within this high wall shear stress regime, in which case it is less likely for coalescence to occur.

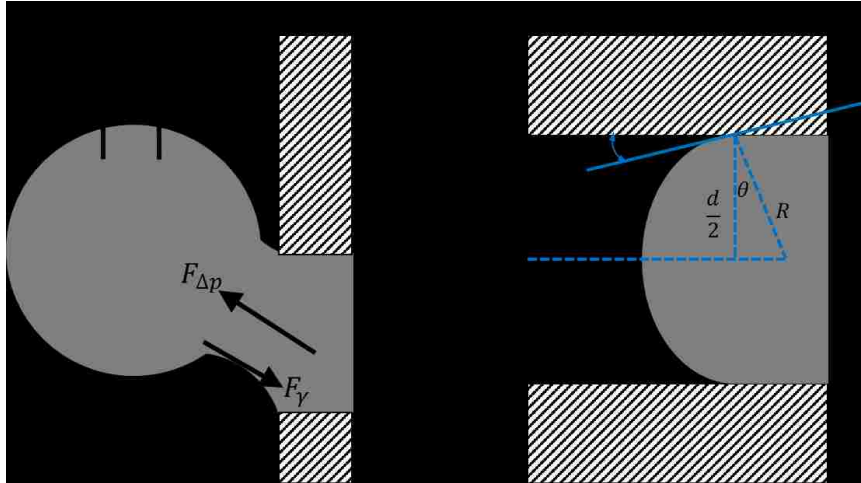


Figure 2.3 Dispersed phase is pressed through the membrane with applied pressure (right). After the droplet has formed on the pore outlet, there are five forces balanced on the droplet.

Emulsifiers are used to stabilize the droplets against coalescence and aggregation. We use SDS as the emulsifier. SDS is known to reduce the interfacial tension quickly between oil and water interface and has a relatively low dynamic interfacial tension. If the time of decreasing interfacial tension is shorter than the droplets formation time, then increasing transmembrane pressure effect on the droplet size.

The minimum transmembrane pressure that is required to generate the droplets is called the critical pressure and can be derived from the Young Laplace equation:

$$\Delta p = \frac{2\gamma}{R} \quad (2-1)$$

$$R = \frac{d}{2 \cos \theta} \quad (2-2)$$

$$p_c = \Delta p = \frac{4\gamma \cos \theta}{d} \quad (2-3)$$

where d is the diameter of the pore, γ is the interfacial tension, θ is the contact angle between the oil phase and the membrane surface and p_c is the critical pressure. The

transmembrane directly controls the flux of the oil phase through the pores. As shown in equation (2-3), larger pressure is required for membranes having smaller pore diameter.

We investigated the critical pressure required for different pore size membranes. As shown in Fig. 4A. The critical pressure decreases when the pore diameter increases as expected. However, the resulting curve does not obey the inverse relationship with respect to nominal diameter. One possible reason is that for some diameter pore membrane, there is a higher chance for coalescence to occur, which reduces the critical pressure. Varying the concentrations of polymer and NPs changes the interfacial tension which in turn leads to a change in the critical pressure. We found that the higher the NPs concentration, the higher pressure is required for generating droplets. On the other hand, the application of too high a pressure will produce an oil jet and resulting in uncontrollable large droplets (Figure 2.4). We chose to run our experiments at pressure close to the critical pressure to form emulsions, which make the emulsification time long (~1h). This slow process is beneficial because the time for absorbing emulsifiers on the droplets surface and decreasing interfacial tension will be much shorter than the droplets formation time.

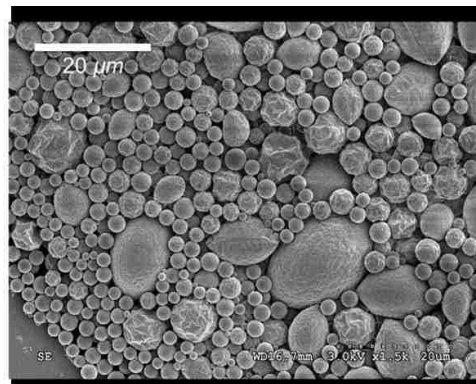
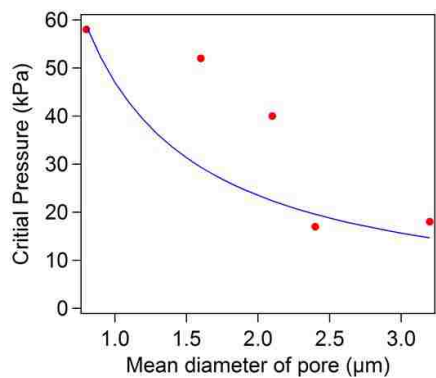


Figure 2.4 Critical pressure decreases with the increases of the mean diameter of the pore size (left). Large not non-spherical particle had been made with too high pressure applied to the system (right).

2.3.2 Tuning the size of the particles

The conditions we are using to generate emulsions give us two simple options to change the size of the polymer microspheres. We can vary the polymer concentration in the dispersed phase or change the pore size. Two different concentrations of the polymer using the same pore size membranes were synthesized (Figure 2.5). The mean diameter of the particles increases when the polymer concentration increases. The simple explanation is that when the concentration of the polymer increases, the amount of polymer per droplet increases, resulting in a bigger volume of the solid microparticle.

Mean particle diameter is also a function of the membrane pore size. We expect that the droplet size scales with the membrane pore, as well as the diameter of the solid microparticle. As shown in Figure 2.5, when the pore size decreases, the particles get smaller. We can easily control the particle size by changing the concentration of polymer and the pore size. Smaller polymer particles are better for single molecule binding (avoid multi-tethered attachment) but have lower magnetite content (give lower force).

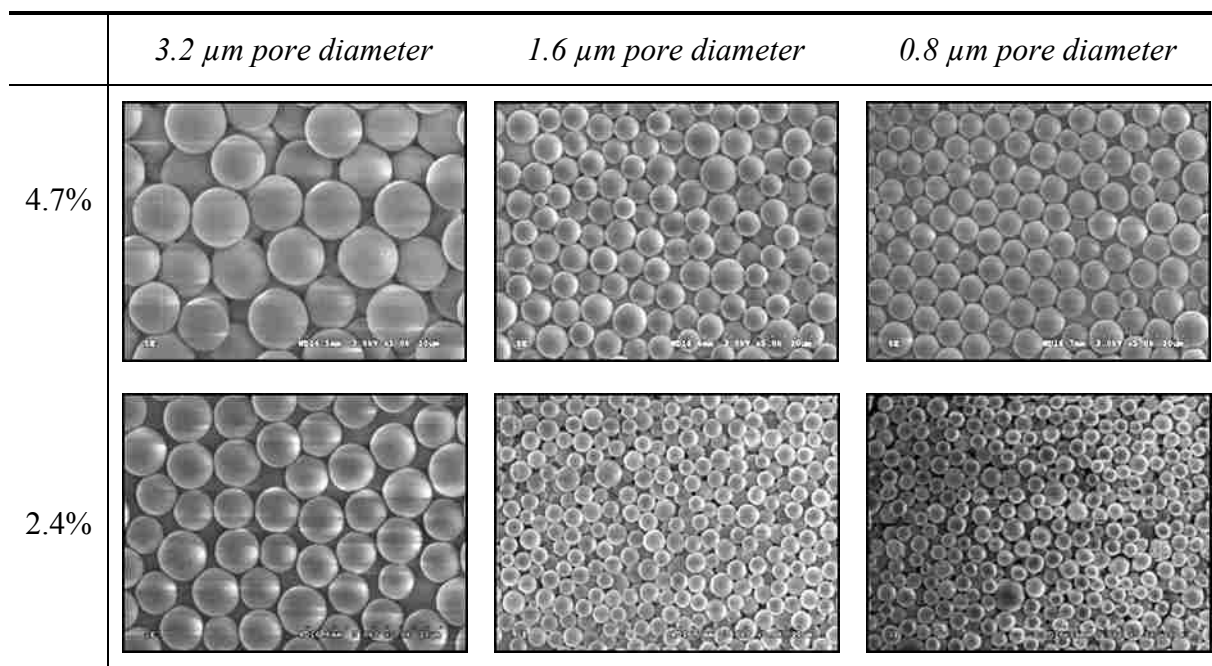


Figure 2.5 (A-C) Microspheres that were made with 4.7 % weight percent of polymer using different pore diameter membranes. (D, F) Microspheres that were made with 2.4 % weight percent of polymer using different pore diameter membranes. When pore diameter decreases, the size of the microsphere decreases. (A & D), (C & F) Microspheres that were made with same pore diameter but different weight percentage of polymer. Lower polymer concentration produces smaller sized particles. A typical size distribution of polymer microspheres with a Gaussian fit.

2.3.3 Surface smoothness

Figure 2.6B represents the cross-sectional view of the topography of the polymer particle taken along the red line in Figure 2.6A. We fabricated polymer microspheres with an extremely smooth surface (2 nm over 4 μm^2 area) that are suitable for single molecule binding.

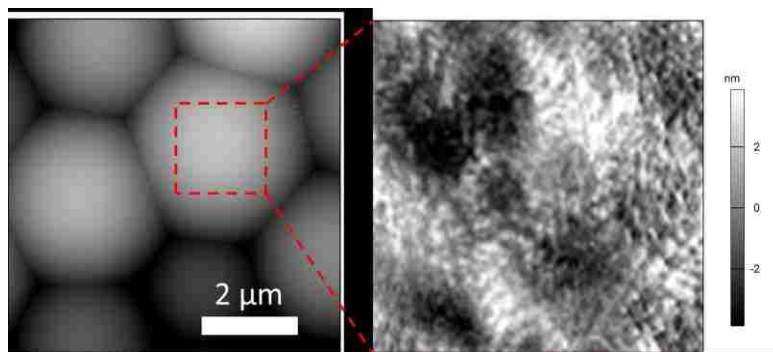


Figure 2.6 (A) Atomic force microscope image of assembled microspheres on the surface of glass slide. (B) A zoomed-in image of one of the microspheres. The curvature of the surface was subtracted from the image using a third order polynomial fit to show the roughness on the same scale as that of the surface.

2.3.4 Fluorescence

Figure 2.7A compiles fluorescent spectra of QDs we synthesized. The absorption wavelength blue-shifts after addition of shells on the CdSe. We chose to use the double shell QDs for encapsulation into the polymer microspheres due to their high quantum yield, desired wavelength, and photo-bleaching stability.

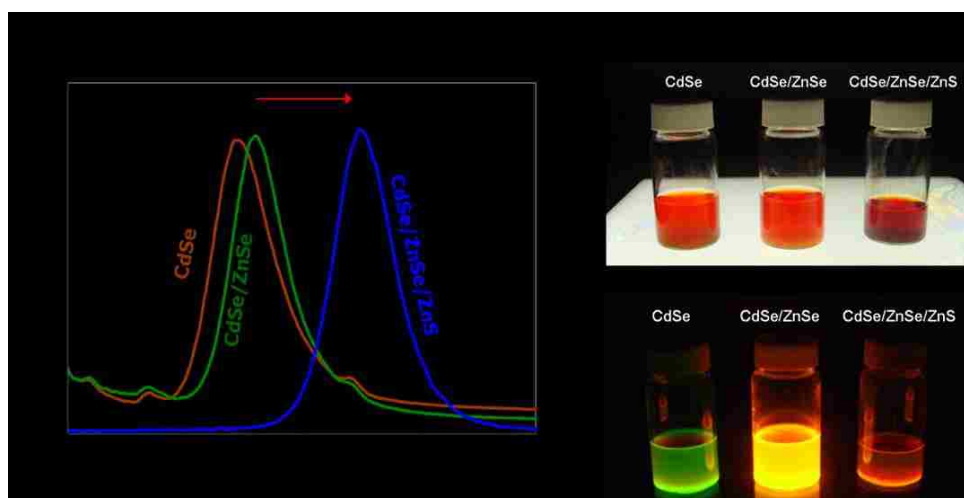


Figure 2.7 Fluorescence spectra of *CdSe*, *CdSe/ZnSe*, *CdSe/ZnSe/ZnS* QDs in toluene (left). Appearance of QD solutions under irradiation with (right top) visible or (right bottom) UV light (325 nm UV lamp) for *CdSe*, *CdSe/ZnSe*, *CdSe/ZnSe/ZnS* QDs.

We fabricated polymer microspheres that contained either QDs or organic dye as fluorescent component. By recording fluorescent images of the same polymer particle as a function of time, we were able to analyze the resistance to photo-bleaching of particles with different fluorophores. As we can see in Figure 2.8A, the integrated fluorescent intensity of the polymer particle with organic fluorophore inclusion decays exponentially under illumination (full power of light source) and the brightness drops nearly 50% after 400 seconds. The total intensity of the polymer particle containing QDs increases rapidly to the maximum value and then gradually decreases under illumination. The brightness decreases about 14% from the maximum value after 2000 seconds. Since the force probes need to be continuously observed with fluorescent microscopy in magnetic tweezers setup, the polymer particles with QD inclusion meet the requirement.

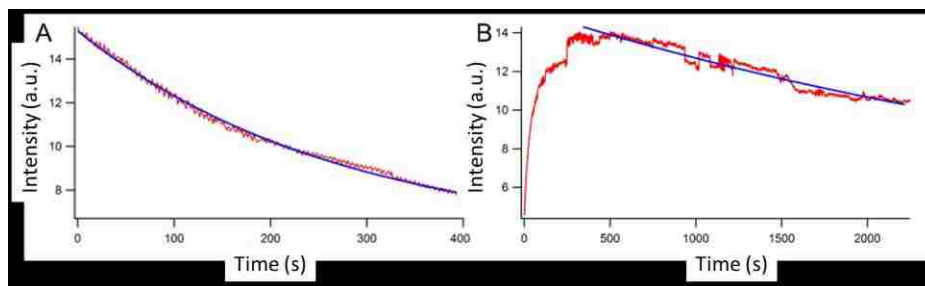


Figure 2.8 (A) The fluorescence intensity of the beads with organic dye inclusion exponentially decays over time (B) The fluorescent intensity of the beads with quantum dots inclusion drastically increases to the maximum value in a short period of time and follows an much slower exponential decay compared to organic dye.

2.3.5 Super-paramagnetic

Vibrating sample magnetometer (VSM) measurements showed that the probes were highly superparamagnetic — exhibiting no observable hysteresis (Figure 2.9).

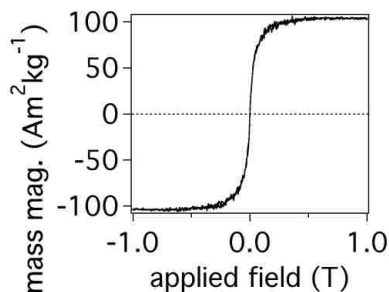


Figure 2.9 There is no observable hysteresis (a). Reconstructed relationship between force and applied field (b & c)

2.3.6 Surface charges and density of surface functional groups

We achieved efficient termination of the surfaces of these particles with carboxylic acid groups by having acrylic acid as a second component in the polymer matrix. For this purpose, we used poly(methyl methacrylate co-methacrylic acid) random copolymer (PMMA-MAA). The copolymer contained about 1 weight % of methacrylic acid, thus polar hydrophilic COOH groups are expected to occupy at least 1% or possibly more due to preferential segregation of MMA segments at the water-polymer interface of the surface sites in the course of formation of the polymer sphere in water. The surfaces of the beads were reactive towards further covalent modifications as was demonstrated by

linking an amino-functionalized dye molecule to these COOH-terminated beads (**Error! Reference source not found.**).

In order to quantitatively determine the density of surface functional groups, we compared the fluorescence intensity of the fluorophore attached to the bead surface to the fluorescence intensity of the fluorophores embedded in the polymer matrix at pre-defined concentration. As shown in **Error! Reference source not found.A**, typical fluorescent polymer particles show bulk fluorescence through the whole volume of the particle. No fluorophore containing polymer particles have only fluorescent dye molecule covalently bound on the surface through forming amide bond (**Error! Reference source not found.B**). Fluorescent microscopy image in **Error! Reference source not found.B** shows a halo-like pattern of particle carrying surface-bound TAMRA molecules.

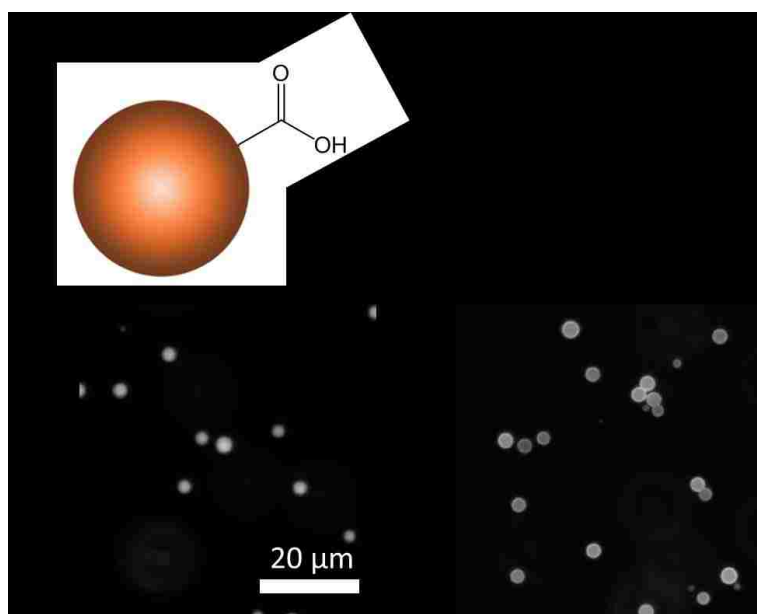


Figure 2.10 (A) A reaction scheme to demonstrate that surface functional groups for beads made from (PMMA-MAA) are available for covalent attachment. We used fluorescent dye bearing amino group (tetramethylrhodamine (TAMRA) 5- (and 6-) carboxamide cadaverine) to render nanospheres fluorescent after reaction coupling

surface carboxyl groups with amine groups of the dye molecules from aqueous solution. (B) Beads with bulk fluorescence. (C) No fluorophore containing particles reacted to the amino terminated dye molecule on the surface of the particles.

For particles that contain fluorophores on the surface, the relationship between fluorescence intensity I_{total}^S and particle radius R is:

$$I_{total}^S = I \cdot \frac{4\pi R^2}{a} \quad (2-4)$$

For particles that contain fluorophores in the polymer matrix, the intensity of the probe is:

$$I_{total}^V = I \cdot \frac{\frac{4}{3}\pi R^3}{V} \quad (2-5)$$

where I_{total}^S and I_{total}^V are the total intensity of one particle with fluorophore on the surface or distributed through volume, a is the surface area per fluorophore and V is the volume per fluorophore, and I is the intensity per fluorophore. Both total intensities of the particles are functions of the particle diameters (radius). We then plotted the total intensities for those two different types of microspheres versus their diameters. By fitting the two curves, we are able to determine the value of a . The relative loading of the dye and polymer is controlled in our experiments during the fabrication stage. Knowing the dye concentration in the polymer matrix, we calculated that $a = 750nm^2$. Thus the nearest neighbor distance between two carboxylic groups on the surface of the particle is 27 nm.

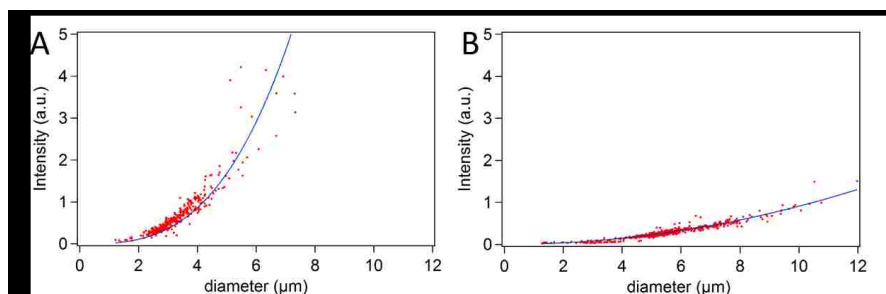


Figure 2.11 Total intensity as a function of particle diameter for both bulk fluorescent polymer particle (left) and surface fluorescent polymer particle (right).

Zeta potential measurements (Figure 2.12) also confirmed that carboxyl termination was present: PMMA-PAA beads gave values between -20 and -48 mV in the pH range from 3 to 11.5. A number of applications of these particles could be envisioned where the reactivity of the surface carboxyl groups is exploited. Since the proper surface chemistry in our methods are general by the choice of monomer, this surface modification and other organic functional groups (e.g. amine) can be readily introduced onto the surface of the nanospheres by the appropriate choice of co-polymers.

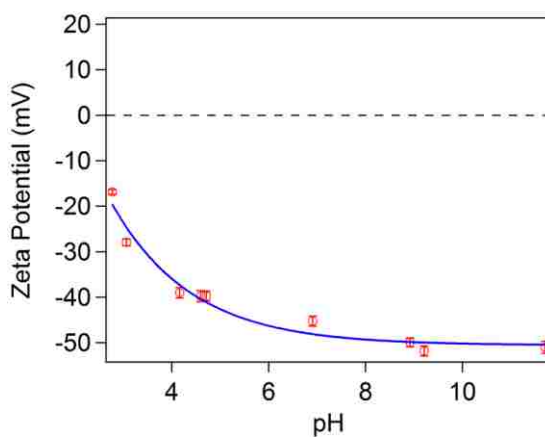


Figure 2.12 Zeta potential decreases as a function of increased pH value.

2.3.7 Changing the magnetite concentration

Since the force exerted on magnetic polymer particles depend on the concentration of magnetite. We investigate effects of having high magnetite content on the quality of the microspheres. We synthesized polymer particles using 3.2 μm pore size SPG membrane with magnetite up to 36% (by mass). We observed that when the magnetite concentration is higher than 20% (by mass), the particle surface becomes rough (Figure 2.13).

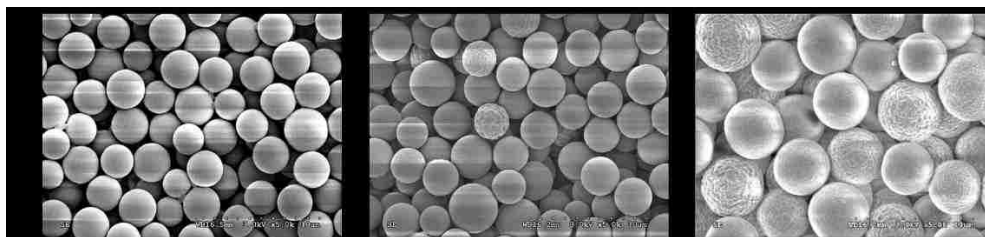


Figure 2.13 Microspheres with 20% (A), 26% (B) and 36% (C) weight percent of magnetite inclusion (A-C). The surface of the microspheres become rougher with the increase of the concentration of magnetite. Particle surfaces remain smooth when concentration of magnetite if not larger than 20%.

2.4 Conclusions

Inclusion of magnetic nanoparticles into polymer beads by a fast one step membrane emulsification method reported here is a very attractive route to superparamagnetic polymer particles. Manipulation of these objects can be performed in a non-contact manner with the application of a magnetic field. For ease of observation, these beads require stable fluorescent labeling that can be achieved by addition of semiconducting nanoparticle. The membrane emulsification method reported here uses a polymer solution rather than small molecule precursors more commonly used. Our

method is suitable to rapidly adjust the properties of these probes to fit the requirements of a particular application. We turned our attention to the synthesis of these composite nanospheres due to their potential application in force spectroscopy with magnetic tweezers. Further optimization of the micro-emulsion synthesis for these composite colloidal probes directly from polymer solutions and development of the procedures for their fractionation by size or magnetization should lead to high quality probes suitable for use in detection, tracking, and manipulation of single molecules.

Chapter 3 : Single-Molecule-Bead Assemblies for Parallel Single Molecule Force

Spectroscopy

*Part of the work described in this chapter has been published in M. J. Barrett, P. M. Oliver, P. Cheng, D. Cetin and D. Vezenov, High Density Single-Molecule-Bead Arrays for Parallel Single Molecule Force Spectroscopy, *Analytical Chemistry*, 2012, 84, 4907-4914.*

3.1 Introduction

In the push towards personalized medicine, affordable DNA sequencing is essential.^{2, 59} To reduce the total cost of genome sequencing, we have proposed a sequencing method that uses force spectroscopy to detect the conformational changes of DNA in the course of a stepwise ligation.²⁴ This approach to sequencing requires a controlled ligation of short DNA strands of known composition to the DNA strand in question followed by mechanical stretching of individual molecules to determine the success or failure of the ligation (as in sequencing by synthesis).³⁰ The detection step does not use expensive fluorescent labels and customized enzymes, thus, simplifying the process and ultimately lowering the cost.⁵⁹ One of the main challenges in building a sequencing platform based on direct manipulation of single DNA molecules as envisioned above is the fabrication of high-density arrays of DNA-force probe assemblies to ensure parallelism. The array is constructed by attaching the DNA strands with one end to the surface of a rigid support and, at the opposite termini, to the microscopic force probes (e.g. magnetic-fluorescent microspheres). A force field (either magnetic or dielectrophoretic) can then be applied to pull on the probe and generate force versus extension curves for multiple DNA molecules in parallel.⁶⁰ Wide field microscopy enables simultaneous observation of multiple force

probes. The observation of the stretching behavior on such a large sampling scale can give insight into sequence effects in DNA elasticity and thermodynamics, polyelectrolyte stretching behavior, as well as DNA-protein interactions⁶¹.

To create such a highly parallel, high throughput force spectroscopy method, our design must include an array of probes that can withstand the shear force of multiple exchanges of reagent solutions.⁶² The conjugation procedure should be carefully chosen in order to avoid the problem of multiply tethered force probes (magnetic microspheres, see Figure 3.1). On the other hand, a very low density of DNA-beads assemblies will also reduce the information yield of the substrate. For bioanalysis based on single-molecule techniques, the regime of appropriate molecular spacing ranges from just above the diffraction limit of resolution in light microscopy (~300-400 nm) to the micron scale. Finally, the number of the beads that bound to the surface of the substrate non-specifically need to be minimized.

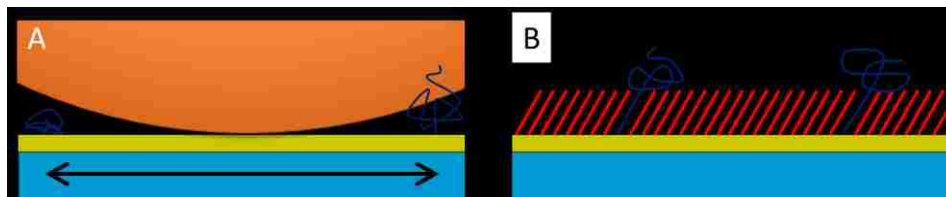


Figure 3.1 Schematic of minimum spacing of DNA molecules allowable using magnetic tweezers. a) A probe with a diameter of 1 μm and a DNA molecule with a radius of gyration of 11 nm (200-mer ssDNA) would require a intermolecular spacing of approximately 400 nm or greater to ensure only one DNA is attached to the probe. b) Intermolecular spacing can be achieved by competitively binding the DNA with a blocking molecule.

Biological complexes are frequently used for immobilization of a target molecule for molecular force spectroscopy. Most experimental work in single-molecule force spectroscopy relies on biotin-avidin binding^{63, 64} as a form of immobilization at one end of the DNA or protein molecule. Such non-covalent bonds tend to be unstable with their life-times shortened significantly if the bond is loaded. For this reason, covalent chemistry should be the preferred method for immobilizing DNA molecules on a substrate for biosensing technologies when multiple cycles of reaction-wash-detection steps are carried out. This chapter describes the tuning of the surface chemistry and reaction conditions for bead attachment to fabricate a high efficiency, high density single-molecule-bead array suitable for use in experiments on single-molecule manipulation with tethered beads.

3.2 Approach

In developing procedures to create a surface with properties suitable for magnetic tweezers, one must (i) control the surface density of DNA oligomers, (ii) enable robust attachment of oligos to both the surface of the solid support and the force probe (i.e. microscopic bead); and (iii) ensure that bead attachment occurs only via a terminal group of the DNA, whereas the surrounding area resists non-specific adhesion of the bead. To implement these features, we have developed a series of chemical modifications to the probe, DNA, and substrate (Figure 3.2). We developed DNA library preparation procedure that results in orthogonal binding chemistry at 3' and 5' ends of the ssDNA, for example, via end-modification with thiol and amino groups. We then used gold-thiol chemistry for attachment of the DNA to the surface of the solid support, while carboxyl-

functionalized probes were attached to the amine groups of the opposite end of ssDNA molecules. To control the spacing between the DNA molecules and to reduce non-specific adhesion of the force probes, we optimized conditions of competitive binding of the thiol-terminated DNA and an inert thiol, forming a blocking layer. To ensure that only one molecule is interrogated by a single force probe, the surface density of the target molecules should have nearest neighbor distances similar to the force probe diameters (1-3 μm). The spacing can be controlled in a rational manner by adjusting the relative amount of the DNA and spacer thiol in solution.

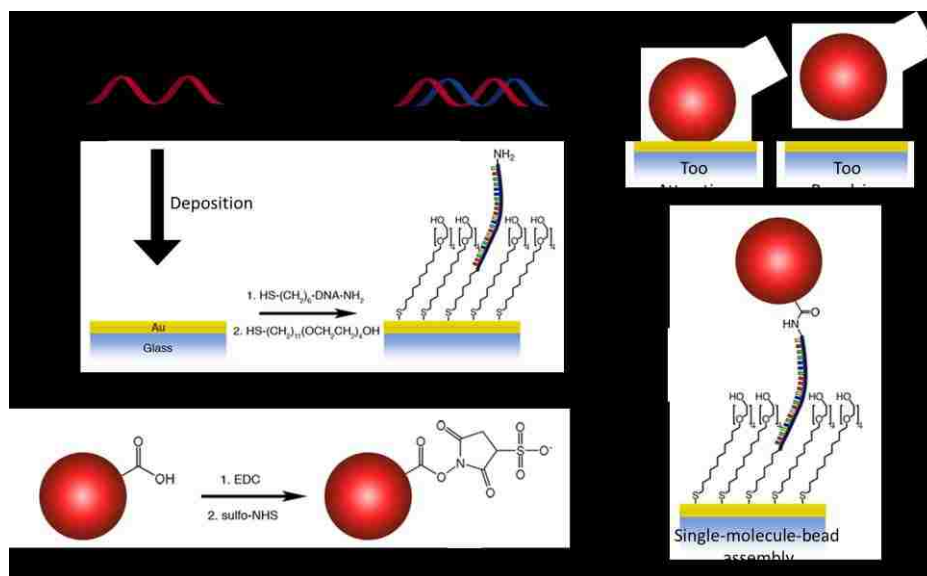


Figure 3.2 Chemistry of attachment of a force probe to DNA oligomers anchored at a solid surface. A double stranded DNA (a) is end-modified, denatured, and combined with a thiol blocking molecule for reaction with a gold coated substrate (b). A carboxyl terminated probe is then activated and allowed to come in contact with the probe (c). When in the vicinity of the DNA molecules one of three outcomes may occur (shaded area): (i) the probe and surface will be too attractive and the probe sticks to the substrate, (ii) the probe and surface will be too repulsive and the probe is unable to bind, or (iii) the probe will come close enough to the DNA and covalently link, while not adhering to the surface.

3.2.1 Control of DNA surface density via competitive binding

We have determined that it is best to use a competitive binding process (where the DNA and MutEG are reacted at the same time) to control the DNA density on the surface. To attach the DNA oligomers as well as add an organic blocking layer, we have chosen to use self-assembled monolayers (SAMs) of thiols on gold due to easy, reproducible chemistry and flexibility in the choice of the ω -functional group. Thiolated DNA on gold is a well-established system for achieving covalent DNA-surface binding via self-assembled monolayers similar to those formed by alkanethiols⁶⁵, however, information on the spatial distribution of the surface bound DNA in such films is lacking. Controlling inter-molecular spacing with DNA brushes,^{65, 66} Tarlov, et. al. showed average nearest neighbor distances of 1 – 4 nm, too dense for analysis by single-molecule techniques. Electrochemical desorption can attenuate the high density of DNA on a gold-coated substrate, however, a nearly complete monolayer of DNA is first formed during these experiments and detection of single-molecules has not been reported to our knowledge.^{67, 68} Furthermore, while the detection of single-molecule fluorescence is the most direct way to derive molecular density on the surface, the metal film will quench the fluorescence from the labeled DNA, making it challenging to observe the distribution of the single DNA molecules on a gold-coated substrate.^{69, 70} Instead, the methods most commonly used for obtaining the binding density of DNA on a gold surface include

radiolabeling, nanoparticle labeling, UV-vis spectroscopy, x-ray photoelectron spectroscopy (XPS), and electrochemical methods. Of these methods, only nanoparticle labeling can yield information about the spatial distribution of the molecules. The density of DNA in a mixed alkanethiol-DNA layer on gold has been measured by counting gold-nanoparticle labels in the AFM images, but the concentration ranges probed resulted in hundreds of molecules per square micron (~ 10 nm spacing).⁷¹

In this chapter, we report on the fabrication of a DNA array with controlled spacing in the range of 100-1000 nm for use with single-molecule force spectroscopy or single-molecule fluorescence experiments. We describe the use of single molecule fluorescence to measure the real-space distribution of dye-labeled and thiolated DNA covalently bound to a transparent gold-coated glass substrate. We visualized the distribution of immobilized DNA by using a small-molecule thiol to lift the fluorophore from the metal surface in the course backfilling gold sites remaining after reaction with the DNA. The spatial distribution was then confirmed with AFM and SEM characterizations. We demonstrated that mixed alkanethiol and thiolated DNA self-assembled monolayers on the thin gold substrates can be used to control the density of immobilized DNA.

3.2.2 Tuning the reaction conditions to attach single bead to single molecule

To gain insight into the behavior of the forces between a surface and a probe, we used extended DLVO theory⁷²⁻⁷⁴ to model how various parameters in our system affect the magnitude and character of respective interactions. This theory states that the total

force acting upon the system is the sum to the electrostatic (F_{el}), steric (F_{st}), and van der Waals (F_{vdW}) forces,

$$F_{total} = F_{el} + F_{st} + F_{vdW} \quad (3-1)$$

The total force is now easily broken down into the three components that can all be independently manipulated. In practice, one can adjust system variables (e.g. solution or surface composition) to obtain the desired force-distance profile (Figure 3.3).

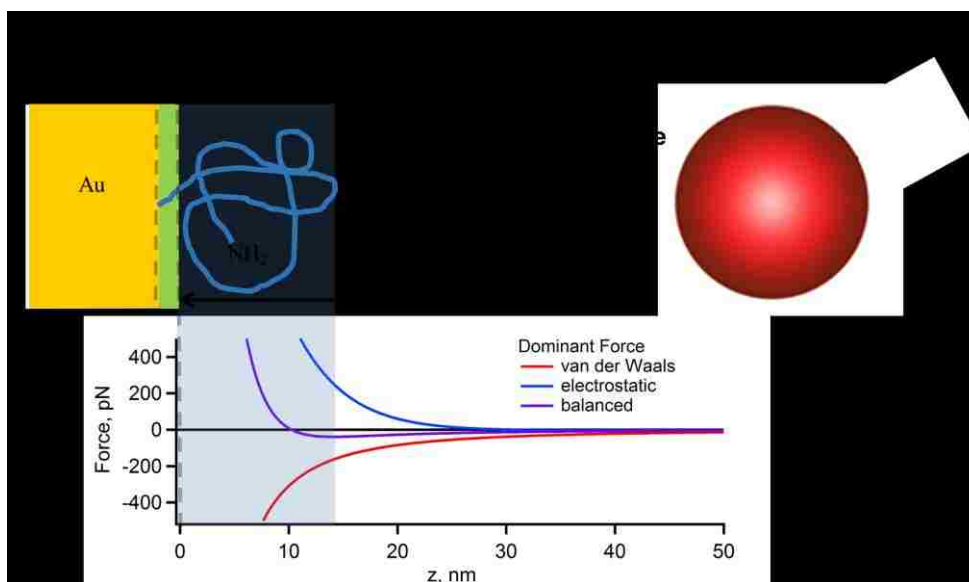


Figure 3.3 Representation of a force profile for a probe (microsphere) approaching a surface. To bind to the DNA molecule, the probe must interact with the amine terminal group by passing into the area represented by the blue-gray shaded box. If the probe comes in contact with the surface, it will most likely adhere strongly, so it must not pass completely through the region indicated by a shaded box. The graph shows three representative force-distance profiles as the probe approaches the surface. The repulsive electrostatic force can be too strong and prevent the probe from approaching the target molecule. Conversely, the van der Waals attractive forces can be too strong and cause the probe to stick irreversibly to the surface. If the forces become balanced, the probe will be attracted to the point where it may bind to the DNA, but is repelled at a very close proximity to the surface.

By comparing the electrostatic, van der Waals, and steric forces we can begin to build a force-distance profile and qualitatively determine the effects of changing the parameters governing the probe surface interactions. The forces can be written as

$$F_{el} = \frac{2\pi\epsilon_0\epsilon_r\kappa R}{1-\exp(-2\kappa z)} (2\Psi_p\Psi_s \exp(-\kappa z) + (\Psi_p^2 + \Psi_s^2)\exp(-2\kappa z)) \quad (3-2)$$

$$F_{vdW} = \frac{-H_{opm}R}{6z^2} + \frac{-H_{spm}R}{6(z+t)^2} \quad (3-3)$$

$$F_{st} = 72\pi R\Gamma k_B T \exp\left(-\frac{z}{R_g}\right) \quad (3-4)$$

We define all the parameters involved as follows: the separation between the probe and substrate (z), probe radius (R), the surface potential of both the substrate and the probe (Ψ_s and Ψ_p), and the inverse Debye length of the medium (κ), ϵ_0 is the permittivity of free space and ϵ_r is the relative permittivity of the medium, H_{opm} is the Hamaker constant between the organic blocking layer and the probe across water, H_{spm} is the Hamaker constant between the probe and the gold metal substrate across the blocking layer and water, Γ is the grafting density of the polymer chains protruding from the surface, and R_g is the radius of gyration of the polymer.

This set of equations makes it clear that all three types of forces have identical dependence on R , thus differences in the probe size we will only be manifested as a change in the magnitude of the forces acting on the probe and not the character of the force-distance profile. Therefore, small probes will be easier to remove from the surface and less likely to adhere permanently. On the other hand, the magnetic force acting on a super-paramagnetic particle scales as R^3 , thus resulting in a substantial loss in magnitude

of the pulling force for small R , making a reduction of the radius of the particles impractical.

In our modeling we are able to ignore the effects of gravity, since the force of gravity of polymer probes of this size is under 1 pN, which is well below the magnitude of the electrostatic and van der Waals forces.

In our system, the thickness of the blocking layer, the Debye length (by way of the solution ionic strength), the probe and substrate potentials, and the Hamaker constants can be targeted to change the system properties the easiest. The theoretical responses of tuning these parameters can be seen in Figure 4. Each of the systems is relatively easy to tune. The ionic strength can be changed by altering the concentration of sodium chloride, the blocking layer thickness is tuned by changing the number of carbons in the chain of the thiol blocking moiety, the surface potential are a function of the pH or the nature of the surface functional groups, and the Hamaker constants depend on the materials used. Of the four properties, the Hamaker constant is the most difficult to change since significant alterations in its value would require drastic changes in the substrate and/or probe, thus requiring a different scheme for surface chemistry.

Using this model, we can predict the trends that will emerge by varying experimental parameters for the system (Figure 3.4). The repulsive electrostatic forces acting on the probe will grow with the increase in the surface charge (e.g. the zeta potential), while the attractive van der Waals forces will remain constant. Therefore, the probe can be detached from the surface using weaker pulling forces (Figure 3.4a). In addition, the increased potential pushes the stable position of the probe (zero force) further away from

the surface. Of all the system parameters at our disposal, the tuning of the ionic strength is by far the most dramatic. With a low ionic strength, the probes are unable to approach the surface, whereas a high ionic strength will completely screen the electrostatic forces giving the system minimum repulsion (Figure 3.4b). If we alter the substrate component of the Hamaker constant, we can decrease or increase the depth of the attractive well without changing the distance of the force minimum (maximum adhesive force) from the surface (Figure 3.4c). The blocking layer thickness has a similar effect, however, the task of tuning the layer thickness is much easier than changing the substrate material (Figure 3.4d).

The theoretical force-distance profiles indicate that in order to bind a microscopic force probe to the ssDNA strand with $R_g=12$ nm (200 base long) the ionic strength must be greater than 10 mM to allow the probe to approach the surface. The remaining parameters control mainly the magnitude of the force minimum (maximum adhesive force). Since our magnetic tweezers setup is capable of applying forces of up to 20-40 pN, it is important that the maximum adhesion force is below that value under most experimental conditions. Convenient surface chemistry dictated our choice of gold as a substrate for magnetic tweezers and effectively fixed the value of the Hamaker constant. Therefore, we must use a system with a thick blocking layer as well as a mid-range surface potential (~ -40 mV) to allow the probe to approach the DNA without adhering to the surface. Using this theoretical description, we systematically tested multiple conditions to determine a range of the above parameters where the specific binding of the probes is optimal, thus creating a general scheme for our magnetic tweezers platform.

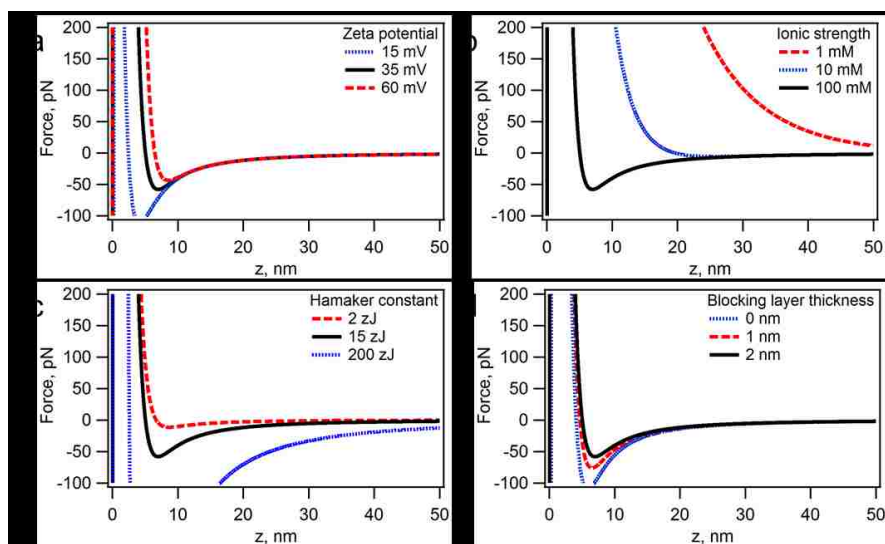


Figure 3.4 The effects of tuning the parameters of the system based on DLVO interactions between a polymer bead (4.5 μm diameter) and an organic layer (thiol monolayer) on gold in water. The zero distance is set at the organic layer/water interface. The black curves in each graph represent a standard set of conditions, where ionic strength = 100 mM, zeta potential = 35 mV, blocking layer thickness = 2 nm, the blocking layer-water-probe Hamaker constant = 2 zJ, and the substrate-water-probe Hamaker constant of 15 zJ. The effects of zeta potential (a), ionic strength (b), substrate-water-probe Hamaker constant (c), and the blocking layer thickness (d) were evaluated.

3.3 Methods

3.3.1 Materials

A 40 mm diameter glass coverslip (No. 1.5) was coated with a thin layer of gold using e-beam evaporation (4.0 nm Ti and 11.0 nm Au, Eddy Co. SYS-24, SC-20-Digital System Controller). After e-beam evaporation, substrates were constantly kept under vacuum and rinsed with ethanol (spectrophotometric grade, 90% ethyl alcohol, 10% isopropyl alcohol, EMD Millipore) and dried with nitrogen immediately before use. (11-mercaptoundecyl)tetra(ethylene glycol) (MutEG) and 6-mercaptohexanoic acid (MHA)

were purchased from Sigma Aldrich with 95% purity and were used as is (kept at -20°C). We purchased a short ssDNA oligo labeled with carboxytetramethylrhodamine (TAMRA) at the 3'-end and a protected thiol at the 5'-end (39-mer – 5'-HOCH₂CH₂S-S-(CH₂)₆-TTT TTT TTT TTT TTT TCA TCG CAC ATC GTA GCA CAA GAC-TAMRA-3') from Integrated DNA Technologies (Coralville, IA). A non-fluorescent thiol-modified 80-mer ssDNA oligo (5'-HOCH₂CH₂S-S-(CH₂)₆-(TATT)₂₀-3') was acquired from the same supplier. A 100 μM stock solution of DNA was made in autoclaved Millipore DI-H₂O. Before each experiment, an aliquot of the labeled DNA was diluted by a factor of 5 with a solution of 5 mM TCEP (tris(2-carboxyethyl)phosphine) in 6x SSC buffer (pH 7.4) and left standing for 30 minutes to reduce the disulfide. All subsequent dilutions were by a factor of ten or more in 10 mM phosphate buffer with 1 M NaCl at pH 7.4. Solutions of MutEG and MHA were diluted from a 1 mM stock solution in 10 mM phosphate buffer with 1 M NaCl at pH 7.4. Magnetic beads were synthesized using the method described in chapter 2.

3.3.2 *Au NPs synthesis and labeling with a primer*

5 mg of chloroauric acid was dissolved in 50 mL of DI-H₂O in a flask. 20 mg of sodium citrate was dissolved in 2 mL of DI-H₂O to make stock solutions. The flask was placed on a hot plate/stirrer. While stirring the solution with a magnetic stirrer, the solution in the flask was heated to boiling. The size of the Au NPs depends on the molar ratio of two reactants. For our purposes, we added 0.7 mL sodium citrate stock solutions to the flask to make ~30 nm NPs. After the color of the solution appeared red (about 10 min), the flask was removed immediately from the hot plate and the size of the NPs was

checked using UV-Vis spectrometer. The concentration of the Au NPs was derived from drying the solution of known volume and measuring the dried mass. 200 μL of AuNP solution was added to 7.22 μL of 100 μM DNA oligo thiolated-primer (in disulfide form). After letting the solution sit for \sim 16 hours at RT, the solution was centrifuged at 15,000 rpm in a 1.5 mL centrifuge tube for 30 min and then the supernatant was removed. The NPs were resuspended in 150 μL 0.1 M NaCl PBS buffer (pH 7.4, 137 mM NaCl, 2.7 mM KCl, 0.02% NaN_3 PBS buffer) and incubated for 40 hours. The NPs were washed three times by centrifuging and resuspending in the same buffer.

3.3.3 Samples for 39-mer DNA attachment via competitive binding

Eight 10 μL solutions were prepared with different ratios of 39-mer 5'-HS-DNA-TAMRA-3' to blocking thiol. All solutions, except one (control), contained 0.5 μM of DNA. The MutEG or MHA concentrations varied from zero to 1 mM. The solutions were pipetted at nearly the same time (as separate drops) onto a single transparent gold-coated glass substrate for 2 hours, then rinsed thoroughly with DI- H_2O , incubated in 1 mM MutEG or MHA for 1 hour (in 1M NaCl PBS), again rinsed with DI- H_2O , and dried with nitrogen. Fluorescence images of the TAMRA-labeled oligo were taken under TRITC illumination conditions (at least 5 images were taken for each spotted concentration up to 200:1).

3.3.4 Samples for 142-mer DNA attachment and further hybridization

Eight 10 μL solutions were prepared with different ratios of 142-mer 5'-HS-DNA-TAMRA-3' to blocking thiol. All solutions, except one (control), contained 0.5 μM of

DNA. The MutEG or MHA concentrations varied from zero to 1 mM. The solutions were pipetted at nearly the same time (as separate drops) onto a single transparent gold-coated glass substrate for 2 hours, then rinsed thoroughly with DI-H₂O, incubated in 1 mM MutEG or MHA for 1 hour (in 1M NaCl PBS), again rinsed with DI-H₂O, and dried with nitrogen. Either 1 μ M of primer labeled Au NPs or TAMRA-primer in 1X PBS buffer were pipetted on the eight spots, and incubated for 1 hour. SEM (Hitachi High Technologies America, Inc.) images, fluorescence images and AFM images (MFP-3D-BIO Asylum Research) were then taken.

3.3.5 Probe binding assays

The probe binding assays were performed in samples comprising a 4 mm thick polydimethylsiloxane (Sylgard 184 Silicone Elastomer kit) mask with 4 mm diameter wells on top of a gold substrate. In each well, 20 μ L of the desired thiol blocking molecule solution was added and allowed to react for 2 h to ensure a complete coverage of the SAM. Upon completion of the reaction, the well was rinsed twice with the solvent that the thiol was dissolved in and then twice in the final buffer solution meant to be studied. During the preparation of the substrate, the probes were prepared for the assay. 20 μ L of a 2 mg/mL (~2.5 million probes/mL) stock solution in 1% SDS were added to a microcentrifuge tube and washed in deionized water three times. The probes were then dried and reconstituted with 500 μ L of buffer being studied. Once reconstituted, the buffer was removed from the well and replaced with the solution of probes. The probes were allowed to settle for 15 min and a fluorescent image of TAMRA labeled probes was taken at 100 \times total magnification using a filter set designed for the TRITC chromophore.

A permanent magnet was placed on top of the wells, producing an approximate force of 200 pN to detach the probes from the surface, and a fluorescent image was taken after five minutes. On these images, the population of probes was sufficiently low that the probes could be individually counted using the particle analysis package in Igor Pro.

3.3.6 Analysis of fluorescence images

All image processing was performed using custom-written code in Igor 6.2 (Wavemetrics, Lake Oswega, OR). To calculate the total integrated intensity, the images were first cropped to approximately 400×400 pixels (89×89 μm). The integrated intensity of the cropped image was divided by the total area of the image to account for the differences in the areas of cropped images when calculating DNA coverage. The total intensity was calculated by averaging the image intensities within each region and subtracting the average intensity of the background (from images of a region with no DNA taken under identical conditions). For further analysis, the background was subtracted from the images by manually selecting regions of each image that contained no fluorophores and fitting them to a second-order 2D-polynomial. After subtracting the background, the images were filtered. We found, through trial and error, that Gaussian filtering (three passes, square matrix of 3×3), sharpening (3×3), and Gaussian filtering again provided the best contrast for our images. To identify locations of individual fluorophores or their clusters (deformed as “spots”) these were subjected to point filtering (3x3 matrix, 8x center – outer) thresholding at a value empirically determined to be adequate for the entire image set (see Figure 3.5). The algorithm selected spots at least two pixels in size and not excessively asymmetric in their shape (with aspect ratio < 2,

i.e. its (x, y) boundary fulfilled $\frac{1}{2} < (x_{\max}-x_{\min})/(y_{\max}-y_{\min}) < 2$). The number of spots was recorded for each image, along with the intensity of every individual spot. The spot intensities were obtained by integrating the signal within the spot boundary defined by the image thresholding. Histograms of the spot intensities, normalized to a probability distribution, were compiled for each sample or region suitable to analysis.

It was often difficult to distinguish between adjacent fluorescent spots using the thresholding algorithm when the surface was highly populated. Therefore, the number of spots was not a reliable metric for determining the surface coverage past a certain critical surface coverage. We determined that anything below a nearest neighbor distance of approximately 0.5-1 μm cannot be analyzed with the spot-finder algorithm. For these reasons, we do not plot the number of spots beyond approximately 400 per field of view, since for sample exceeding this spot density, a significant fraction of spots would be undercounted.

3.4 Results and discussion

3.4.1 Competitive binding of 39-mer ssDNA with MutEG

In order to tune the surface density of our 39-mer fluorescently-labeled DNA, we incubated our substrates in a solution which contained the blocking thiol along with the labeled oligo. The MutEG competes with DNA for open gold binding sites, effectively reducing the area available for DNA binding. When increasing the relative concentration of MutEG to DNA, we see a decrease in binding density—confirmed by fluorescence, SEM and AFM measurements.

3.4.2 Fluorescence measurements

Chemical attachment of the fluorescently labeled DNA to gold without any MutEG results in samples that do not show any fluorescence above the background level under our illumination/detection conditions (Figure 3.5, left). The flat gold substrate, in close proximity of the fluorophore (< 2 nm according to ellipsometry data on thickness of the DNA layer), is expected to act as a highly efficient quencher of TAMRA fluorescence. This quenching of fluorescence is the reason that, in most cases, characterization of these DNA-on-Au systems has been carried out using non-optical methods, such as XPS, ellipsometry, electrochemistry, radiolabeling, etc. Due to the potential for quenching, and to reduce the amount of nonspecifically-bound DNA, we always passivated the substrates with a blocking thiol for 1 hour after addition of the DNA solution. After exposure to the MutEG solution, the physisorbed regions of the DNA were displaced from the gold surface due to formation of the self-assembled monolayer of the small-molecule thiol. As a result, the fluorophores at the 3' termini of the DNA molecules (immobilized via their 5' ends) were lifted from the metal surface, resulting in a noticeable fluorescence for samples of all compositions. The quenching of fluorescently-labeled DNA has been reported previously in literature and can be used as an analytical tool for studying the effects of temperature and ionic strength on DNA, or for detection of hybridization of the label-free complementary DNA.

Figure 3.5 shows representative fluorescence images at several solution ratios of MutEG to DNA. The most apparent feature of these images is the aggregation of fluorescent material in nucleating sites at the lower MutEG to DNA ratios. As the MutEG

concentration increases, the overall intensity, peak intensity, peak size, and peak number all decrease. After finding the peak locations by thresholding, we captured the peak intensities of several images for each ratio of the two thiols. We generate a series of histograms of those fluorescent images. The histograms show a clear reduction in multiple-fluorophore (high intensity) peaks as the MutEG concentration is increased. We attribute this reduction in high intensity peaks to lower surface-DNA aggregation, probably as a result of a higher potential for interaction between DNA and MutEG. It is possible that the MutEG is passivating the surface, which reduces the van der Waals interaction between the gold and DNA and prevents intimate contact between multiple bases and Au surface, thus moving the mechanism of reaction towards the slower rate path and much smaller rate constant. Castner, et. al. have shown that MutEG backfilling effectively reduces the interaction between ssDNA and the gold, allowing for improved orientation of the DNA on the substrate. Since the DNA is forced to spend more time looking for an open site on the surface, the electrostatic repulsion between adjacent DNA molecules probably becomes more important; hence, the DNA molecules tend to adsorb in a more highly spaced manner.

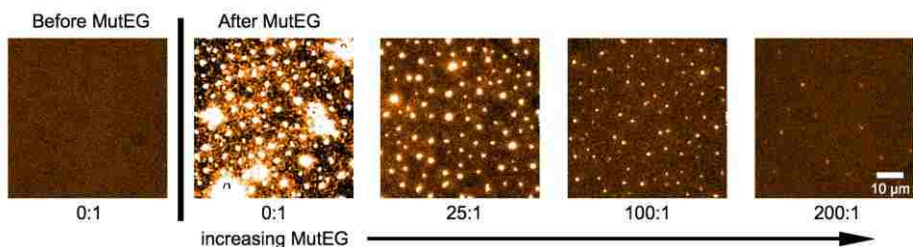


Figure 3.5 Microscope images of fluorescent TAMRA-labeled DNA competitively adsorbed with MutEG on an optically-transparent gold substrate followed by passivation by MutEG. Ratios indicate the relative concentration of MutEG to DNA for each image. In the pure DNA sample (0:1), essentially no fluorescent signal is seen before addition of

MutEG. A reduction of overall fluorescence signal, a decrease in the size of the peaks, and a decrease in the number of peaks are observed as the MutEG concentration is increased. Images were flattened by fitting the background areas to a 2-D second-order polynomial and subtracting the result from the whole image.

Aggregation of fluorescently-labeled and thiolated DNA (30-mer) on a gold surface has been reported by Bizzotto, et. al., but their images show a more heterogeneous distribution of fluorescence intensity and are not consistent with the long-range uniformity seen in our images. These differences are likely due to different types of Au substrates employed. Bizzotto, et. al. studied DNA SAM formation using 1-2.5 mm gold beads, which may be a rougher surface compared to e-beam evaporated polycrystalline gold on a glass substrate (we measured an RMS roughness of < 0.8 nm over a $1 \mu\text{m} \times 1 \mu\text{m}$ area using AFM, with no large islands visible). Their work did, however, reveal that double-stranded DNA has a lower propensity for non-specific adsorption than single-stranded DNA.

3.4.3 Surface MutEG/DNA ratio as a function of solution ratio

Since we are going to stretch around 142-mer long ssDNA in magnetic tweezers, we repeated competitive binding experiments using 142-mer ssDNA and then conducted SEM, fluorescent microscopy and AFM measurements. Figure 3.6 shows typical SEM images of different solution ratios of MutEG to DNA with Au-primer hybridized on the end of 142-mer ssDNA. This result confirms the observation from fluorescent images that when the MutEG concentration in solution increases, the density of the DNA on the surface decreases.



Figure 3.6 Scanning Electron Microscopy (SEM) images of competitive adsorption of MutEG and DNA. The relative MutEG and DNA concentrations are 10 (a), 200 (b) and 2000 (c) respectively. The scale bar is 1 μm .

The SEM measurements were compiled in terms of the surface MutEG to DNA mole fraction versus solution MutEG to DNA mole fraction, as shown in Figure 3.7. The results from Fig. 7 indicate a clear saturation of DNA coverage at low MutEG to DNA ratios. The saturation is not surprising, considering that MutEG is expected to form a closely-packed monolayer with a 0.214 nm^2 average parking area, while the 142-mer ssDNA will have a parking greater than $\sim 9\text{-}10 \text{ nm}^2$ (depending on deposition conditions) based off of our XPS measurements of neat DNA on gold. This greater than fifty-fold difference in parking area means that MutEG is expected to have little effect on spacing out DNA below a certain threshold, $N_{MutEG}^{soln.}/N_{DNA}^{soln.} \approx 20$.

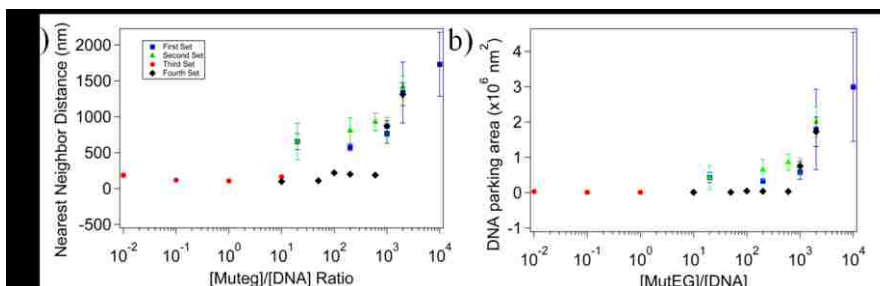


Figure 3.7 Experiment of competitive adsorption of MutEG and DNA. Competitive kinetics of both mechanism 1 (black-line) and mechanism 2 (red-line) are shown. (a) Plot of DNA parking area versus relative MutEG and DNA concentration. (b) Log plot of nearest neighbor distance versus relative MutEG and DNA concentration.

The slope of the line (fitted to points above $N_{MutEG}^{soln.}/N_{DNA}^{soln.} = 20$) is 234 ± 104 and should be equal to the ratio of the rate constants of MutEG with DNA.

$$N_{MutEG}^{surf.}/N_{DNA}^{surf.} = \frac{k_{MutEG}}{k_{DNA}} \cdot N_{MutEG}^{soln.}/N_{DNA}^{soln.} \quad (3-5)$$

Fluorescent and AFM images confirm SEM results. Figure 3.8 shows spatial distribution of single 142 bases long ssDNA molecules on gold coated glass substrates after immobilization under conditions of competitive binding.

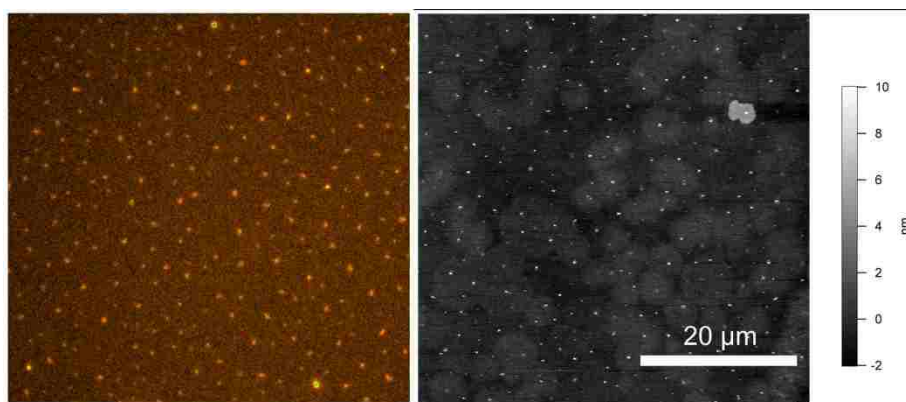


Figure 3.8 Distribution of the single ssDNA oligomers(142 bases) immobilized on Au surfaces is visualized using fluorescent (A) and tapping mode AFM (B) imaging after hybridization with a Cy5-labeled primer (21 bases, complementary to the end opposite to immobilization site). The density of ssDNA is comparable in both images.

3.4.4 Probe binding assay

To verify the predictions of the theory and to obtain a complete quantitative description of the binding of the probes to the surface, we used wide-area multi-probe binding assays. We conducted these experiments under various conditions (altering ionic strength, pH, and blocking layer thickness). The wide-area binding assays consist of two

steps. First, the probes settle by gravity on the surface and an image of their spatial distribution and population is recorded. A magnet is then applied and a second image is taken to determine the fraction of probes remaining on the surface after application of force. To illustrate the probe binding assay, we present in Figure 3.9 images of probes bound to a substrate both before and after a magnet is applied. We are then able to accurately count the change in the number of probes from one set of images/conditions to the next.

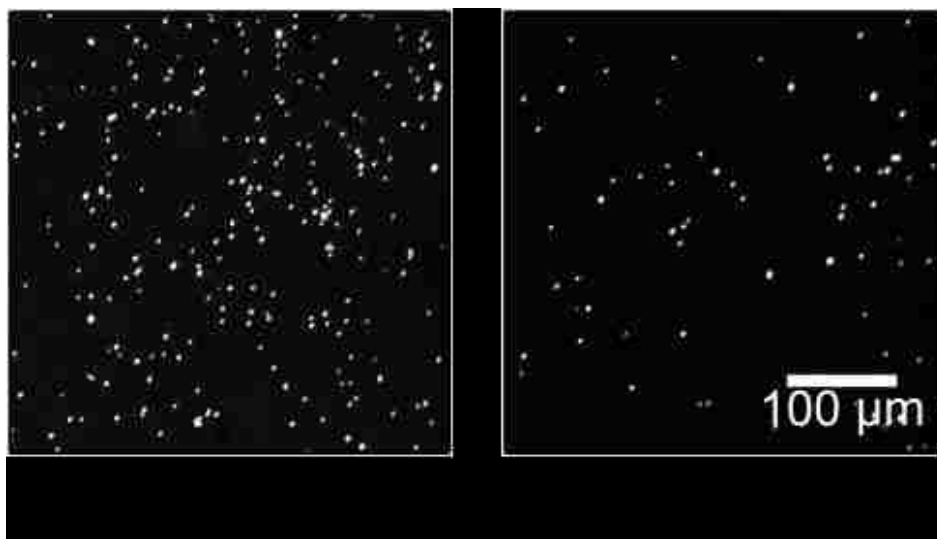


Figure 3.9 Representative images from bead binding assay. The probes were allowed to settle onto the surface via gravity (left image) and a permanent magnet was used to remove the probes (right image). This particular experiment was conducted on a SAM of MHDA on gold in a solution of pH 7.0 phosphate buffer with an ionic strength of 1 mM.

Figure 3.10 shows a summary of all the results analyzing the effects of altering surface and solution chemistry on the binding of probes to a substrate. It is obvious from all the force curves that as the pH increases the system becomes increasingly repulsive. The

probe binding assays show that the probes become repulsive only at high pH ($\text{pH} > 5$). Variations in the ionic strength of the solution achieve a similar effect. To prevent significant binding the probes need to be placed into solutions of an ionic strength less than 100 mM. By altering the surface potential from 25 mV for MutEG to 35 mV for MHA SAMs, we did not observe many probes remaining.

To understand effect of the attractive van der Waals interactions, we then deposited different lengths blocking molecule SAMs on the surface. This analysis has given three pieces of information. The probe binding experiments conducted in a solution with a pH 3 and 100 mM ionic strength. We chose the solution that has pH of 3 to neutralize the acid groups on the probe and the surface, thus nearly eliminating all long-ranged repulsion in the system. The experiment yielded close to 100 % binding for all blocking layers from zero to eleven-carbon chains. It is not until the MDHA (a sixteen-carbon chain) is used as a blocking layer that a reduction from the almost complete adhesion is observed (consistent with our theoretical modeling). This consideration argues that, in the case of SAMs on Au surface chemistry, to produce a surface for use in massively parallel force spectroscopy, it is very important to have a long blocking layer to reduce the non-specific binding.

From this set of data we can determine that to bring the probe within 12 nm of the surface without it adhering would require a pH greater than 6, and ionic strength of around 100 mM, a surface potential from 25 mV and a long blocking molecule.

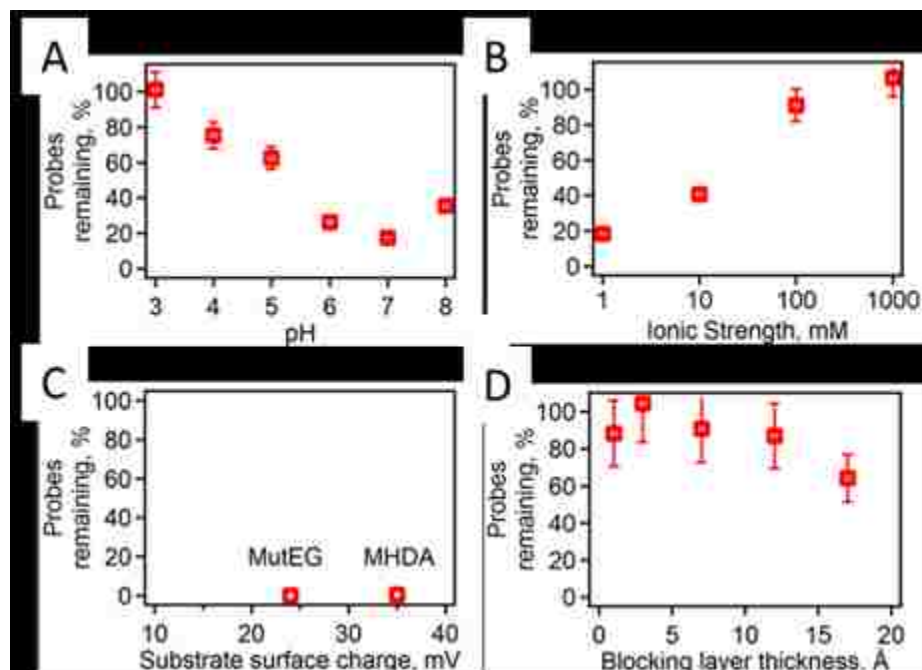


Figure 3.10 The effects of changing the pH with a constant ionic strength of 1 mM on an MHA surface (a), the solutions ionic strength with a constant pH of 7 on an MHA surface (b), and the surface potential with constant pH of 7 and ionic strength of 1 mM (c). The results of the probe binding assays (c) show the levels of adhesion for the different thicknesses in a series of carboxyl-terminated SAMs (formed by HS-(CH₂)_n-COOH, n=2, 5, 10, 15) at pH 3.

To study the effects of the surfactant (in this case Tween 20) on the system, we chose biological conditions close in value to the optimal conditions determined earlier: a MutEG surface and a solution with pH=7.4 and an ionic strength of 174 mM. To test the effects of the surfactant, we added Tween 20 up to 0.1 % v/v to these high ionic strength solutions and conducted binding assays. We were able to see a decrease in the adhesion of probes to the surface. Increase in the concentration of Tween 20 show a dramatic drop (from 100 to 5-15 %) in the number of probes left on the surface after a magnet is applied and should greatly increase the number of active probes in our system (up to 95 % of the

total population). These data indicate that to maximize the number of active probes in a bead-based platform (necessary for accurate and simultaneous force spectroscopy on a high number of molecules), it is highly advantageous to include non-ionic surfactant when one needs to work with solutions of high ionic strength (~ 100 mM).

3.4.5 Ordered single-molecule-bead assemblies

Use of the flat support surfaces leads to random arrays. For microscopic beads, a straightforward way to achieve high density of probes with predefined spacing is to use an array of microwells to arrange the beads in the regular pattern and then link them to DNA attached at the bottom surface of the wells. Figure 3.11 illustrates the implementation of this format for ordered bead-molecule arrays.

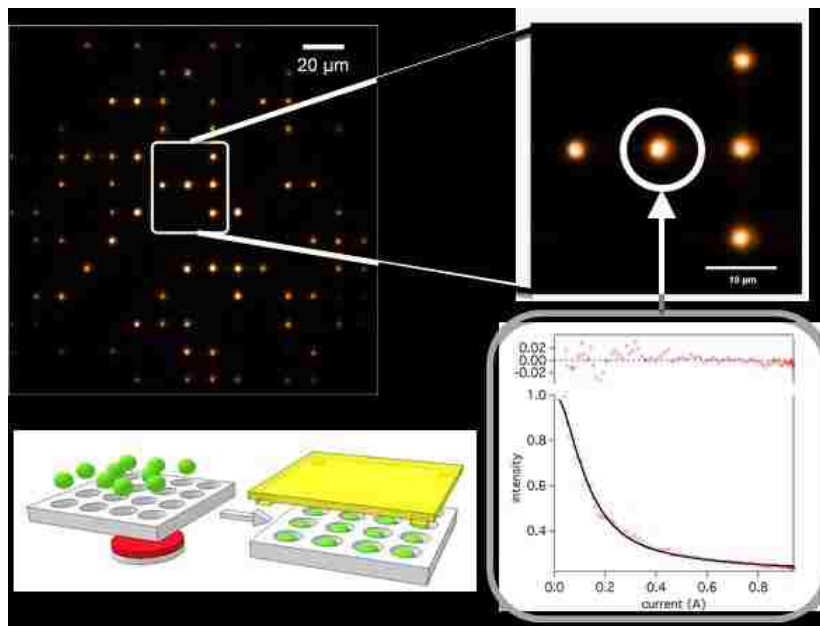


Figure 3.11 Proposed scheme for a force spectroscopy array comprises an array of wells accommodating a single magnetic bead per well, with each bead in turn attached to a single oligomer. Application of a permanent magnet readily forces magnetic beads inside

the wells. Plots of intensity (decreasing with distance) vs. current for magnetic tweezers or voltage squared for DEP tweezers (proportional to force) are generated for individual beads. Uneven brightness of the beads in large area images reflects Gaussian intensity distribution in the laser beam illuminating the sample. Variations in the intensity of the neighboring beads reflect differences in their size and exact positioning inside the well.

3.5 Conclusions

We have successfully designed a single-molecule-bead chemistry with which we are capable of perform parallel force spectroscopy on almost 80 % of the probes bound to ssDNA. We used a general method for spacing thiol-modified DNA by means of a competitive binding with a thiol forming a blocking layer. The creation and tuning of a system for highly parallel force spectroscopy requires a non-trivial balance of many factors involved with the surface and solution chemistry of the system.

We were able to establish the guidelines for tuning the solution and surface chemistry of the flow cell by modeling the forces acting on the probes using DLVO theory, as well as AFM measurements and bead binding experiments. We have determined that the optimal conditions for specific binding include a long blocking layer (approximately 2 nm in thickness), a solution ionic strength in the range of 10-100 mM, and a surface potential of the surface and probe approaching 35 mV. The use of a non-ionic surfactant at low concentration (0.01-0.1 %) is critical to prevent adhesion of probes after they contact the surface. In our experiments, we used either addition of NaCl or change in the concentration of the phosphate buffer to control the ionic strength. In some biological systems divalent cations (such as Ca^{2+} and Mg^{2+}) are important to certain biological structures or processes. For example, the melting point of dsDNA is raised in the

presence of those divalent ions and Mg^{2+} is required for the function of the DNA polymerase. Since one expects the effects of these divalent cations on ionic strength and the adhesion of the probes to the surface to be more pronounced than for monovalent cations, adjustments to the ionic strengths of the solutions should be made to optimize the experimental conditions. With improvement to the yield in assembling active bead-biomolecule pairs in an organized bead array, this single-molecule-bead chemistry can be used to conduct parallel force spectroscopy on a variety of complex biological systems.

Chapter 4 : Dielectrophoretic Tweezers as a Platform for Molecular Force

Spectroscopy in a Highly Parallel Format

*The work described in this chapter has been published in P. Cheng, M. J. Barrett, P. M. Oliver, D. Cetin and D. Vezenov, Dielectrophoretic tweezers as a platform for molecular force spectroscopy in a highly parallel format, *Lab on a Chip*, 2011, 11, 4248-4259.*

4.1 Introduction

Molecular force spectroscopy (MFS) is a major research tool for studying inter- and intra-molecular forces, including biomolecular recognition,^{31, 32} the energy landscapes of protein folding,^{75, 76} and energetic barriers of the conformational changes in biomolecules.^{77, 78} A typical force spectroscopy experiment often involves binding one end of a molecule to a surface of a rigid support and the other to a mobile force probe (commonly a tip of an atomic force microscope (AFM) or a microsphere used in optical tweezers)^{18, 22} followed by controlled displacement of the probe to obtain a force-extension curve.¹⁹ In MFS experiments, hundreds of measurements must be collected on the same system in order to provide sufficient data for averaging and statistics or to uncover multiple unique mechanical pathways or states of the system. This experimental process is often time-consuming and cannot be readily extended to a parallel format, especially if chemically-distinct molecules are to be analyzed, since a different optical trap or AFM tip will be needed for multiple molecular species. Alternatively, magnetic tweezers provide an opportunity to acquire large amounts of data by simultaneously applying a magnetic field to multiple magnetic colloidal probes.^{34, 35} thereby applying a controlled force in parallel. However, the challenges in this case are the difficulty in

fabrication of the monodisperse superparamagnetic probes, need for close proximity of the magnetic field concentrator to achieve high forces, and limited sample area where uniform force application can be achieved. These drawbacks led us to propose a massively parallel MFS technique based on dielectrophoresis (DEP), in which the force on the probes is evenly applied to all the probes in the system. We showed that by perturbing the electric field with dielectric microstructures one can generate DEP forces in the range of several hundred piconewtons acting on microscopic probes across a macroscopic sample area (1-100 cm²). The magnitude and direction of the force can be manipulated by controlling the amplitude and frequency of the electric field.

In this chapter, I describe an implementation of dielectrophoretic tweezers using parallel flat electrodes to manipulate an array of polymer force probes. Instead of fabricating complex micro-electrode arrays to generate the field gradients necessary to manipulate particles with DEP (a common approach for applications of dielectrophoresis with biological samples),^{79, 80} we used a single set of macroscopic electrodes to generate high electric field gradients in the vicinity of the sample surface by using simple microfabricated dielectric structures (microwells) on one of the electrodes. Near a planar electrode, the force probe itself (a dielectric microsphere) can also serve as such a microstructure thereby creating the electric field gradient necessary to generate a force. We evaluated the performance characteristics of several possible designs for DEP tweezers using numerical analysis, fabricated a prototype, and then used this chip-based force spectroscopy technique to stretch single stranded DNA (ssDNA). Since we are using large area metal surfaces as electrodes, we can achieve a uniform potential

distribution and reproducible field gradients throughout the whole working area of the device, thus, making this approach ideally suited for highly parallel measurements.

4.2 Theoretical background of DEP

The DEP phenomenon occurs when a dielectric material (in our case, a polymer microsphere) is exposed to a non-uniform electric field. In the presence of electric field, the dielectric microspheres is polarized acquiring an induced dipole moment. Before we describe the results of the analysis of force using numerical methods, it is instructive to review a simple picture of a net force experienced by a small physical dipole in vacuum (Figure 4.1). The simple dipole has two equal and opposite charges $+q$ and $-q$. The dipole is placed in an electric field E and two charges are a vector distance \vec{d} apart.

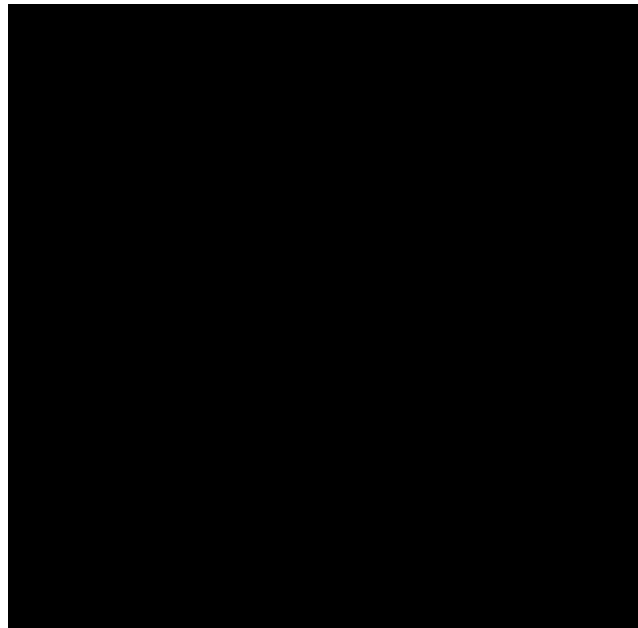


Figure 4.1 Net force acting on a small physical dipole placed in a non-uniform electric field.

We assume that the dipole itself has no effect on the imposed field, which implies that the scale of nonuniformity of the electric field is much larger than vector distance \vec{d} (so that $\vec{E}(\vec{r} + \vec{d}) \cong \vec{E}(\vec{r})$, where \vec{r} is the position vector of $-q$ charge. The energy is equal to the work done by the field to separate the charges by vector \vec{d} in an external electric field \vec{E} .

$$U = -q\vec{E} \cdot \vec{d} = -\vec{p} \cdot \vec{E} \quad (4-1)$$

where $\vec{p} = q\vec{d}$. Then the net force can be expressed as the derivative of the energy along the direction of the small physical dipole in the field gradient:

$$\vec{F} = -\vec{\nabla}U = \nabla(\vec{p} \cdot \vec{E}) \quad (4-2)$$

For a rigid dipole, which has a fixed charge separation \vec{d}

$$\vec{F} = q\vec{d} \cdot \nabla\vec{E} \quad (4-3)$$

$$\vec{p} = q\vec{d} \quad (4-4)$$

$$\vec{F} = \vec{p} \cdot \nabla\vec{E} \quad (4-5)$$

where \vec{p} is the finite dipole moment. The conclusion we can draw from the equation is that the particle (induced dipole) has to be placed in a nonuniform electric field to experience the net force.

In order to calculate the net force, we will use the effective moment method to calculate \vec{p} . When a dielectric particle is located in an electric field, the field polarizes the particle. This induced dipole then generates electrostatic potential, as shown in Figure 4.2. Two point charges $+q$ and $-q$ are suspended in the medium with permittivity ϵ_1 . Let

us consider where r is the radial coordinate and θ is the polar angle in spherical coordinates.

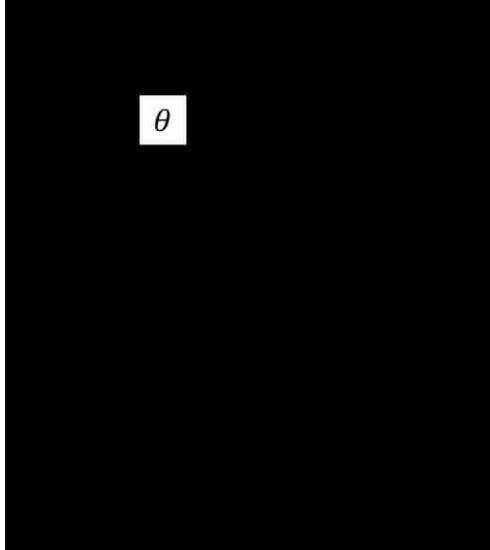


Figure 4.2 A small physical dipole suspended in medium with permittivity ϵ_1 . r_+ and r_- are the radius reference to an arbitrary point.

The electrostatic potential is a sum of the electric potential due to two point charges:

$$\Phi(r, \theta) = \frac{q}{4\pi\epsilon_1 r_+} - \frac{q}{4\pi\epsilon_1 r_-} \quad (4-6)$$

Using the law of cosines, we can write:

$$r_+^2 = \left(\frac{d}{2}\right)^2 + r^2 \pm 2 \cdot \frac{d}{2} r \cos \theta \quad (4-7)$$

$$\frac{r}{r_{\pm}} = [1 + \left(\frac{d}{2r}\right)^2 \pm \frac{d}{r} \cos \theta]^{-1/2} \quad (4-8)$$

We can now expand the equation using Maclaurin series:

$$(1 + x)^{-1/2} = 1 - \frac{x}{2} + \frac{3x^2}{8} - \frac{5x^3}{16} + \dots \quad (4-9)$$

$$\frac{r}{r_{\pm}} = P_0 \pm \left(\frac{d}{2r}\right) P_1 + \left(\frac{d}{2r}\right)^2 P_2 \pm \left(\frac{d}{2r}\right)^3 P_3 + \dots \quad (4-10)$$

where P_i are the Legendre polynomials. Combining equations results in:

$$\Phi(r, \theta) = \frac{qdP_1(\cos \theta)}{4\pi\epsilon_1 r^2} + \frac{qd^3 P_3(\cos \theta)}{16\pi\epsilon_1 r^2} + \dots \quad (4-11)$$

$$P_1(\cos \theta) = \cos \theta \quad (4-12)$$

$$\Phi_{\vec{d}} = \frac{p \cos \theta}{4\pi\epsilon_1 r^2} \quad (4-13)$$

where the solution of Legendre polynomials of P_1 (indicating there is only one induced dipole, instead of higher order multipoles) is $\cos \theta$, and the electric potential of the dipole can be calculated using the effective dipole moment $p = qd$. We can then solve for the electric potential and effective dipole moment using boundary conditions. Let us apply electric field \vec{E}_0 is applied to the system (Figure 4.3). Assuming the dielectric particle does not substantially disturb the electric field, the electrostatic potential equations should satisfy Laplace's equation: $\nabla^2 \Phi = 0$.

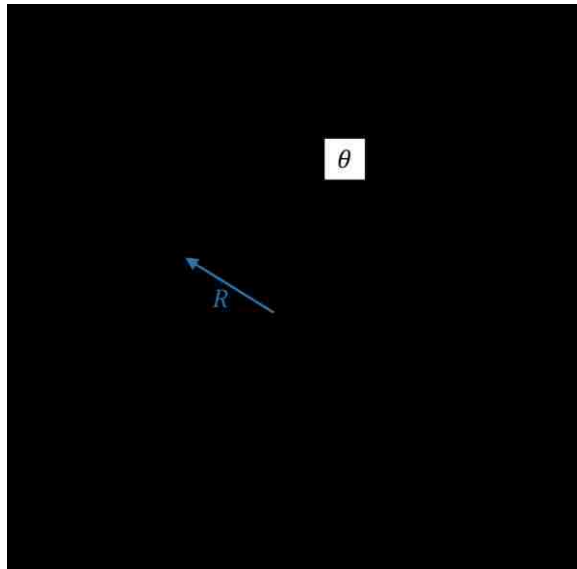


Figure 4.3 Dielectric particle with radius R and permittivity ϵ_2 is suspended in dielectric medium with permittivity ϵ_1 .

The solutions are:

$$\Phi_1(r, \theta) = -Er \cos \theta + A \frac{\cos \theta}{r^2}, r > R \quad (4-14)$$

$$\Phi_2(r, \theta) = -Br \cos \theta, r < R \quad (4-15)$$

where A and B are the coefficients we need to evaluate. Since the electrostatic potential and the electric displacement have to be continuous cross the particle-medium interface, we can then apply the boundary conditions at $r = R$:

$$\Phi_1(r = R, \theta) = \Phi_2(r = R, \theta) \quad (4-16)$$

$$-\varepsilon_1 \frac{\partial \Phi_1}{\partial r} = -\varepsilon_2 \frac{\partial \Phi_2}{\partial r} \quad (4-17)$$

$$\varepsilon_1 E_1(r = R, \theta) = \varepsilon_2 E_2(r = R, \theta) \quad (4-18)$$

We then obtain A and B. By comparing the solution of A and B to equation (4-13), we can calculate the effective dipole moment.

$$A = \frac{\varepsilon_2 - \varepsilon_1}{\varepsilon_2 + 2\varepsilon_1} R^3 E \quad \text{and} \quad B = \frac{3\varepsilon_1}{\varepsilon_2 + 2\varepsilon_1} E \quad (4-19)$$

$$p = 4\pi\varepsilon_1 A \quad (4-20)$$

$$p = 4\pi\varepsilon_1 CM(\varepsilon_1, \varepsilon_2) R^3 E \quad (4-21)$$

where $CM(\varepsilon_1, \varepsilon_2)$ is called Clausius-Mossotti (CM) factor.

$$\vec{F} = \vec{p}_{eff} \cdot \nabla \vec{E} = 4\pi\varepsilon_1 CM(\varepsilon_1, \varepsilon_2) R^3 E \cdot \nabla \vec{E} \quad (4-22)$$

The CM factor describes the total redistribution of charge throughout the system and takes into account the polarizabilities and the conductivities of both the particle and the medium.

$$CM(\tilde{\varepsilon}_p, \tilde{\varepsilon}_m) = \frac{\tilde{\varepsilon}_p - \tilde{\varepsilon}_m}{\tilde{\varepsilon}_p + 2\tilde{\varepsilon}_m} \quad (4-24)$$

where $\tilde{\epsilon}_p$ and $\tilde{\epsilon}_m$ are the complex dielectric constant of the particle and the medium, respectively. The complex dielectric constants depend on both the conductivity (σ) (of the polymer itself and the electric double layer) and the relative permittivity (ϵ_r) of the material, as well as the frequency of the AC field (f) and is given by:

$$\tilde{\epsilon} = \epsilon_0 \epsilon_r - i \frac{\sigma}{2\pi f} \quad (4-25)$$

An important aspect of the CM factor is that it introduces frequency dependence of the DEP force that one can potentially use to tune the magnitude of the DEP force or even reverse its direction. When $Re(CM)$ value is positive (i.e. particle is more polarizable than the medium), the particle will move towards the high electric field, and the effect is termed positive DEP. In contrast, negative DEP occurs when the value of the real part of the CM factor is negative (i.e. medium is more polarizable than the particle), inducing the particle to move towards the low electric field. As a result, this physical relationship can be exploited to either push or pull on a polymer microsphere in an aqueous medium.

Figure 4.4 shows the calculated frequency dependence of the CM factor expected for the polymer-only microspheres used throughout this thesis, in an ideal water environment assuming formation of an electrical double layer. As we discussed above, the frequency necessary to switch the DEP direction from positive to negative for colloidal probes in aqueous solutions lies around the 1 MHz range, which is easily obtainable with off-the-shelf function generators. This swappable force direction enables application of the proposed DEP tweezers in a wide range of different systems; for example, one can use the tweezers to trap and then release polymer particles or whole cells.

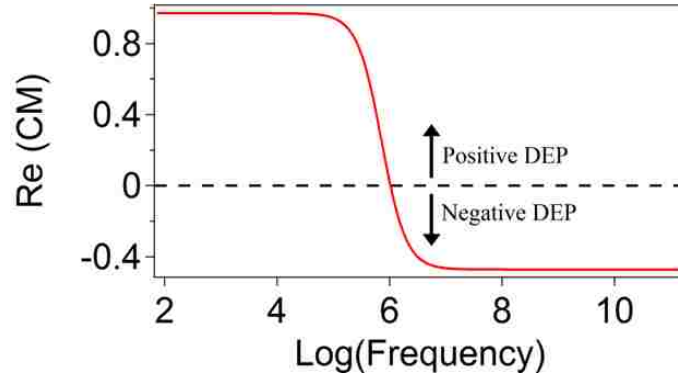


Figure 4.4 Calculated frequency dependence of the real part of the Clausius-Mossotti factor for a dielectric particle typical to our system ($\epsilon_m/\epsilon_0 = 78, \sigma_m = 10^{-5} \text{S} \cdot \text{m}^{-1}$; $\epsilon_p/\epsilon_0 = 3.0, \sigma_p = 10^{-3} \text{S} \cdot \text{m}^{-1}$). The probe experiences a positive DEP force when the frequency is below 1 MHz, while a negative DEP force acts on a probe when the frequency of applied AC field is above 1 MHz.

The real part of CM factor is the determining factor for DEP force and the imaginary part is the determining factor for electrorotation torque. We finally get the expression for the first order approximation DEP force:

$$\vec{F} = 2\pi R^3 \epsilon_m \text{Re}(CM) \nabla E^2 \quad (4-23)$$

where ϵ_m is the dielectric constant of the medium, $\text{Re}(CM)$ is the real part of the CM factor, and ∇E_{rms}^2 is the gradient of the electric field squared.

The effective dipole moment approximation breaks down when the scale of nonuniformity of the electric field is comparable to the size of the dipole, as is the case for our system. One then needs to use linear multiples to describe the effective moment. The n th order induced linear multipole will experience a force:

$$\vec{F}_n = q_n (\vec{d}_n \cdot \nabla)^n \vec{E} \quad (4-26)$$

where q_n is charge of the n th order multipole. The most rigorous approach, Maxwell stress tensor (MST), is often used to calculate the electric field induced force. Due to the mathematical complexity of calculating MST, we chose to use numerical analysis to evaluate the DEP force.

4.3 System Design

To produce a DEP force, one needs to form electric field gradient in the sample volume of interest. Commonly, closely positioned micropatterned electrodes are used to create a non-uniform electric field capable of generating a DEP force. As an alternative to this method, it is possible to perturb the electric field with a dielectric structure (including the particle that one is trying to manipulate)^{81, 82}.

A system of two parallel large area electrodes produces a uniform electric field and no DEP force is expected for a single microsphere suspended in the space between these electrodes. When the sphere is close to the surface of one of the electrodes (distance \ll particle size), an imbalance of the field gradient is created on the two sides of the probe (facing the solution and facing the electrode), generating a net DEP force normal to the substrate. When the sphere moves farther away from the electrode's surface (on the order of the probe radius), the classical picture emerges and the DEP force disappears. This phenomenon is ideally suited for use of large (micron size) probes to pull on molecules having contour lengths on the order of hundreds of nanometers attached to flat surfaces, since the probe will always remain close to the surface compared to its size. An assembly of microspheres on a planar electrode due to DEP

forces has been previously investigated^{83, 84}, although only lateral inter-particle forces were of interest in this case.

Flat electrodes as described above are not always ideal to conduct parallel force spectroscopy experiments, because (i) they do not provide for the optimization of the magnitude of the forces and (ii) they create a random array of probes that lack the organization to process data on a very large scale. To maximize control over the DEP forces, as well as introduce order to the array, we can consider the creation of a patterned electrode array and the perturbation of the electric field with a dielectric structure integrated into the large area electrode. Creating patterned electrode arrays may involve sophisticated fabrication methods and raises possible alignment issues (e.g. position of the probe with respect to electrode will affect the magnitude of the force), thus increasing the cost and degree of difficulty needed to fabricate and operate a cell for DEP tweezers working on a large scale. Alternatively, to perturb the electric field, a dielectric obstacle can be placed inside the otherwise uniform field^{85, 86}, such as a microfabricated solid structure, for example, a microwell array. For these reasons, we chose to focus solely on the design of dielectric patterns to form the electric field gradient. Figure 5 diagrams four such electrode configurations all capable of delivering DEP force. We have conducted theoretical simulations and experiments to characterize the DEP forces for all four configurations of the electrodes.

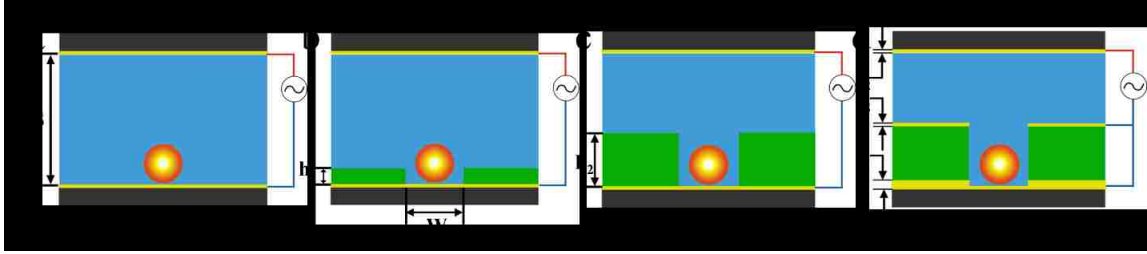


Figure 4.5 Various cell designs for DEP tweezers. (a) Geometry A: A probe above a flat electrode. (b) Geometry B: A probe in a shallow microwell fabricated on top of an electrode (well depth $h_1 <$ bead diameter). (c) Geometry C: A probe inside a deep microwell fabricated on top of an electrode (well depth $h_2 >$ bead diameter). (d) Geometry D: A microwell on top of a thick gold layer (thickness $t_1=135$ nm), whose primary purpose is to block the light from entering the photoresist layer making layout suitable for TIRFM detection. The thin gold layers (thickness $t_2=14$ nm) act as the electrodes. The standard dimensions for all wells used in this work had $w=4.2$ μm and $s=24$ μm (unless varied on purpose). The center-to-center distance for the wells was 44.2 μm .

There are several advantages to the use of the microwell format shown in Figure 4.5b-d. First, when the probe is positioned inside a well, there are several interfaces where dielectric constant experiences a significant jump. When potential is applied between two planar gold electrodes, the electric field will be strongly perturbed by the dielectric contrast of three different materials (the probe, the medium, and the microwell), resulting in a high electric field gradient inside the well. Second, this approach to generation of the DEP force only relies on conventional fabrication of the microwell arrays by a single step contact photolithography. Third, the wells will also provide a high degree of order for arrangement of the probes on the surface of the DEP cell to simplify indexing of the array and subsequent analysis. Finally, placement of the microspheres inside individual wells results in the added stability of the setup during fluid exchanges, which may be necessary to conduct biochemical reactions/binding without removing the

probes. The shear force on a single force probe is minimized during exchange (flow) of the solution above the surface of the microwell array.

In order to create a system for molecular force spectroscopy that can accommodate a large number of individual experiments and applies an adjustable DEP force to each molecule at the same time, we mounted a DEP chip inside a fluid cell that is accessible for optical observations and enables controlled dosing of microscopic force probes and reagents. Wide field optical microscopy ensures simultaneous observations of multiple probes. Integration with microfluidics minimizes the volume of reagents used, so that the total cost of conducting single molecule pulling experiments is greatly reduced, which is important if the DEP tweezers are to be used in a bioanalysis assay.

4.4 Numerical simulation

To investigate the magnitude of the DEP force in each variation of the DEP tweezers arrays, we used a finite element method software package (COMSOL Multiphysics, Burlington, MA). Due to the constraints of the size and complexity of the problem, and demands on computational time for the simulations of the electric field in the space around the probe and electrodes, the majority of our simulations were conducted as two dimensional (2D) approximations. In order to examine the accuracy of 2D simulation, we compared results from four types of simulations: 2D, reduced 3D (2D with axial symmetry), and full 3D with a round or square well (Fig. 6). In 3D calculations, the number of degrees of freedom is dramatically greater than in 2D calculations; therefore, an optimal choice of the proper model is critical to reduce computation time.

A standard simulation consisted of two 44.2 μm wide electrodes separated by 20 μm (unless specified otherwise) of deionized water. On the lower electrode 4.2 μm wide dielectric wells (consisting of SU-8) were simulated with depths of 2, 4, 6, and 8 μm with rounded corners (0.2 μm curvature) to reduce sharp edge effects not present in experiment. To represent the format of an array, the left and right boundaries of the cell were set to a periodic condition to repeat the structure infinitely. To simulate the force on a probe a PMMA sphere was placed inside the well just above the surface of the electrode. For the entire system physical values for the relative dielectric constants were used. A quasi-static potential field was simulated from the Laplace equation $\nabla^2 V = 0$ (V is the voltage) for surface potentials of +5 and -5 V. The 3D calculations share the same parameters with the 2D simulation. Both a square shaped well and a round shaped well were modeled in 3D.

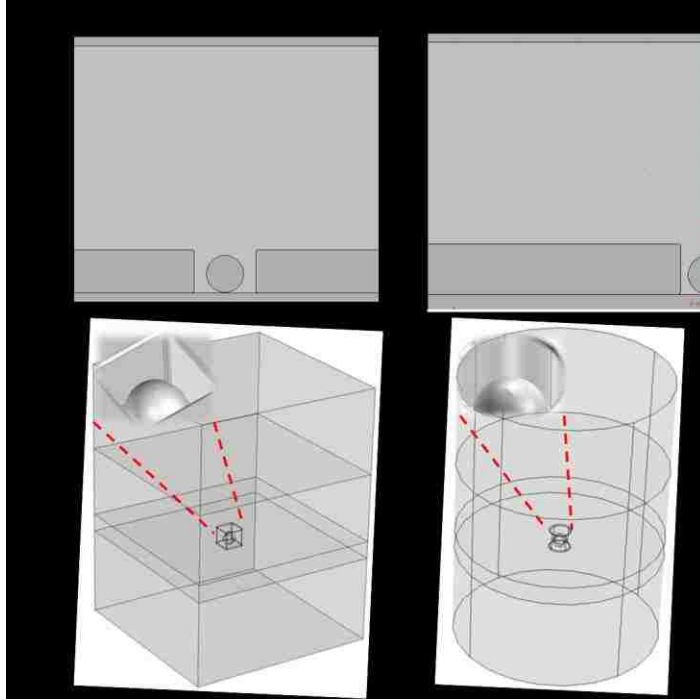


Figure 4.6 Geometry of simulations for a square well in full 3D (a, c) and a round well in reduced 3D (b, c) simulations.

In both 2D and 3D simulations, we solved a variant of Poisson's equation for potential distribution:

$$-\nabla \cdot (\epsilon_0 \nabla V - P) = \rho \quad (4-27)$$

in the electrostatics module. Here V is the electric potential, P is the electric polarization vector, and the ρ is the electric charge density.

Besides using the first order approximation -- effective dipole moment (EDA) model, which results in Equation 1, we also used a rigorous model and obtained the force by integration of the Maxwell stress tensor (MST) over the surface of the probe. The general form for the time-averaged net DEP force resulting from the MST method is:

$$F_{DEP} = \frac{1}{4} Re(\tilde{\epsilon}_m) \oint_A ((\vec{E}\vec{E}^* + \vec{E}^*\vec{E}) - |E|^2 U) \cdot \vec{n} dA \quad (4-28)$$

where A is the surface area of the probe, \vec{E} is the electric field outside the probe and U is the unit tensor.

We investigated the accuracy of two different integration methods for derivation of a DEP force. We first looked at the sensitivity of the numerical results to different mesh sizes. The size and the height of the wells, the separation between two electrodes and the diameter of the probes have the same values as the standard parameters mentioned in the main text. The probes were set at 50 nm above the bottom of the well. The DEP forces obtained by both EDA and MST methods converged to constant values when the mesh size was smaller than 25 nm (Figure 4.7). We then kept 25 nm as a meshing parameter in the following calculations.

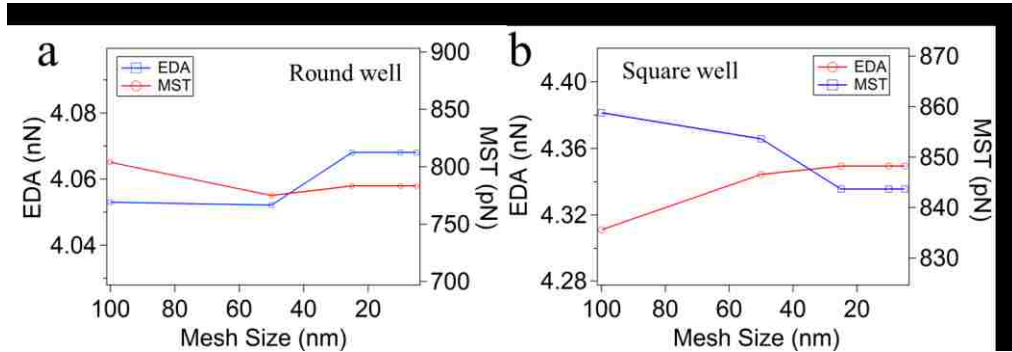


Figure 4.7 DEP forces for beads in Geometry C calculated using EDA and MST methods are plotted versus the mesh sizes for 3D simulation with a round well (a) and square well (b). The potential was set to 10 V (peak to peak).

EDA model considers the probe as a single dipole. This approximation is normally sufficient for cases where the electric field does not change appreciably over distances comparable to probe size. We verified the results obtained using the EDA model by

carrying out rigorous MST calculations on the same systems. Figure 4.8 represents the results of the calculations of the DEP force in the setups shown in Figure 6 above.

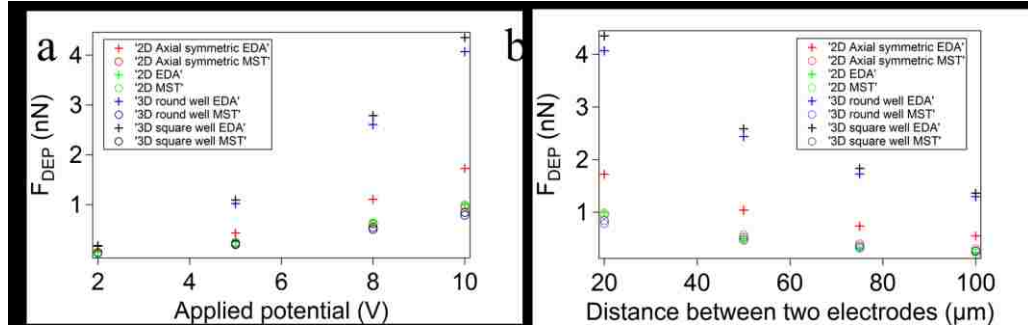


Figure 4.8 Both of EDA and MST methods are used for calculation of the DEP force. (a) The DEP force varies as a function of applied potential while the electrode separation was set at 20 μm . (b) Change in the DEP force with respect to the distance between two electrodes while the applied potential was set at 10 V.

Both methods showed convergence to constant force values for mesh sizes below 25 nm. After we integrated the MST over the surface, we multiplied the resulting force by the maximum real part of the CM factor, which is equal to 1 for positive DEP and 0.5 for negative DEP. We found that the MST method produced very similar results for all models; forces for full 3D round and square well models agreed within 3-8 %, whereas reduced 3D or 2D models were different from the full 3D results by 15-20 % of the total force (with a potential varied between 1 and 10 V and electrode separations varied between 20 and 100 μm). In contrast, the EDA method, which assumes a slowly varying electric field (compared to the probe size), overestimated the forces by a factor of 1.8 (reduced 3D) or 5 (full 3D) with respect to the MST results. Since the results between the full and reduced 3D methods showed adequate agreement in the magnitude of forces, we used the reduced 3D method in all simulations unless otherwise noted.

Two parameters were varied in those calculations. When the applied potential between two electrodes increases, DEP force exerted on the probe increases (Figure 4.8a). When the distance between two electrodes increases, DEP force diminishes (Figure 4.8b). Forces calculated using MST-based approach cluster very tightly and show self-consistency between all models. However, the EDA results span a wide range of DEP force values for the same geometry and set of parameters (could differ by > a factor of 4), indicating that EDA is only a first order approximation that will overestimated the DEP force for all 3D models. Only the 2D model produced similar results for DEP forces with both EDA and MST methods. We can conclude that 2D simulation for force calculations using MST integration is the optimum approach to balance requirements on the computation time with the accuracy when simulating various DEP tweezers designs.

4.5 Experimental methods

4.5.1 Fabrication of the DEP chip

The general strategy of fabricating an array of wells on a cover glass is shown in SI, Fig. S3. A round (40 mm diameter) cover glass (Warner Instruments, MA) was cleaned in Piranha solution (a 3:2 mixture of 98 % H₂SO₄ : 30 % H₂O₂) for 40 minutes. The cover glass was rinsed with deionized (DI) water and blown dry with filtered nitrogen. Titanium (4.5 nm) and gold (11 nm) films were deposited on the glass surface using an e-beam evaporator (Eddy Co. SYS-24, SC-20-Digital System Controller). The gold-coated cover glass was then cleaned by air plasma (Harrick Plasma, Ithaca, NY) on a high power setting for 1 min. SU-8 3005 resist (Microchem Co., MA), was used to construct wells of

desired depth and size on the gold-coated cover glass following the procedure recommended by the manufacturer. The cell compatible with TIRF observations required two extra fabrication steps. In order to block the light from propagating in the SU-8 and interacting with the probe, a 130 nm gold film was first deposited instead of the 11 nm gold layer (using the e-beam evaporator). We calculated that the transmission of light through 130 nm gold layer is less than 0.1%. After exposure and development of the SU-8 pattern, the thick gold layer at the bottom of the well was etched using a standard gold etchant (4 g KI, 1 g I₂, and 80 mL DI-H₂O), as confirmed by transmission microscopy. A final thin transparent gold film (4 nm titanium and 15 nm gold using an e-beam evaporator) was deposited, coating primarily the bottom of the well and the top of the SU8 resist, for use with the thiol-on-gold immobilization chemistry. The initial gold layer under the SU8 will block the light from reaching any probe that may reside on the surface of the resist.

4.5.2 Probe fabrication and activation

The fluorescent microspheres were synthesized by micro-emulsification of PMMA solutions that contained 1-oxazine (see Chapter 2). The probes were washed three times with 1 mL of 100 mM MES (2-(N-morpholino)ethanesulfonic acid, MP Biomedicals) pH 5.4 buffer, centrifuged, and resuspended in the same buffer in a 1.5 mL centrifuge tube. For attachment to ssDNA molecules, the probes were activated for 15 min by adding 10 mg of 1-ethyl-3-(3-dimethylaminopropyl)carbodiimide (EDC) and 10 mg of N-hydroxysulfosuccinimide (sulfo-NHS) to suspension. The probes were washed three

times with 1 mL pH 8.0 phosphate buffer containing 0.1% TWEEN 20 (Calbiochem) before they were flushed into the cell.

4.5.3 End-modification of DNA

Our ssDNA oligomer was 142 base pairs long (82 nm) and produced in-house using standard ligation techniques. The model DNA contained 5'-amine and 3'-thiol end modifications (5'-NH₂-(CH₂)₆- TG TAG AGA CGT CGA CAG CTC ACA CTC GCA TAC GAG ACT ATA GTA CGT ATC GAT ACG TCA TCT GAT CAC GCA CGC ATA TGT AGA GCT AGT GAG CAC GTC GAT ATG ACA TGA TAG CAG TCG CTA GGT CAG ATC GTT CGA CTA GG -(CH₂)₃-S-S-CH₂CH₂OH-3'). The sequence was constructed in order to eliminate as much secondary structure as possible by randomly generating sequences with certain limitations. Namely, no repeats of any particular base more than three times in a row were allowed.

To create a 142mer ssDNA terminated with an amine on the 5' end and a thiol group on the 3' end, a 5'-amine terminated 71mer, a 3'-thiol terminated 71mer, and a 30mer complementary to 15 bases at non-modified ends of each 71mer (purchased from Integrated DNA Technologies) were annealed, and the 71mers were then ligated together. First, 4.5 μ L of 1 mM aqueous solutions of each DNA oligo were mixed with 10 μ L of an annealing buffer (100 mM Tris HCL, 1M NaCl, 10 mM EDTA) and diluted to 100 μ L with autoclaved DI water. The solution was denatured by undergoing a heat cycle of 2 min at 95° C in a thermocycler (Techne TC-3000) followed by five cycles of 95° C for 15 s, 40° C for 15s, and 72° C for 60 s. At the end of the last cycle the system was annealed

for 5 min at 72° C. This procedure resulted in 45 μM of DNA in a 100 μL solution. For ligation, 50 μL of the DNA solution were combined with 14 μL of 10x T4 ligase buffer and 18.75 μL of T4 DNA ligase (7500 units) (New England Biosciences), diluted to 150 μL with autoclaved DI water, and kept at 16 °C for 16 hours in the thermocycler. The product of ligation was separated from reaction mixture using a MinElute column (Qiagen) and eluted with 10 μL DI water. The DNA was purified from the 30mer and other side-products by a 6x TBE Urea gel (Invitrogen). After excising the band, the sample was eluted with 1x TBE buffer at 37 °C overnight. The final product was purified with a MinElute column and eluted with 20 μL of DI water. The final DNA concentration was 50 ng/ μL (~ 1 μM).

4.5.4 Substrate Preparation

The microwells were cleaned with air plasma for 1 minute, then placed in an ethanol bath for 10 min on a shaker table and finally dried with nitrogen. A self-assembled monolayer was formed by reacting a 1 mM aqueous solution of (11-mercaptopundecyl)tetra(ethylene glycol) (MutEG) with the Au substrate for 1 hour followed by a thorough DI water rinse. For single molecule stretching experiments with ssDNA, 1 μL of 1.5 μM solution of 142mer ssDNA was first unprotected by adding 4 μL of 5 mM tris(2-carboxyethyl)phosphine in 6 \times SSC buffer and incubating for 30 min. A competitive binding was then used to attach the DNA at a low density by placing 10 μL (5 μL of each) of 1:100 or 1:150 142mer ssDNA (mixture from previous step): MutEG (dissolved in 1 M NaCl PBS) mixture on the substrate for 2 hours. The DI water rinsed

and nitrogen dried substrate was then incubated in 1mM MutEG solution for another hour.

4.5.5 DEP cell assembly and microscope setup

The substrates were installed on the bottom side of a commercially available fluid cell (RC30, Warner Instruments) and a plasma cleaned flat gold substrate is installed on the top plate and sealed with vacuum grease (Figure 4.9a). A 30 mm long copper foil tape (32 μm thickness) was attached to the surface of each electrode. The top-plate and the bottom-plate were sealed together with a silicone gasket leaving a 100 μm gap. The two electrodes were then connected to a function generator (Model 645-G, BNC Co., CA). The cell was set onto a stage of the through-objective TIRF microscope (Olympus IX 71, equipped with 638 nm fiber optic coupled diode laser, (Coherent), Figure 4.9b). An excess of probes were added to the cell using an inlet port. The probes were then allowed to settle via gravity and those that did not occupy the wells were washed away. A fluorescent microscopy image (Figure 4.9c) showed more than 80% occupancy of the micro-wells after the probes were infused into the assembled fluid cell.

For non-specific binding experiments, the probes were suspended in 0.1% solution of TWEEN 20 in DI water or phosphate buffer (pH 7.4) at 1 or 10 mM total ionic strength and flushed into the microfluidic cell. For the frequency scan experiment on a flat substrate, the probes settled down close to the surface by gravity. A frequency sweep with different scan rates under a constant potential was applied to the two electrodes while a video was captured by a CCD camera (Andor Technologies, iXon DV888,

Belfast, Ireland). The number of probes and the integrated intensity of individual probes were calculated from analysis of the videos using custom code written in Igor Pro 6.2 (WaveMetrics, OR). Initial probe locations were found by thresholding the image and then (more accurately) from a fit to a 2-D Gaussian function. For each probe, a circular region of interest (ROI) was set around the center of the probe at a diameter of 10 μm (approximately five times the FWHM of the probe intensity profile). For each ROI, the background was first subtracted using a plane fit to a 1 μm -wide band surrounding the ROI. Probe intensities were then computed by numerical integration over the ROI. For ssDNA single molecule stretching experiment, the NHS-activated probes were flushed into the cell and settled down in the wells by gravity. The probes were incubated for 10 min inside the wells in order to attach to the ssDNA molecules (Figure 4.9b). A sinusoidal potential modulation was applied to the two electrodes to stretch the DNA while a video was recorded.

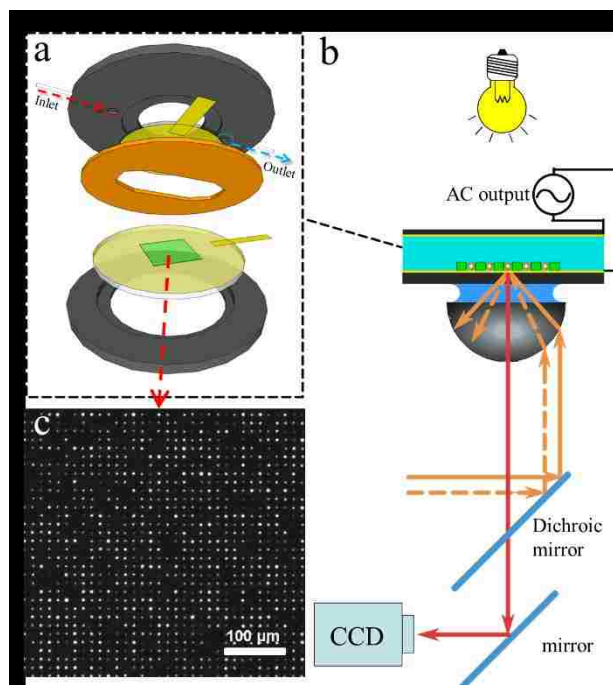


Figure 4.9 (a) DEP cell assembly and (b) setup in an optical microscope. The microwell pattern (green) is fabricated on top of the Au-coated glass cover slip (yellow). A sample is sealed with an elastomeric gasket (orange) against Au-coated electrode (yellow) and both are connected to a function generator via copper foil (rectangular yellow pieces). (b) The illumination in transmission mode helped to identify the edges of the microwells. CCD camera captures fluorescent images of the probes from a commercial TIRF setup integrated with a 638 nm laser. (c) Microscope image (10×) of the fluorescent probes assembled inside the microwells.

4.6 Results and Discussion

Molecular force spectroscopy provides information about a molecule's intra- and intermolecular forces through the measurement of force-distance profiles. The simulations and experiments described in this paper sought to determine the applicability of our DEP setup as a standalone force spectroscopy technique for parallel measurement. Three common aspects of force spectroscopy are usually considered: (i) a high force magnitude ($> 1\text{ nN}$) in a controllable direction (compression or extension), (ii) high force

resolution (~ 1 pN), and (iii) sensitive detection of molecular extension (< 1 nm). We addressed each of these aspects with respect to critical factors such as applied voltage, electrode separation, frequency of applied field, probe position, and microwell geometry.

4.6.1 Voltage dependence of DEP force

One can vary the DEP force exerted on the probe by adjusting potential difference between the two electrodes ($F_{\text{DEP}} \sim V^2$). We computed the DEP force for flat electrodes (Geometry A) through the MST integration by sweeping peak-to-peak voltage from 0 V to 10 V for the planar electrode cell. The results of the numerical analysis indicated an excellent agreement with the formal voltage dependence (a power law exponent of exactly 2) expected from the approximate model. Therefore, modulation of the DEP force can be readily achieved via the electrode potential. Using this method the force resolution would be defined by the resolution and stability of the driving electronics (for the simulated design, the relative noise in applied force should stay constant throughout voltage sweep, $\delta F/F = 2\delta V/V$, and 1 mV RMS noise will correspond to a 0.2 pN resolution at 10 V and 10 fN at 1 V). Since the shape of the field gradient is set by the geometry of the setup and the local field scales with voltage, this voltage dependence of the DEP force holds for all other chip designs, as we confirmed by simulations of the DEP force on probes placed in 4 μm deep microwells.

4.6.2 Effect of the spacing between two electrodes

At a fixed potential difference, the magnitude of the electric field, E , in the space confined by the large area electrodes depends on their separation, s (for parallel electrodes in Geometry A, $E \propto 1/s$ and $F_{DEP} \propto EV^2 \propto 1/s^2$). We found that the magnitude of the DEP force quickly decays with increasing distance between the two electrodes for both flat substrates and microwell designs. According to our simulations, for a 20 μm separation between electrodes, the DEP force of several hundred piconewton is readily achieved with both flat and micropatterned electrode configurations. For flat electrodes (Geometry A), the applied force dropped by two orders of magnitude, from 450 pN to 4 pN, (Figure 4.10) when the separation between electrodes increases from 20 μm to 200 μm . In contrast, when we placed a 3 μm diameter probe inside a 4 μm deep microwell (Geometry C, Figure 4.5c), the calculated force decreased gradually from 980 pN to 80 pN when electrodes moved apart from 20 μm to 200 μm .

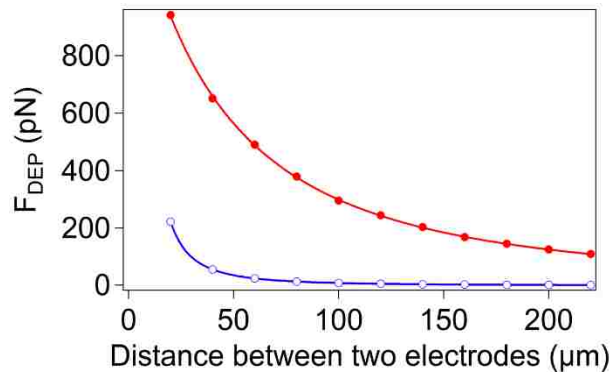


Figure 4.10 Simulation results of DEP force as a function of the electrode separation for probes placed 50 nm above the surface of a flat substrate (\circ), Geometry A, or the bottom of the microwell (\bullet), Geometry C. The parameters used for the simulation were 10 V peak-to-peak voltage with a 3 μm diameter probe. The curves represent the power law $F_{DEP} \propto 1/s^2$ for a Geometry A, where $n=1.987\pm 0.001$, and the square of a function in equation (4-23) for a Geometry B.

By fitting the DEP force decay for flat electrodes to a power law (Figure 4), we determined that $1/s^2$ relationship fits this decay precisely, implying that for large electrode separations ($s \ll R$) the distribution of the electric field in this geometry does not change with the electrode gap (i.e. $E(z,s) \approx V / s f(z)$), where function $f(z)$ characterizes electric field distribution for all s). For the microwells, the fit unexpectedly deviates from the $F_{DEP} \propto 1/s^2$ form (we obtained a best-fit exponent of 0.600 ± 0.033). We inspected numerical values of the electric field in the system and determined that this deviation is a result of our two layer arrangement (SU-8 and water). Since we are effectively using two parallel dielectrics in our system, the relative contributions (to the overall voltage between electrodes) of potential drops across each layer change with gap size causing a deviation from the expected power law. This effect is not present in a one-layer system. The electric field in the SU8 layer in this capacitor is:

For Geometry C, there are two layers with different dielectric constants in the capacitor. The total potential is:

$$V = E_{water} \cdot (S - h) + E_{resist} \cdot h \quad (4-29)$$

$$V = \frac{E_0}{\epsilon_{water}} \cdot (S - h) + \frac{E_0}{\epsilon_{resist}} \cdot h \quad (4-30)$$

$$E_0 = \frac{q}{\epsilon_0 \cdot A} \quad (4-31)$$

where q is the total charges on the electrode, ϵ_0 is the vacuum permittivity, and A is the area of the two electrodes.

The electric field in the photoresist should be:

$$E_{resist} = \frac{E_0}{\varepsilon_{resist}} = \frac{V}{s \frac{\varepsilon_{resist}}{\varepsilon_m} + h \left(1 + \frac{\varepsilon_{resist}}{\varepsilon_m}\right)} \quad (4-32)$$

where ε_{resist} is the dielectric constant of photoresist and ε_m is the dielectric constant of medium. By fitting the decay in the graph to the square of this function we see that the observed decrease in the DEP force follows a decay law related to the magnitude of the electric field in the resist.

The results from Figure 4.10 demonstrate that the DEP tweezers have a limitation on the maximum achievable force, requiring close proximity between the electrodes to attain a measurable DEP force. Although the force generated with a 20 μm gap for both flat and patterned electrodes is sufficient for most applications in force spectroscopy, the fabrication, handling, and storing components of such a device will pose some challenges. For example, it is hard to fabricate and handle a 20 μm thick elastomeric gasket to seal the DEP cell for fluid delivery. Therefore, to ensure an adequate range of forces (~ 100 pN) for Geometry A, the seal must be fabricated into one of the electrodes. On the other hand, the microwell geometry is not as sensitive to electrode separation and gaskets as thick as 100-200 μm appear suitable for a DEP cell, simplifying assembly of the microfluidic cell. For example, we successfully used a commercial fluid cell that places a polymer gasket between top-plate and bottom-plate to seal the system.

4.6.3 Frequency dependence of the DEP forces

Within any one of the DEP tweezers geometries, the microspheres can be pulled away from the surface or pushed towards the surface by switching between positive and negative DEP. Both regimes are readily achievable by operating at an appropriate

frequency of the AC field (Figure 4.4). Since the CM factor is a property of the probe and the medium only, we used the simplest electrode setup of two parallel plates to determine the crossover frequency. Using flat electrodes (Geometry A), dispersed probes were allowed to settle onto the surface of the bottom electrode via gravity and then (i) either a stepped potential (0 to 10V) was applied to the cell at a fixed frequency or (ii) the potential was held constant ($V_{pp}=10$ V) while modulating the frequency from 1 MHz to 1 kHz. Using TIRF detection, with a 70° angle of incidence, we captured movies of the probes present near sample surface (probes lifted from the surface by the DEP force into bulk solution do not fluoresce due to TIR illumination conditions).

Without an applied voltage, the probe population remained suspended some distance (up to 200 nm) above the surface trapped in a potential well formed by the repulsive double layer forces and attraction due to gravity. In this state, the thermally activated movement of the probes in the soft potential well resulted in significant fluctuations in intensity (comparable to their mean intensity). When the high frequency (>100 kHz) field was applied, the probe fluorescence became more intense (Figure 4.11 - right inset) and fluctuations in intensity were reduced, indicating that the DEP force drove the probes toward the surface. Conversely, when the field was applied at a low frequency (<10 kHz), the intensity of the fluorescence dropped to zero, indicating the probes were driven off the surface completely (Figure 4.11- left inset). Thus, positive DEP moves the polymer beads away from the flat electrode, whereas negative DEP attracts them to the surface.

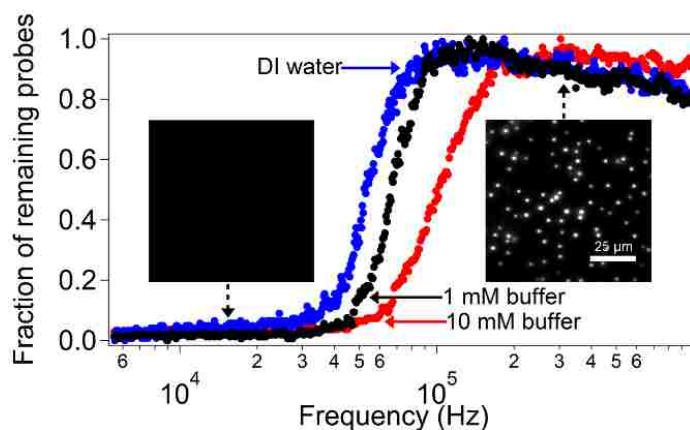


Figure 4.11 The number of polystyrene microspheres remaining on the surface of the electrode as the frequency of the applied AC field is changed from 1 MHz to 1 kHz in DI water or phosphate buffer. The number of probes is normalized to the maximum detected during a given sweep. In the negative DEP regime (high frequency), the number of probes slowly increases in the course of the experiment as more probes approach the surface from the bulk of the solution and accumulate at the surface due to attractive DEP forces. (left inset) TIRF image of a sample of probes when 10 V potential is applied at 200 kHz. The probes overcome the electrical double layer repulsion and land on the surface when the field is turned on. The intensity is high, indicating a close proximity to the surface. (right inset) Image of the same sample at a frequency of 10 kHz (10 V potential). Probes are no longer visible using TIRF microscopy.

In order to acquire the full frequency response of the probes in our system, we continuously monitored the number of probes in the vicinity of the surface (using TIRF) over the course of a frequency sweep at three different ionic strengths. The results shown in Figure 4.11 represent the changes of the CM factor with frequency of the AC field in

our system. The crossover between positive and negative DEP occurs at between 50 and 100 kHz and depends on the bead's surface (electrical double layer) conductivity, which changes with the ionic strength of the buffer. The method we describe here was highly reproducible (2-3% error for crossover frequency obtained in repeated experiments), independent of the rate of frequency sweep (between 1 and 4 decades per minute). Unlike the use of quadrupole electrodes⁸⁷, optical trapping⁸⁸ or patterned electrodes⁸⁹, our method is very straightforward to implement under different solution conditions for beads of various compositions and properties. Any proposed design of DEP tweezers can be quickly evaluated for the frequency dependence of the directionality of the force by carrying out a frequency sweep experiment with probes having inert chemistry (to ensure that they contact the surface of the electrode in a fully reversible manner). For example, we determined experimentally that microwells having a depth greater than the bead diameter (Geometry C) result in repulsion from the surface under positive DEP conditions (low frequency), whereas microwells with depths smaller than bead diameter (Geometry B) display attractive forces under the same conditions.

4.6.4 Voltage dependence of the DEP force on probes in microwells

We calculated the changes in the DEP force generated on a flat electrode and in a 4 μm height micro-well (Geometry C) when voltage between two electrodes was varied. The DEP force exerted on the probe follows a power law and the fitted value for an exponent is exactly 2 (as in the flat electrodes case for Geometry A).

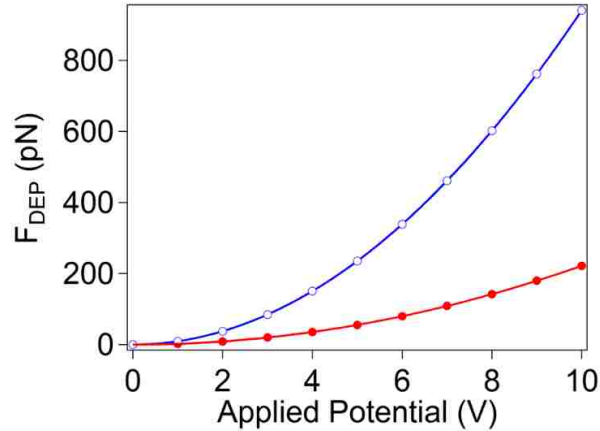


Figure 4.12 Simulation results of DEP force acting on a probe which is 50 nm away from the surface as a function of potential applied between two parallel electrodes separated by 24.5 μm for Geometry A (●) and C (○). For Geometry A, the line is a power law fit $F_{\text{DEP}}=2.22V^{2.00}$ (where F is in piconewtons, V is volts, standard deviation for both coefficients is $< 0.003\%$). For Geometry C, the line is a power law fit $F_{\text{DEP}}=9.41V^{2.00}$ (where F is in piconewtons, V is volts, standard deviation for both coefficients is $< 0.003\%$).

4.6.5 Changes in the DEP force magnitude with position of the probe

With single molecule force spectroscopy, one could study specific binding events (i.e. breaking of intermolecular contacts) as well as conformational changes and stretching of biopolymers (DNA and proteins) that could require a force probe to move by as much as 100-1000 nm, depending on the contour length of the biomolecule. Since field inhomogeneity is produced by microscopic features, changes in the DEP force experienced by probes moving near the surface of the electrode constitute an important characteristic in the design of the DEP tweezers.

4.6.6 Normal forces.

When a dielectric probe is placed between the two planar electrodes, the probe itself induces inhomogeneity in the electric field. Numerical calculations show a difference in the density of electric field lines above and below the probe in contact with the electrode (Figure 4.13a). The overall electric field is higher at the top half of the probe than at the bottom, so that the probe will move away from the electrode under conditions of the positive DEP, as indeed observed in our experiments (Figure 4.11). When the probe is displaced away from the surface, the asymmetry is gradually lost as the electric field intensity above and below the probe becomes balanced (Figure 4.13b), resulting in no net DEP force as expected for a dielectric probe suspended in a uniform electric field. The DEP force drops down to one half of its maximum value within $1 \mu\text{m}$ from the surface.

Once the probes are placed inside the microwells, the contrast in the intensity of the electric field around the probes markedly increases (Figure 4.13c-f) leading to forces higher than for a probe near a non-structured interface. For shallow wells (Geometry B), the high field is concentrated near the edges of the well. As a result, at any distance from the surface, the parts of the probe facing the sample experience a higher field than the parts facing the solution. This situation is opposite to what we found for flat electrodes (Geometry A). The DEP cell with shallow microwells (Geometry B) will produce a repulsive force at negative DEP (high frequency). Indeed, a voltage step from 0 to 1 V at 1 MHz results in the removal of the $3 \mu\text{m}$ probes from $1 \mu\text{m}$ deep wells in our experiments.

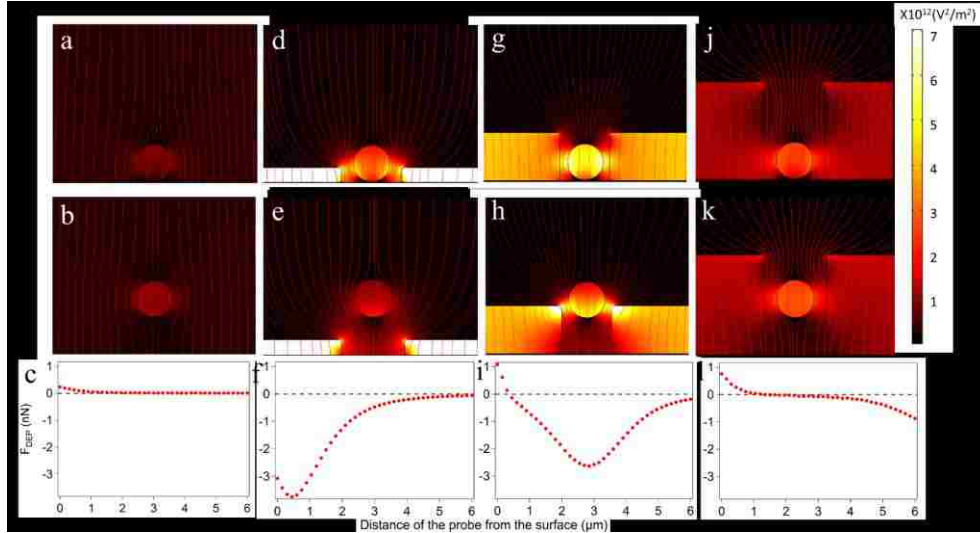


Figure 4.13 Electric field distributions in Geometry A (a-c), Geometry B (d-f), and Geometry C (g-l) for a 3 μm diameter probe at 50 nm (a, d, g, and j) and 3 μm (b, e, h, and k) above the surface of the electrode. When close to the surface, the probe is pulled up ($F_{DEP} > 0$) by the positive DEP force in (a), (g), and (j), and by the negative DEP in (d). The red streamlines represent the electric field. The surface plots are E^2 and all six graphs share the same scale. (c), (f), (i), and (l) The DEP forces versus distance from the surface when the 3 μm probe is moving away from the electrode.

When the depth of a microwell exceeds the size of the probe (Geometry C), the overall force profile represents a superposition of two opposing effects (i) a decrease of the electric field between the probe and electrode surface and (ii) an increase of the field around the edges of the well. For positive DEP (low frequency), the resulting force is repulsive and moves the bead away from the surface at small bead-electrode separations ($< 0.5 \mu\text{m}$ for a 4 μm deep well), whereas the force is attractive at large separations. For such a geometry, the probes can be trapped inside the well at some stable vertical position elevated above the surface, representing potential energy minimum for positive DEP (Figure 4.13i). Experiments with this design produced a stable trapping position for 3 μm diameter microspheres inside the microwells as demonstrated with far-field epi-

fluorescence. (Figure 4.14). The probes inside the well moved out of the focus, but stayed inside the wells, when the frequency was changed from 100 kHz to 1 kHz. In contrast, the intensity profiles of the beads on top of the SU8 layer show perfect overlap at 100 kHz and 1 kHz as expected for stationary probes, since now realignment was done during frequency shift.

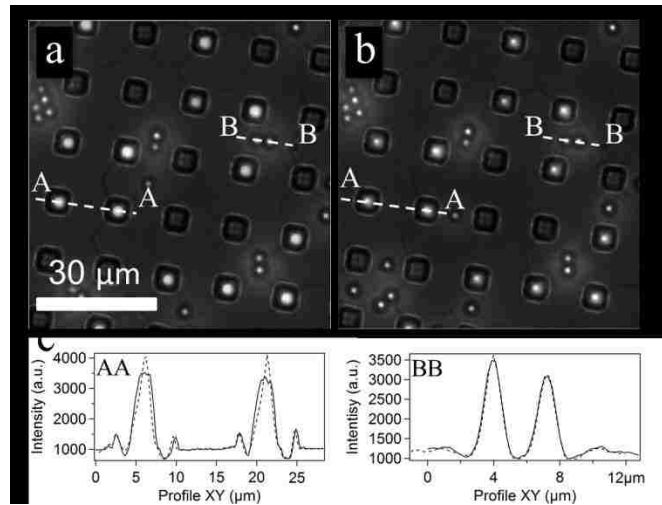


Figure 4.14 Epi-fluorescence images of the probes assembled in wells with Geometry C. (a) The probes are pushed toward the surface by a negative DEP force at high frequency (100 kHz) and (b) levitated above the surface by a positive DEP force at low frequency (1 kHz) ($V_{pp}=10$ V). The probes go slightly out of focus as indicated by their intensity profiles (c) when the frequency is switched from high (a) to low (b). Small bright spots are beads settled on top of the SU-8 surface between wells. Their positions do not change (c). The solid lines in (c) represent the profiles for 100 kHz AC field, while the dashed lines correspond to 1 KHz.

The competition between the two effects results in a quicker decay of the force with distance than for planar electrodes. The DEP force drops down to one half of its maximum value within 200-400 nm from the surface for 4-8 μm deep wells. On the other hand, the maximum force experienced by the probe in contact with the surface more than

doubles compared to the flat electrode (Geometry A) due to the concentration of the field inside the microwell containing the buffer solution having a higher polarizability than the adjacent photoresist.

The change of the force with increase of the probe separation from the electrode is a potential drawback of the DEP tweezers, since, in addition to calibration with respect to applied voltage and probe size for a given microwell design, the forces need to be measured or calibrated at every position of the probe. This requirement, however, is not substantially different from the need to measure forces at every experimental point in the force-distance curves obtained using common force spectroscopy methods such as AFM or optical tweezers. In principle, one can calibrate forces in DEP tweezers using thermal fluctuations in the probe position with either x-y or z tracking as is done for magnetic or optical tweezers. Since according in our simulations, the DEP force appears linear with respect to bead-surface separation at displacements below several hundred nanometers, one can also derive the DEP forces by calibrating this linear correlation; thus, only applied voltage and probe-surface distance will be required for the calculation of the DEP force experienced by the probe.

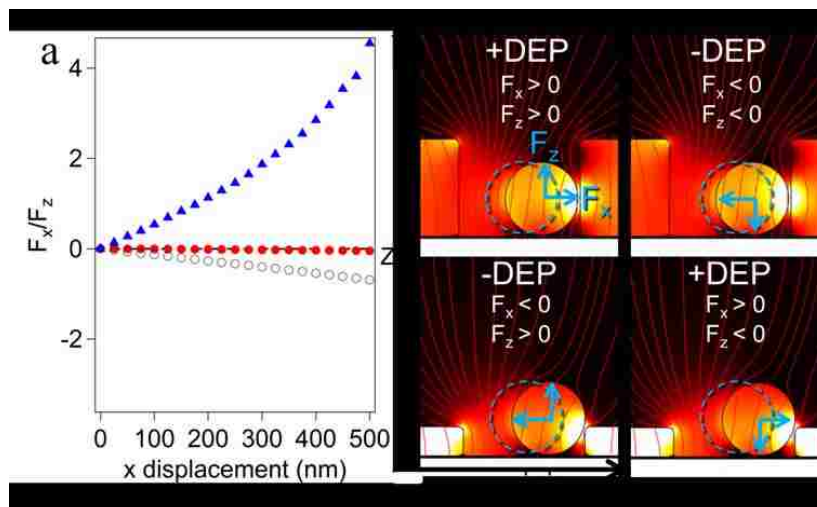


Figure 4.15 (a) The ratio of lateral forces to normal forces as functions of lateral displacement of the probes from the well axis for microwell DEP cell with Geometry B (Figure 2b, ▲), Geometry C (Figure 2c, ○), and Geometry D (Figure 2d, ●). (b) Blue dashed outlines show the centered position of the probes and the blue arrows show the direction of the normal and lateral forces acting on the probe in each situation (positive or negative DEP). These forces were calculated using a 2D well to reduce calculation time.

4.6.7 Lateral forces.

One can expect an imbalance of the electric field distribution, if the bead is not centered laterally in the microwell for Geometries B-D. A smaller gap between the probe and the wall results in a higher field intensity. This uneven electric field produces a lateral force that pulls the probes towards the wall during positive DEP and repels them from the wall under negative DEP conditions (Figure 4.15). Force spectroscopy operates by pulling the bead away from the surface, thereby stretching the attached molecule. In deep wells (Geometries C & D), a stretching force is applied using positive DEP, while shallow wells (Geometry B) use negative DEP.

Inspecting the relative magnitude of normal and lateral forces (Figure 4.13a), we observe that for deep wells it is crucial to have the probes properly centered, whereas some misalignment can be tolerated for shallow wells. Nevertheless, use of the deep wells may be preferred to shallow wells, because the required alignment can be achieved in the course of the attachment step by application of the negative DEP to trap the bead in the microwell (negative DEP traps and centers the probe in this case,). The probe will be axially centered by lateral forces at negative DEP (see Figure 4.15b) and its position fixed by the molecule attached between the electrode and the probe. Alternatively, one can make the top surface of the pattern conductive as well (by the second metal coating step) as in the DEP cell with Geometry D (Figure 4.5d). This cell produces no noticeable lateral force (Figure 8a) and centering of the bead inside the well becomes unimportant.

4.6.8 Measurements of molecular extension

The z-position of a microsphere near surface could be found using analysis of images from reflectance interference microscopy or TIRF microscopy. Both methods are compatible with flat electrodes, however, for structured electrodes, TIRF microscopy is preferred because only total intensity of the probe fluorescence or scattering intensity is needed to map the vertical position of the probe. We used through-objective laser TIRF in our experiments with DEP tweezers. To achieve TIR conditions at the bottom of the microwells, the incident laser beam must be prevented from entering the SU-8 resist layer, since otherwise propagating light conditions will be achieved effectively throughout the whole sample. A thick metal layer between the glass substrate and resist layer in the DEP cell design shown in Figure 4.5d (Geometry D) serves this purpose.

4.6.9 Electric field distribution inside a round well in Geometry D.

We simulated electric field distribution from the incident laser beam inside microwells using numerical code we developed for numerical analysis of the bead fluorescence excited by the evanescent wave. The presence of a dielectric with high dielectric permittivity in contact with glass breaks the condition for the total internal reflection of the waves incident from the glass coverslip. Although the TIR condition still holds at the glass-water interface, the propagating waves that originate at the glass-dielectric boundary can make their way inside the well and overwhelm the evanescent waves produced due to the total internal reflection. A thin layer of metal (~100 nm of gold) placed between glass and photoresists pattern is sufficient to block the propagation of waves into SU-8, preventing them from entering the well. The evanescent wave is then confined to a thin layer of water in the vicinity of the glass and its intensity decays towards the sidewalls. Due to the reflection from the walls of the well, an interference pattern develops inside the well, although its effect is likely to be minor due to more than an order of magnitude drop in intensity in the region where the variation in intensity becomes pronounced.

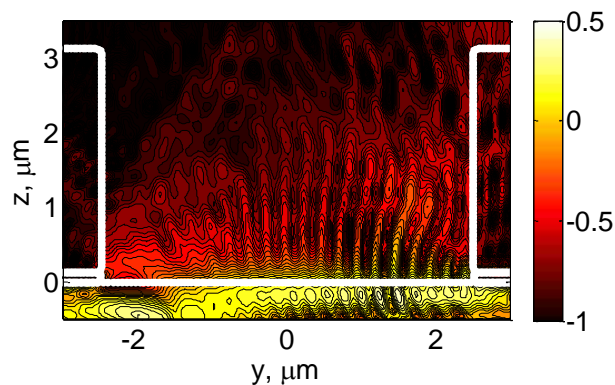


Figure 4.16 Electric field intensity distribution (\log_{10} scale) inside a well.

4.6.10 *Stretching of single stranded DNA molecules using DEP tweezers*

To demonstrate the ability of the proposed DEP tweezers to conduct single molecule force spectroscopy, we used a model system of ssDNA. We tethered the DEP probe to the surface via a 142 base long DNA oligomer using the reaction scheme depicted in Figure 4.17. The synthetic sequence contained two different terminal functional groups (thiol and amine) to facilitate attachment chemistry to gold electrode and poly(methyl methacrylate) microspheres bearing surface carboxyl groups. After the beads were flushed into the fluid cell and tethered to ssDNA molecules attached to the bottom of the wells, about 80% of the wells were occupied with the force probes (Figure 4.9a).

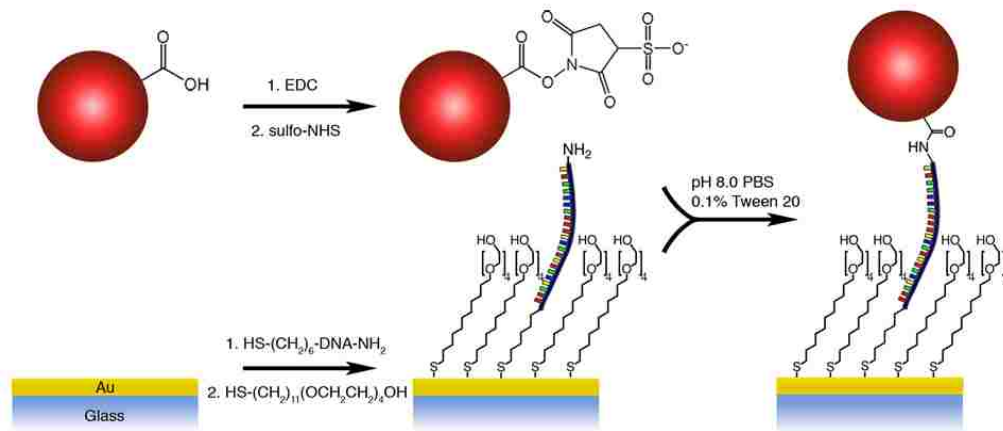


Figure 4.17 Reaction scheme of the probe and ssDNA attachment to gold electrode.

After attachment of probes, we applied a 1 kHz AC field to electrodes in the DEP fluid cell (Geometry D, Figure 4.5) and modulated the peak-to-peak voltage between 0 V and 10 V to stretch the DNA. When the AC field was applied, about 25% of the captured probes left the surface, indicating that these probes were not covalently bound to the ssDNA. The remaining probes showed intensity oscillations when we modulated the amplitude of AC voltage. At low forces (low voltage amplitude), the DNA is compact and probes are close to the surface of the electrode (i.e. the interface for TIR). As the voltage amplitude is ramped up, the probes move away from the surface, extending the DNA molecules. As expected for TIRF illumination, the fluorescence of the beads is brighter at low voltage than at high voltage (compare images in Figure 4.18b). The fluorescence intensities of the beads that move away from the surface at high voltage amplitude decay about 50% on average. According to the force-extension curve of ssDNA molecule, the estimated DEP force exerted on a probe is between 15 and 25 piconewtons.

The TIRF-illumination images of the probes in Figure 4.18 show a wide distribution of intensities. This variation can be attributed to a number of factors: (i) non-uniform particle size, (ii) differences in the lateral positions of probes in the wells, and (iii) a non-uniform (Gaussian) illuminating intensity distribution in the field of view. We have measured a moderate polydispersity of probes sizes (up to a factor of two difference in diameters) and, since the fluorescence intensity is proportional to the volume, this polydispersity can yield up to an order of magnitude difference in brightness. The probe position and the light distribution of the probe inside the well are related. Simulations show an uneven lateral distribution of light inside the wells, which decreases in intensity as the probes move closer to the edges. Finally, it may be possible that the thick gold layer on the bottom of the well is not fully etched for every well, thus blocking an unknown percentage of the illumination and emission of the probes.

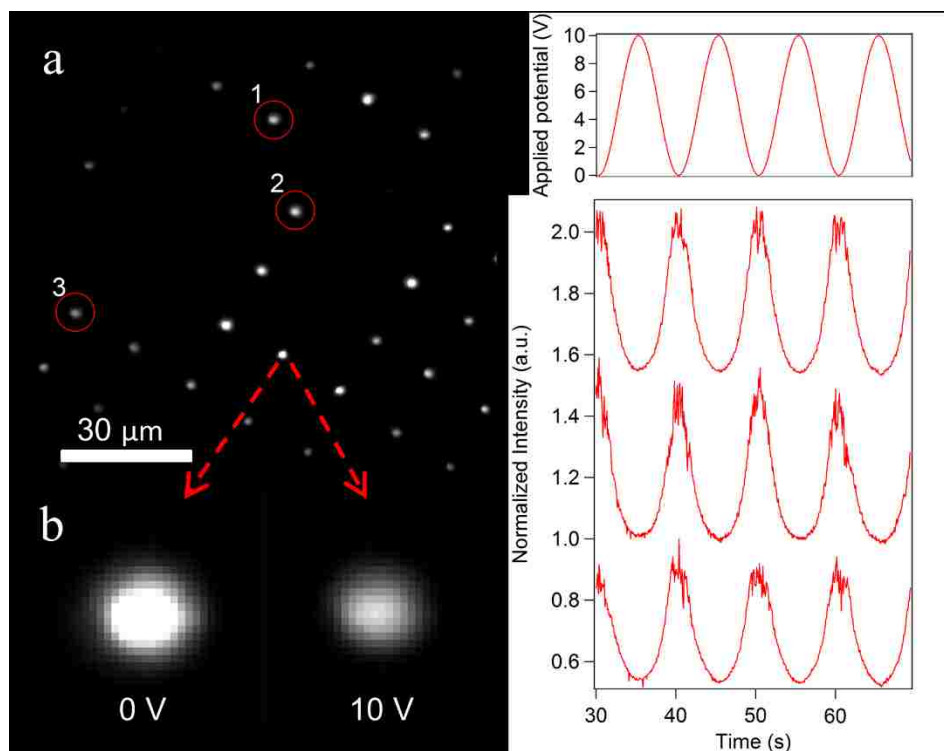


Figure 4.18 (a) TIRF image extracted from a movie of the beads bound to ssDNA molecules attached at low density at the bottom of the wells. The image was taken at 0V (i.e. when the probes were closest to the surface). (b) When the AC voltage amplitude changes from 0 V to 10 V, the brightness of the probe drops approximately 50%, consistent with the probe being pulled away from the surface and the DNA molecule being stretched. (c) Applied potential and raw fluorescence intensity data (normalized to a maximum intensity observed in a given trace) versus time for three beads circled in part (a). Intensity traces are shifted with respect to each other for clarity.

We are able to record movies of active probes (those that exhibited a change in intensity upon application of force) and record multiple force-extension curves for an array of the DNA molecules. As can be seen from the time traces of the total fluorescence intensity shown in Figure 4.18c, the force-extension curves for individual molecules are very reproducible and one can acquire high-quality data from multiple molecules in parallel. In this particular frame, 27 force probes populated 50 microwells and most of

them showed the behaviour expected for single molecule stretching (only a few produced changes in intensity consistent with multi-tether attachment). The current DEP tweezers setup can already be used in qualitative analysis, for example, in the case of the ssDNA used here, to detect binding of the DNA-binding proteins or hybridization with a complementary oligomer. Quantitative force spectroscopy will require proper calibration of forces and bead-surface distances as well as the light intensity field in the microwells, all of which are the focus of our on-going work with this system.

4.7 Conclusions

We proposed a new single molecule force spectroscopy method based on dielectrophoresis—DEP tweezers. Numerical simulations suggest that forces on the order of 1 nN can be readily achieved with a 10 V peak-to-peak AC voltage applied to a DEP cell. The direction of the force can be switched by selecting the frequency regime appropriate for either positive or negative DEP. The parallel-plate electrodes DEP cell design can serve as a simple device to map the crossover frequency between the two DEP regimes for different probes and solution conditions without setting up the quadruple electrodes or integrating the DEP device with the optical tweezers.

There are several disadvantages to this method of manipulation of the force probes: (i) DEP forces acting on a colloidal probe decay quickly with its distance from the electrode (within 200-500 nm); (ii) the maximum force achieved in the DEP tweezers drops rapidly (inversely quadratic) with an increase in the inter-electrode gap; and (iii) forces need to be measured or calibrated independently for each position of the probe. Some of these

difficulties can be alleviated by using microstructured electrodes; for example, microwells can increase the maximum force on the beads and greatly reduce the dependence of the DEP force on the inter-electrode spacing. Microwell arrays can have added benefits for DEP tweezers by increasing the density of the probes on the surface, simplifying bead indexing, and improving stability of the probe-molecule assembly by reducing shear forces during exchange of the solution inside the fluid cell. The final assembled instrument was applied to stretching of the ssDNA molecules and demonstrated reproducible operation in stretching single DNA molecules.

We have examined a variety of chip geometries for highly parallel force spectroscopy, each with its own set of advantages and limitations. We feel that, with the selection of geometries described in this paper, most applications involving some form of force application should be amenable to DEP tweezers. For applications where the applied force must be known quantitatively (such as in protein unfolding or DNA stretching) a middle ground must be reached between the magnitude of the forces and complexity of the cell design and data analysis. One has to compromise between small variations in the magnitude of the forces (less than an order of magnitude) due to positioning and size, and the need for an individual calibration of the forces on each probe in order to measure the forces in an arbitrary system. Refinement of the uniformity of the experimental implementation of the DEP tweezers (e.g. use of symmetrical round wells and monodisperse probes) can also alleviate the issues of device calibration. As opposed to the microwell geometry, the planar electrode produces more uniform forces across the entire working area making it easier to directly compare the results of adjacent

probes at the expense of reduced force magnitude and the need for slower fluid exchange. If both conditions are required (high forces and a calibrated force magnitude) one can use the microwell geometry with a force calibration based on the Brownian diffusion of the probes under applied force.

4.8 Future directions

4.8.1 Reducing the size of force probes.

Optical and magnetic tweezers rely on μm -sized colloidal probes because the force scales with the volume of the probe (which in turn scales with radius as R^3). Using μm -sized probes often leads to the difficulty of binding single molecule to the single force probe due to the large size difference. Alternatively, DEP tweezers provide an opportunity to scale down the size of the force probe significantly in order to enable simple attachment chemistry and to assemble probe-single-molecule arrays. According to the first order approximation of the DEP force, one need to increase the electric field magnitude if one want to preserve the same force magnitude on nm-sized force probes. Reducing the dimensions of the device essentially increases the electric field magnitude since the electric field is proportional to the inverse of the distance between electrodes.

We will design several geometries for nanoparticle DEP tweezers experiments and investigate them with numerical simulations. To reduce the fabrication cost and non-uniformity, flat electrodes design is always attractive. In order to assemble the DEP cell

at such a small scale, we will introduce a small fraction of large size particles (Fig. 5A) to serve as spacers.

In preliminary calculations, we estimated how electrodes separation affects the normal DEP force. When the distance between two electrodes increases from 100 nm to 1 μm , the DEP force drops from 900 pN to tens of pico-Newtons (Figure 4.19A). Thus, in order to maintain a high magnitude of the DEP force, we need to assemble a device with small electrode separation. There are several advantages of this design: (i) there is nearly no fabrication effort required to assemble this device having nanoscopic inter-electrode spacing; (ii) the DEP force can be readily reach hundreds of pico-Newtons by reducing the distance between two electrodes. The potential drawback of such a design is that the force is only maintained to within a short distance from the surface. With the distance between two electrodes fixed at 200 nm, the calculated DEP force (Figure 4.19B) decays to zero when the force probe is 40 nm above the surface. Based on our simulation results, the range of molecular extensions resulting in DEP force with relatively high magnitude is limited to distances comparable to the size of the force probe.

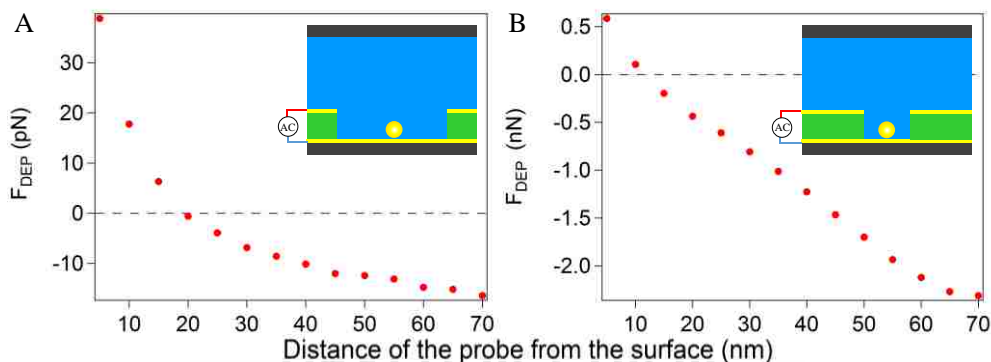


Figure 4.19 The DEP forces versus distance from the surface when the 40 nm probe is moving away from the electrode.

We also modelled two other designs that involve micro-/nano-wells, where the electric field gradient around the force probe is dramatically increased. Microwells are straightforward to fabricate with conventional photolithography. When we place a 40 nm diameter nano-sized force probe inside a 1 μm width round well, pico-Newton level forces can be exerted on the force probe. When the probe is moving away from the surface, the DEP force decay to zero and change the direction. The stable trapping position for such geometry is around the radius of the particle. The magnitude of the DEP force is smaller than the two parallel electrodes design. Lastly, we look at the nanowell structure with a comparable width to the probe diameter. We placed a 40 nm diameter nanoparticle into a 100 nm width round well. In this case, the DEP force changes direction when the probe is 10 nm away from the surface. When the probe is moving away from the surface, the magnitude of DEP force markedly increases to nano-Newtons range. In the last two designs, the assembly of the fluidic-cell is easier comparing to the two parallel electrodes design since there is no need to create such a narrow channel. The last design offers nano-Newtons range forces, which is phenomenal for nano-sized force probes. The simulation indicates that by reducing the width of the nanowell, the location of the zero force is near the surface. By optimizing the height and the width of the nanowell, we can achieve high DEP force and adjust it to one type (either positive or negative). However, this design requires substantial fabrication efforts. Tanni's group demonstrated that 30 nm to 150 nm nanoholes can be fabricated with an inexpensive UV nanoimprint lithography method. Alternatively, Philseok *et al.* had shown that a typical

micro-size fabrication followed by electrodeposition of the polymer will produce ~100 nm nanowells.

These designs could enable us to use gold nanoparticle as our force probes. The attachment of the gold nanoparticles is similar to attachment to colloidal probes, with two important simplifications: (i) the gold nanoparticle is easily modified with thiolated DNA, requiring no activation chemistry and (ii) the size of the gold nanoparticle is commensurate with the hydrodynamic radius of the DNA strand itself (~10 nm). The similarity in size between the gold nanoparticle and the target molecule significantly reduces the possibility of making multiple tethers between the probe and the surface. Furthermore, the small size of the nanoparticles reduces nonspecific binding of probes to the substrate. In spite of the gold nanoparticles' small dimensions, we found that they scatter very brightly (several orders of magnitude brighter than the background) under TIR illumination (Figure 4.20). We expect scattering of these gold nanoparticle tethers to provide us with highly accurate nanometric measurements of extensions for single molecules in a way previously unprecedented in the SMFS community as discussed in the next section.

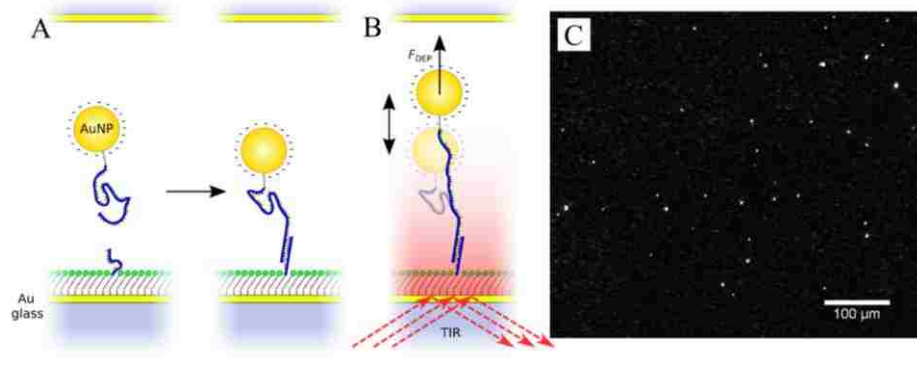


Figure 4.20 SMFS using Au nanoparticles in a DEP fluid cell. (A) Thiol terminated cDNA primers are first introduced on the surface using competitive binding chemistry. Gold nanoparticles, functionalized with the target DNA strand, are then added to a surface containing cDNA. (B) After hybridization, a DEP force can be used to stretch the single DNA strand, while measuring its extension using TIR-scattering from the Au nanoparticle. (C) Experimental image of a dilute solution of 17 nm diameter gold nanoparticles in a fluid cell (20x magnification, TIR-illumination).

4.8.2 Low magnification objective enables large sample area observation

We envision a move away from the objective-style TIRF detection scheme as the next logical step in further parallelizing our platform. Since objective-style TIRF limits the area of analysis to the small field-of-view of a high powered (60 \times -100 \times), high numerical aperture (NA), objective we have begun testing a setup using a planar wave guide excitation combined with detection using a low magnification (10 \times), low NA, objective (Figure 4.21). We were able to drastically increase the number of probes analyzed at any one time by using a forward scattering setup constructed using evanescently-guided light passed through the edge of a glass coverslip patterned with our array (Figure 4.21). For observation of probes, the low magnification objective (10 \times) was placed above the sample area. As a consequence of drastically increasing the area of analysis (from $4 \cdot 10^4 \mu\text{m}^2$ to $2 \cdot 10^6 \mu\text{m}^2$), it becomes far too difficult to maintain a laterally uniform

magnetic field gradient, making the large electrodes fabricated for DEP the practical choice for the application of force. Lastly, using this technique we are no longer restricted to fluorescent detection of probes, eliminating the need for fluorescent dyes, which have the propensity to photobleach. Since we are now using a low magnification objective we can use the light scattered by the microspheres as a measure of distance. Like fluorescence, the intensity of light forward scattered is dependent of the probes position in the evanescent field making it a suitable choice for detection. Therefore, we can integrate the highly parallel force spectroscopy method with a large sample area characterization method to achieve a highly parallel DNA sequencing platform.

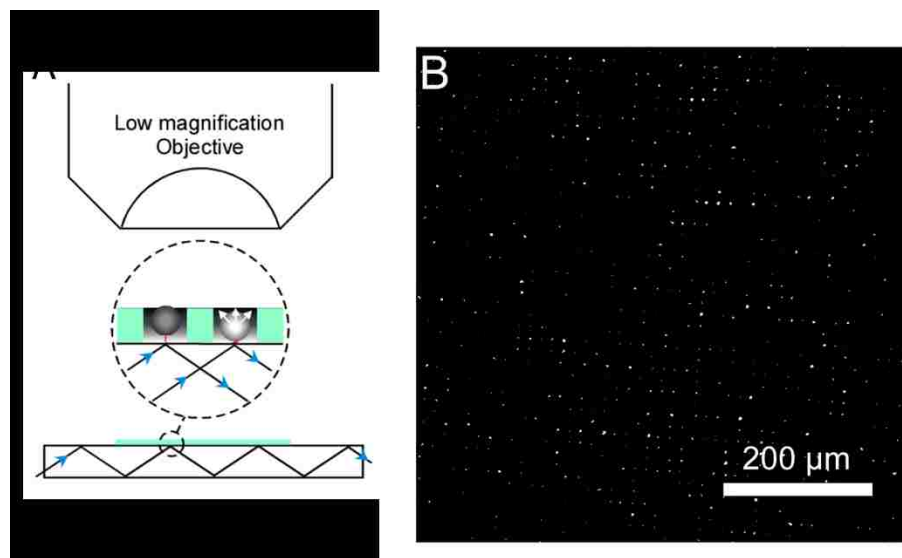


Figure 4.21 (A) The incident light undergoes total internal reflection at glass-water interface in a planar-waveguide implementation of a force spectroscopy array. Forward scattering of the evanescent field by dielectric microspheres maps their distance from the surface of the waveguide. (B) We used 10× objective to capture the intensity of light scattered by beads.

Chapter 5 DEP force calibration and stretching of single DNA molecule

Part of the work described in this chapter has been published in P. Cheng, P. M. Oliver, M. J. Barrett and D. Vezenov, Progress toward the application of molecular force spectroscopy to DNA sequencing, ELECTROPHORESIS, 2012, 33, 3497-3505.

5.1 Introduction

Detection of the physical differences in conformations of single and double stranded DNA is at the heart of the technology we are developing for genome sequencing in previous chapters. We have described dielectrophoretic (DEP) tweezers combined with total internal reflection fluorescent microscopy (TIRFM) as a highly parallel platform aimed at achieving single molecule sensitivity in bioanalysis.^{24, 90} DEP tweezers are of particular interest due to their promise of high speed analysis, low cost, and simplicity of implementation. In DEP tweezers, one end of the DNA molecule is bound to a dielectric bead and the other end is tethered to the surface of a solid support. A non-uniform electric field exerts force on the dielectric bead to manipulate the bead so that DNA molecule can be stretched.

The extension of DNA molecule is measured by recording the intensity of the bead fluorescence using video microscopy. We estimated theoretical values of the DEP force for different designs of the DEP tweezers using numerical simulations described in the previous chapter. In order to quantify the relationship between extension and the force applied to the DNA molecule, we need to carefully calibrate the DEP force.

In this chapter, I describe three different methods we used to quantify DEP force. i) We calibrated DEP force by directly measuring the potential energy profile for

interaction between our spherical probes and wall under conditions of hindered diffusion.^{91, 92} ii) We also constructed combined DEP tweezers & magnetic tweezers in the same experimental platform and compared the DEP force with previous calibrated magnetic force.⁹⁰ iii) Lastly, we applied DEP tweezers to study the elasticity the model DNA molecule and used the equation of state for ssDNA to calibrate forces observed.^{25, 30}

5.2 Theory

5.2.1 Using TIRFM to measure the particle-wall separation distance

In order to determine the instantaneous distance, we measured the fluorescent intensity of the probe under evanescent wave illumination. The evanescent wave is generated by totally reflecting the laser beam at the glass-water interface when the incident angle is larger than the critical angle. Snell's law gives the relationship between the incident and transmitted angles θ_{inc} and θ_{trans} as:

$$n_{glass} \sin \theta_{inc} = n_{water} \sin \theta_{trans} \quad (5-1)$$

where n_{glass} and n_{water} are the refractive indices of the glass and water. Since n_{glass} is larger than n_{water} , transmitted angle is larger than incident angle. When the incident angle is larger than critical angle (i.e. when transmitted angle is 90°):

$$\theta_{critical} = \sin^{-1} \frac{n_{water}}{n_{glass}} \quad (5-2)$$

the incident laser beam is total internally reflected at the glass-water interface (Figure 5.1A). Under these conditions, the optical field exists in the form of evanescent wave, which propagates along the interface. The electric field intensity of evanescent wave decays exponentially with distance from the interface. When a fluorescent particles is

positioned within such an evanescent field, the intensity of its fluorescent image drops exponentially as it is moved away from the interface.

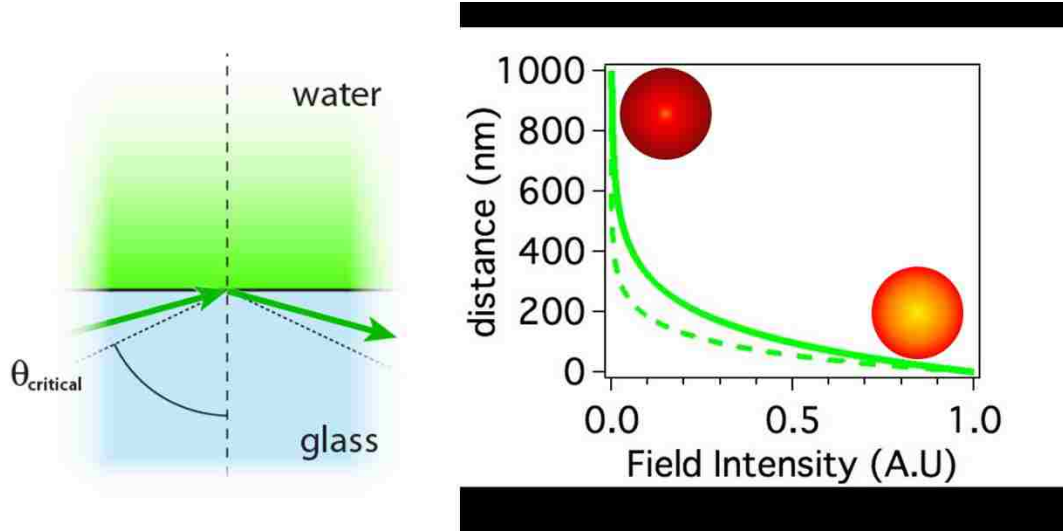


Figure 5.1 When transmitted angle is larger than critical angle, evanescent wave is generated. The intensity of electric field drops exponentially as a function of the distance from the interface.

In the TIRFM experiment, the fluorescent intensity of the probe in an evanescent field can be used to determine the instantaneous particle-wall separation, h , as shown in the following equation⁹³:

$$I(h) = I_0 \exp\left(-\frac{h}{d}\right) \quad (5-3)$$

where I is the fluorescent intensity, I_0 is the intensity at particle-wall contact, and d is the penetration depth of the evanescent wave, which is a function of the incident angle θ , wave length λ of the incident beam, and refractive indices of the two media n_1 and n_2 :

$$d = \frac{4\pi}{\lambda} \sqrt{(n_1 \sin \theta)^2 - n_2^2} \quad (5-4)$$

Typical d is about 150 nm in our experiments. Using exponential sensitivity of image brightness on the placement of probe in the near field, one can achieve high spatial resolution of the vertical position of the probe with respect to the glass-water interface. Therefore, changes of the probe position can be directly mapped onto changes in molecular extension.

5.2.2 Potential energy profile

The total potential energy profile of a single particle near the interface can be calculated by summing contributions due to all the forces acting on the particle:

$$U_{total} = U_{es} + U_G + U_{DEP} \quad (5-5)$$

where U_{es} is the interaction between overlapping electrostatic double layers on the particle and the wall, U_G is the buoyance force, and U_{DEP} is the potential energy of the particle due to DEP force. Van der Waals attraction is not shown in this equation since van der Waals force is negligible at long separations from surface typical of the tweezers setup.

For symmetrical electrolyte, the electrostatic potential, U_{es} is given as:

$$U_{es} = 4\pi\epsilon r \Psi_{particle} \Psi_{wall} \exp\left(-\frac{h}{\kappa}\right) \quad (5-6)$$

$$\kappa^{-1} = (2e^2 z^2 C N_A / \epsilon k_B T)^{1/2} \quad (5-7)$$

where ϵ is the dielectric constant of water, r is the radius of the particle, $\Psi_{particle}$ and Ψ_{wall} are the Stern potentials of the particle and the wall, respectively, κ is the Debye length, e is the elemental charge, z is the ion valence, C is the bulk electrolyte

concentration, N_A is the Avogadro's number, k_B is the Boltzmann's constant, T is the absolute temperature.

For spherical probes, the gravitational potential energy, U_G can be expressed as:

$$U_G = \frac{4}{3}\pi r^3(\rho_{particle} - \rho_{water})gh \quad (5-8)$$

where g is the acceleration due to gravity, and $\rho_{particle}$ and ρ_{water} are the densities of the particle and water, respectively.

By fitting the potential energy profile to known fundamental form, we can obtain the potential of DEP force that exerted on the particle and therefore calculate DEP force as an derivative of U_{DEP} .

5.2.3 Freely jointed chain model of macro-molecule

In this chapter, we show that a freely jointed chain model for ssDNA can be applied to raw DEP tweezers data to obtain several calibration parameters including DEP force exerted on the particle and evanescent field penetration depth.

Consider a freely jointed chain of N bonds of Kuhn segments stretched by a force f applied to its ends along z axis, as shown in Figure 5.2A.

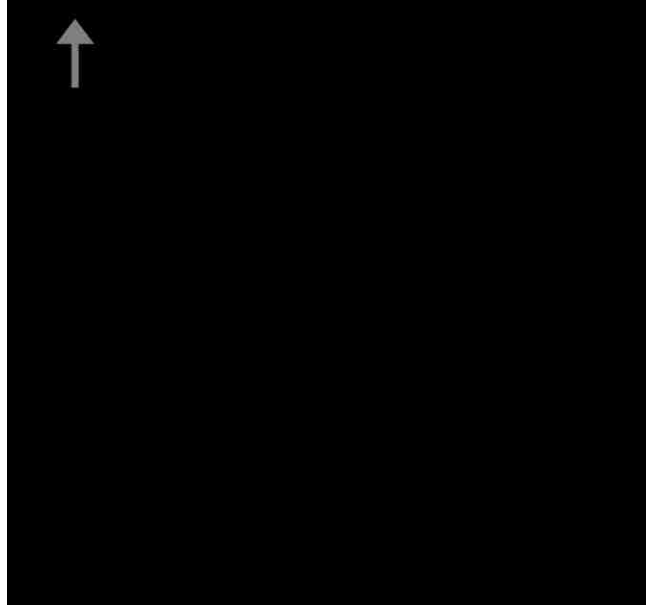


Figure 5.2 Many Kuhn segments freely jointed as a chain. Every segment has can be freely rotated.

We can calculate the partition function Q by summing up all the Boltzmann factors $\exp(-U/kT)$. In this case, energy U are spans all the different conformation of the ssDNA molecule.

$$Q = \sum \exp\left(-\frac{U}{k_B T}\right) = \sum \exp\left(\frac{FR_z}{k_B T}\right) \quad (5-9)$$

Different conformations of ssDNA molecule correspond to different sets of orientations of bond vector r . θ and φ are two polar angles of each bond vector in the spherical coordinate system. Thus, we can integrate all the possible orientations of all bond vectors of the chain to calculate the partition function:

$$Q = \int \exp\left(\frac{FR_z}{k_B T}\right) \prod_{i=1}^N \sin \theta_i d\theta_i d\varphi_i \quad (5-10)$$

$$R_z = \sum_{i=1}^N b \cos \theta_i \quad (5-11)$$

where the integral is multidimensional over all θ and φ

$$Q = \left[\frac{4\pi \sinh(Fb/k_B T)}{Fb/k_B T} \right]^N \quad (5-12)$$

We can then calculate the Helmholtz free energy and derive the relationship between force and extension of ideal ssDNA.

$$A = -k_B T \ln Q = -k_B T N \left[\ln \left(4\pi \sinh \left(\frac{Fb}{k_B T} \right) \right) - \ln \left(\frac{Fb}{k_B T} \right) l \right] \quad (5-13)$$

$$\langle R \rangle = -\frac{\partial G}{\partial F} = L_{ss} \left[\coth(f_{ss}) - \frac{1}{f_{ss}} \right] \quad (5-14)$$

where $f_{ss} = \frac{Fb}{k_B T}$. Smith, et al. shown that a Kuhn segment of ssDNA can be stretched as well. When ssDNA is under tension, the sugar pucker in ssDNA changed from C3' endo to C2' endo conformation²⁶ so that inter-phosphate distance changes from ~ 5.9 Å to ~ 7 Å, as we can see in Fig. 3. This change can take into account for segment size changes under applied force.

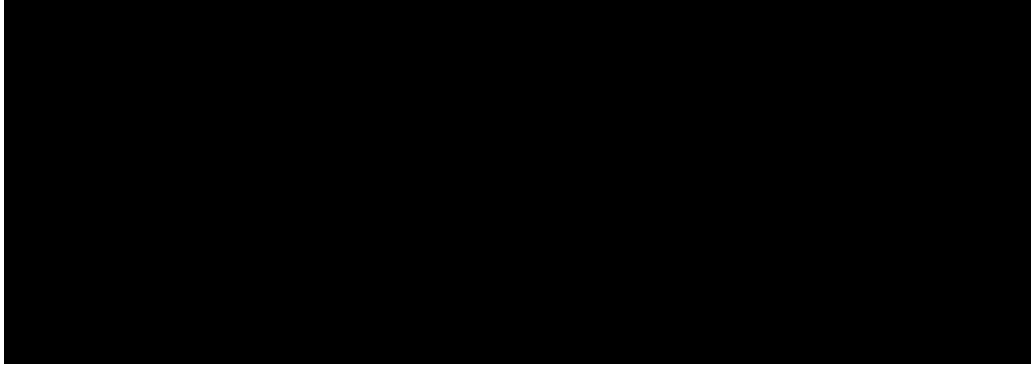


Figure 5.3 Two conformations of DNA backbone.

Finally, the modified FJC model is used to describe the elasticity of ssDNA:

$$\langle R \rangle = L_{ss} \left[\coth(f_{ss}) - \frac{1}{f_{ss}} \right] \left(1 + \frac{F}{K_{ss}} \right) \quad (5-15)$$

where K_{ss} is the dimensionless segment elasticity.

5.3 Methods

5.3.1 Evanescent illumination and detection

An objective-type TIRF system was assembled using an Olympus IX71 inverted optical microscope with a high numerical aperture TIRF lens (Olympus, 60x, NA = 1.45) and a 532 nm 12 mW laser (OZ-Optics, Ottawa, Ontario, Canada). The refractive indices for water ($n_{\text{water}} = 1.333$) and glass coverslip ($n_{\text{glass}} = 1.519$), gave a critical angle of $\theta_c = 61.1^\circ$. The laser beam was TM polarized, with a final power set at ~ 4 mW at the input (the microscope optics attenuated the input power by approximately 90 %). A motorized actuator (CMA-12CCCL, Newport) changed the incident laser beam angle to allow for control of the penetration depth of the evanescent field. The quantity dx was referenced to the lateral position of the marginal ray in our setup (i.e. the highest incident angle). Beads were imaged by an iXon DV888 (Andor Technologies, Belfast, Ireland) back-illuminated electron-multiplying charge-coupled device (EMCCD) camera (0.227 μm per pixel, >95% quantum efficiency at 532 nm) cooled to -85°C . Custom written Igor Pro code with an XOP allowing communication between the camera and computer (Bruyton, Seattle, WA, USA) enabled movies to be taken and streamed to disk at frame rates up to 30 Hz depending on the exposure time and size of the region of interest (ROI). An active response vibration isolation platform (StableTable, Herzan, Laguna Hills, CA, USA) stabilized the entire setup.

5.3.2 Direct measurement of potential profile

Fluorescent PMMA-MAA particles 4 μm in diameter were suspended in 0.1% solution of TWEEN 20 in DI water or phosphate buffer (pH 7.4) at 10~40 mM total ionic strength and flushed into the microfluidic cell integrated with DEP chip. For studying particle-wall interaction on a flat substrate, the particles settled down close to the surface by gravity. A constant frequency and voltage was applied to the two electrodes while a video was captured by a CCD camera.

5.3.3 Force spectroscopy

To conduct the force spectroscopy experiments, we fabricated a microwell array as described elsewhere. A glass substrate was coated with a thick gold layer, followed by a layer of 4 μm deep, 7 μm diameter wells, with the gold on their floors etched away and finally topped with a thin gold layer. DNA was added to the surface in a 1 μM solution with 10 mM phosphate buffer (pH 8) with 100 mM NaCl followed by a surface modification with MutEG (chosen as the best blocker from the probe binding assays) followed by the conjugation of the probes. The two step binding process was chosen to maximize the probe-DNA binding efficiency. The probes were reacted to the amine groups at the free end of the DNA. The whole chip was integrated into a fluid cell and an AC electric field was applied to conduct stretching of single DNA oligomers with the DEP tweezers.

5.3.4 Data Capture and Analysis

In a typical TIRF/DEP tweezers experiment we found “active” probes, or probes that display proper extension behavior, by linearly ramping the current between zero and maximum at a rate of 0.5 Hz while previewing the sample. A smaller capture area was created around those probes that were blinking or “active”. In a single field of view ($144\ \mu\text{m} \times 144\ \mu\text{m}$) we found on average 50 active probes. Exposure time and laser intensity were tuned to maximize the bead intensity without saturating the detector (typical settings were 0.02 to 0.10 s exposure time and $\sim 25\%$ of the maximum laser power or $\sim 4\ \text{mW}$). A sinusoidal voltage modulation was applied to the electrodes at a rate of 0.1-0.2 Hz during movie capture. Data analysis to generate intensity-voltage curves was performed using custom Igor code. Initial probe locations were found by thresholding and then (more accurately) from a fit to a 2-D Gaussian function. Intensities were then computed by first subtracting a plane-fit background (from a $2\ \mu\text{m}$ -wide ROI surrounding the region of integration of the probe image) and then numerically integrating in the x and y directions over a circular region with a diameter of $7\ \mu\text{m}$ around the center of the probe for each frame.

5.4 Results and Discussion

5.4.1 Force calibration from experimental potential energy profile

All potential energy profiles were generated using TIRFM experiments. The fluorescent intensity of the particles were monitored using video microscopy. We first

acquired a histogram of the intensity distribution over a long period of time. We can then obtain the probability of finding a particular particle-wall separation (fluorescent intensity) from the histogram, which will be:

$$p(h) = \frac{N(I)I}{\sum I_i N(I_i)} \quad (5-16)$$

We can also write the expected probability of sampling each height above the surface, which is related to the potential energy of each height, in the form of Boltzmann probability distribution:

$$p(h) = \frac{1}{Q} \exp \left[-\frac{U_{total}(h)}{k_B T} \right] \quad (5-17)$$

Assigning the most probable intensity (position) of the particle to the bottom of the potential well, then the potential energy profile can be calculated from

$$U(h) - U(h_m) = k_B T \ln \frac{N(I_m)I_m}{N(I)I} \quad (5-18)$$

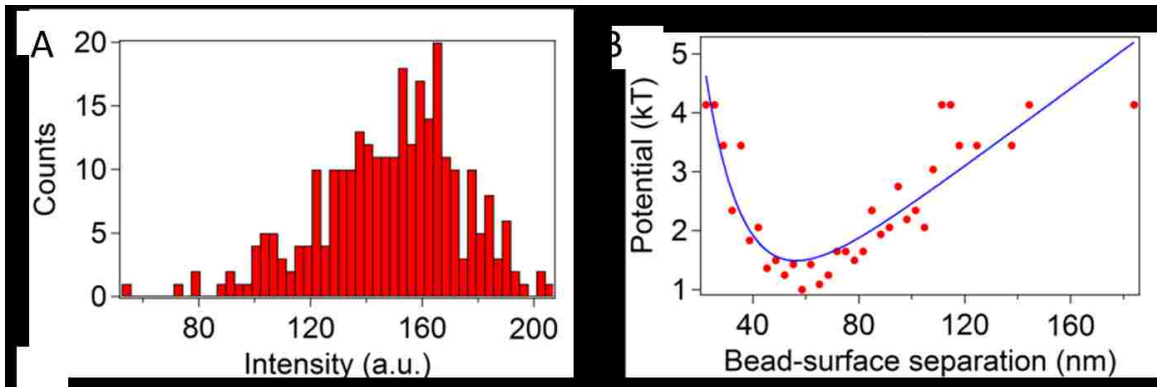


Figure 5.4 Histogram of fluorescent intensity (left) and potential energy profile (right).

The DEP force we calculated using this potential profile is 0.8 pN. Here we are assuming the highest intensity obtained from intensity histogram is I_0 . However, this assumption is not always true, especially when the high surface charge density from the

wall pushed the particle away from the surface. If one could measure I_0 independently, absolute separation can be achieved using fluorescent intensity data. Lacking the value of I_0 , we need to find an alternative way to derive the most probable position to gain a more precise calibration of DEP force.

5.4.2 Calculation of h_m

Instead of plotting the potential profile as a function of the absolute particle-wall separation, we can work with the potential energy against relative separation $\delta = h - h_m$

$$\delta = d \cdot \ln\left(\frac{I_m}{I}\right) \quad (5-19)$$

Next we can evaluate h_m by calculating the weight averaged diffusion coefficient. One method to analyze the apparent diffusion coefficient of Brownian particle is to compute the associated intensity autocorrelation function, which is given as:

$$R(\tau) = \langle I(t)I(t + \tau) \rangle = \lim_{T \rightarrow \infty} \left[\frac{1}{T} \int_{t_0}^{t_0+T} I(t)I(t + \tau) dt \right] \quad (5-20)$$

We can also integrate the autocorrelation function over the position h rather than overtime. In this case, the particle is initially located in position h_0 at time t_0 . After delay time τ , the particle moved to position h . The probability $p(h_0)$ of finding the particle at h_0 can be expressed as Boltzmann distribution:

$$p(h_0) = \frac{1}{Q} \exp[-U(h_0)/k_B T]$$

Then the probability of finding the particle at position h after time τ can be written as $p(h_0)W(h, h_0; \tau)dh_0dh$, while $W(h, h_0; \tau)$ is the conditional probability for initial position and time. The autocorrelation function can then be expressed instead as:

$$R(\tau) = \int_{-\infty}^{+\infty} dh_0 \int_{-\infty}^{+\infty} dh I(h) I(h_0) p(h_0) W(h, h_0; \tau) \quad (5-20)$$

In the limit of zero delay time, $W(h, h_0; 0)$ is equal to $\delta(h - h_0)$. The particle-wall separation is equal to the initial separation distance, which implies that:

$$R(0) = \int_{-\infty}^{\infty} I^2(h_0) p(h_0) dh_0 = \langle I^2 \rangle \quad (5-21)$$

By plugging Smoluchowski's equation:

$$\frac{\partial W}{\partial \tau} = \frac{\partial}{\partial h} \left(D \frac{\partial W}{\partial h} + m \frac{dU(h)}{dh} W \right)$$

into equation (5-20), we can then calculate the derivative of the autocorrelation function at small delay times τ as:

$$R'(0) = -\alpha^2 \int_{-\infty}^{\infty} D(h) I^2(h) p(h) dh \quad (5-22)$$

So that the initial slope of the autocorrelation function is proportional to the weight averaged diffusion coefficient:

$$D_{app} = -\alpha^{-2} \frac{R'(0)}{R(0)} = \frac{\int_{-\infty}^{\infty} D(h) I^2(h) p(h) dh}{\int_{-\infty}^{\infty} I^2(h_0) p(h_0) dh_0} \quad (5-23)$$

We can then re-calculate the autocorrelation function with relative separation δ as the variable and express “apparent diffusion coefficient” as a function of most probable position h_m :

$$g(h_m) = \frac{\int_{-\infty}^{\infty} D(\delta+h_m) I^2(\delta) p(\delta) d\delta}{\int_{-\infty}^{\infty} I^2(\delta) p(\delta) d\delta} = \frac{\int_{-\infty}^{\infty} D(\delta+h_m) e^{-2\alpha\delta} e^{\left(-\frac{U(\delta)}{k_B T}\right)} d\delta}{\int_{-\infty}^{\infty} e^{-2\alpha\delta} e^{\left(-\frac{U(\delta)}{k_B T}\right)} d\delta} \quad (5-24)$$

Figure 5.5 shows the function $g(h_m)$ computed from equation. The cross-section of $g(h_m) = D_{app}$ gives the absolute separation between the most probable position and the

wall. In the case of 4V applied voltage, this separation is found to be 79 nm, which is different from fitted bottom of the potential well (55 nm).

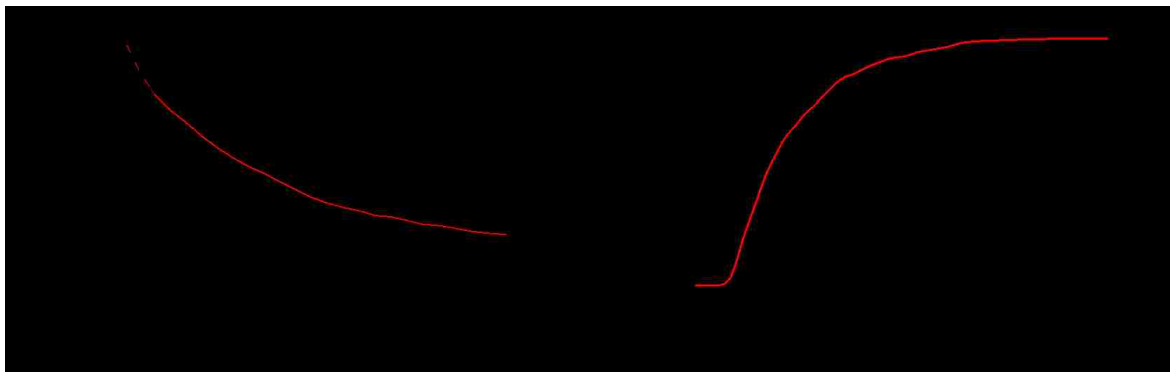


Figure 5.5 Autocorrelation function of fluorescent intensity (left) and apparent diffusion coefficient as a function of most probable position (right).

Finally, we can plot the potential energy profile as a function of the absolute particle-wall separation.

By repeating this analysis at different AC voltages, DEP cell designs and bead sizes, absolute values for DEP force will be derived.

5.4.3 Magnetic Tweezers for DEP force calibration

We integrated magnetic tweezers and DEP tweezers on the same chip so that we could calibrate DEP force using magnetic tweezers. In a typical experiment, as the electromagnet current (magnetic tweezers) or AC voltage (DEP tweezers) is ramped, the force applied to the bead increases and stretches the DNA molecule. The instrument synchronously captures applied current (voltage) and a digital movie of the bead attached to a DNA anchored at the surface of the fluid cell. Each single molecule stretching curve

is plotted as a normalized bead intensity (with respect to the maximum intensity) versus applied current (voltage) in order to perform side-by-side comparison of different evanescent field penetration depths, different beads or molecules, etc. The intensity versus current curve is the raw data that can be interpreted as an extension-versus-applied-force curve, if proper calibration parameters are available. A comparison of the force-extension loops conducted at different rates indicated that retraction curves align without a dependence on rate and could be captured as fast as fast 1-10 sec per curve (Figure 5.6).

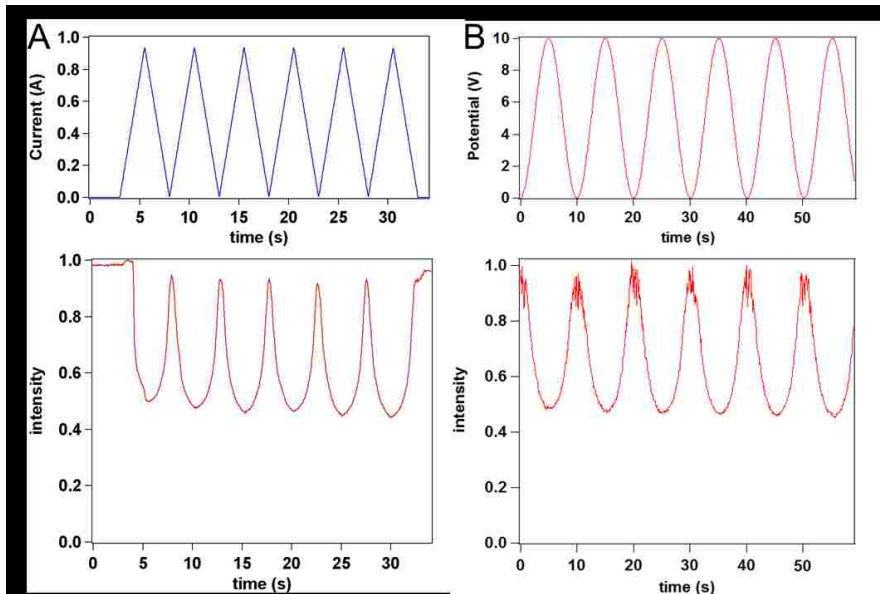


Figure 5.6 The forces on the DNA molecule can be generated using either magnetic (A) or DEP (B) tweezers. The 200-base long ssDNA molecule is immobilized on the surface and bound to the surface of the bead. When the magnetic or DEP force is applied (via coil current or AC voltage amplitude changes – top panels), the brightness of the probe fluorescence in the evanescent field drops by approximately 50%, consistent with the probe being pulled away from the surface and the DNA molecule being stretched.

We observed that the two methods – DEP tweezers and magnetic tweezers – were effectively equivalent when we applied both methods of acquiring force-extension curves to the same molecule-bead construct in the same microwell. Resulting intensity-voltage and intensity-current curves (Figure 5.7) show the same dynamic range indicating that very similar extension of the molecule was reached in both cases. When analyzing the force extension curves, the method at which they were collected must be noted since the force is proportional to voltage squared for DEP tweezers and current for magnetic tweezers. We note that DEP tweezers, when compared magnetic tweezers, have the advantage of incorporation of the critical alignment into the sample fabrication step. Lithographic procedures define electrode characteristics, which therefore should be uniform across centimeter-wide areas and independent of positioning of external elements (such as magnets).

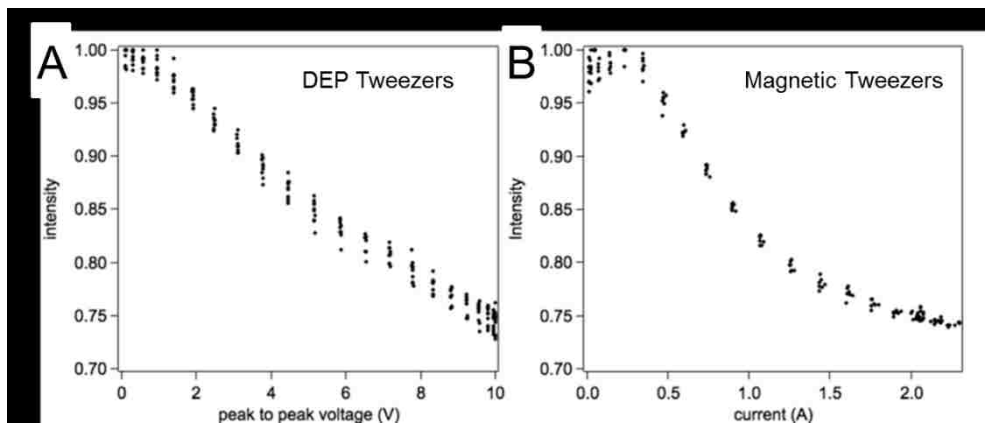


Figure 5.7 Direct comparison of the DNA stretching curves obtained with DEP tweezers (A) and magnetic tweezers (B) using the same superparamagnetic bead-ssDNA pair. Both experiments used a bead positioned inside a microwell and illuminated by the evanescent wave. Since the decrease in the probe intensity for both DEP and magnetic tweezers is the same, the range of forces achieved in the two molecular tweezers arrangements should also be the same.

5.4.4 Highly parallel SMFS and analysis of ssDNA stretching

Program tracked 57 probes (out of total 85 occupied locations) labeled from 0 to 56 in Figure 5e and generated potential versus probe intensity curves for each bead (a representative curve is shown in Figure 5f and all the curves are compiled in the section S4 of supporting information). The majority of the non-indexed positions contain multiple probes, which appear to be bound and conducting some form of force spectroscopy, but not suitable for interpretation. Of the indexed force probes, we can extract usable force curves from 53 (or 93 %) of the single probes. These 53 probes conducting force spectroscopy in one field of view is an order of magnitude improvement over the <5 active probes we have observed in our early experiments prior to optimization of surface and solution chemistry. We must note that some of the force curves do not comply with the shape expected for single molecule stretching. This aberration is most likely a result of multiple DNA molecules binding to a single probe and is the subject of ongoing experimentation to improve control of the spacing between DNA molecules on the surface of the substrate to avoid multiple tethering.

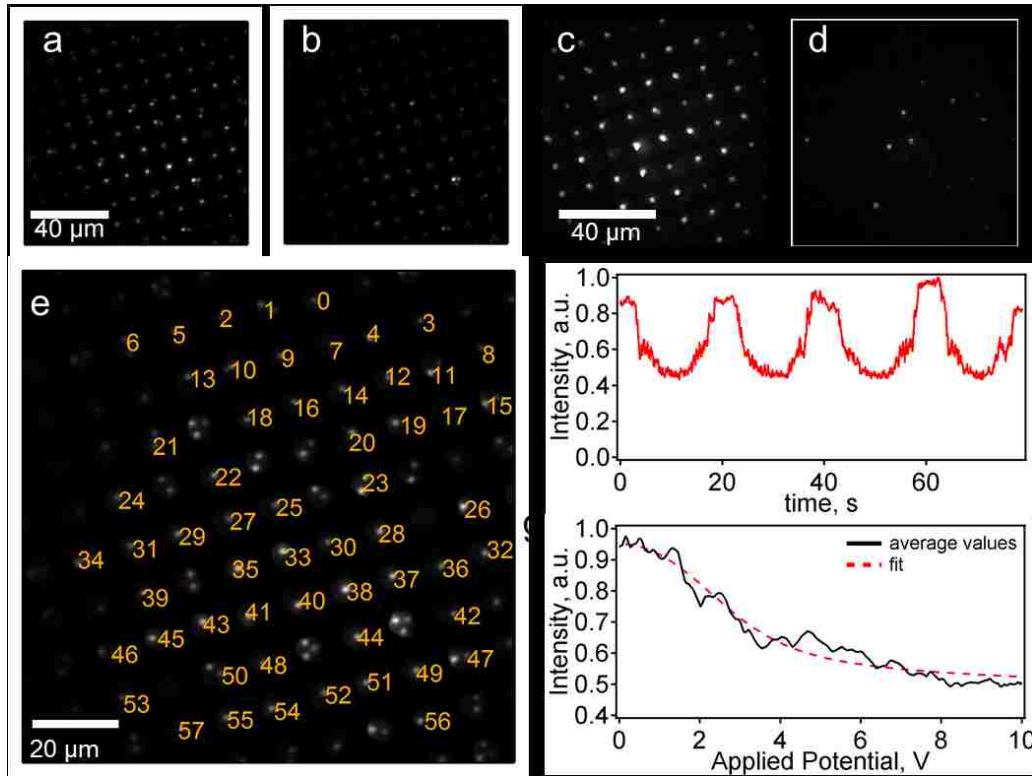


Figure 5.8 Force spectroscopy of ssDNA conducted using DEP tweezers on a system optimized using design principles based on results from this paper. Force probes tethered to DNA in wells before (a) and after (b) they were exposed to a DEP force. Free force probes settled in wells before (c) and after (d) the DEP force was applied. The brightness of the probes (a-d) varies due to Gaussian profile of the illumination laser beam and variations in the bead sizes. (e) A single frame from a movie of the probes, showing the indexing of the force probes for data analysis. (f) A representative intensity vs. voltage plot for one probe. (g) Fits of the data from the plot in part f.

We can use these force curves both to calibrate forces acting on each probe and to determine if the force spectra are reasonable. To fully describe the relationship between applied voltage and extension, we can re-write DEP force as:

$$F_{DEP} = S_f V^2 \quad (5-25)$$

where S_f is the sensitivity factor and V is the applied voltage. By substituting equation, we can finally have

$$I(V) = I_0 \exp \left(-\frac{Nl_{ss}}{d} \left[\coth \left(\frac{F_{DEP} b_{ss}}{k_B T} \right) - \frac{k_B T}{F_{DEP} b_{ss}} \right] \left[1 + \frac{F_{DEP}}{K_{ss}} \right] \right) \quad (5-26)$$

To analyze the data, we averaged the normalized intensity-versus-applied-potential curves from one of the probes (Figure 5.8f) and fitted the result (Figure 5.8g) to the equation. The terms in the fitting equation include the total number of bases in the DNA strand ($N=142$), the contour length of a single base ($l_{ss}=0.58$ nm), the Kuhn length of the ssDNA ($b_{ss}=1.4$ nm,) and the segment elasticity of the ssDNA ($K_{ss}=905$ pN,). The curve was fitted for the initial intensity of the probe, I_0 , the force sensitivity factor, S_f , and the penetration depth of the evanescent field, d . Upon fitting the equation to our data (Figure 5g), we determine that these parameters are equal to 0.953, 0.56 pN/V², and 137 nm, respectively. The initial intensity is close to 1 since the curves were initially normalized to maximum intensity observed for a given probe. The penetration depth was found to be 137 nm, which is in the center of the typical range of values we get for our system. To determine the plausibility of the value obtained for the sensitivity factor, we determined a maximum force applied to the system by multiplying S_f by the maximum voltage squared. The estimate yields a maximum force of 56 pN, which is also a typical value for this setup. This analysis shows that one can conduct force spectroscopy in a parallel manner using finely tuned system to assemble high density tethered bead arrays.

5.5 Conclusions

We have demonstrated a practical implementation of DEP tweezers with evanescent nanometry for quantitative detection of DNA elasticity. Individual force-extension curves can be acquired in a continuous manner in 5-10 seconds. DEP force was calibrated by

fitting the potential energy profile, comparing to magnetic tweezers and fitting the ssDNA force-extension curve to expected behavior of force-extension. We validated the use of a fit to the stretching model for ssDNA as a method for internal calibration of both the penetration depth and DEP force. The simplified model for obtaining both penetration depths and a force calibration from a known DNA strand is especially useful in cases where the differences after a biological event (DNA hybridization, protein binding, polymerization, etc.) are more important than initial characterization of the biomolecule itself.

Chapter 6 Conclusions

We developed a massively parallel SMFS platform using dielectrophoresis combined with evanescent field excitation. As outlined in the first chapter: 1) We have fabricated magnetic fluorescent polymer force probes with surface functionality, which is suitable for various of SMFS platforms and other bio-analysis. 2) We have developed the surface chemistry and reaction conditions for highly parallel single-molecule-single-bead arrays. 3) We numerically modeled several DEP tweezers design and implemented the optimal design to stretch single DNA molecules in a parallel manner. 4) We established the DEP force calibration methods and finally obtained the elasticity of single DNA molecule by analyzing the force-extension curve, which is conducted using DEP tweezers.

Currently, there are three major ways to apply forces to single molecules (Table 6.1): atomic force microscopy, optical tweezers, and magnetic tweezers. In AFM, a microfabricated force probe (AFM tip) is moved by the piezoelectric scanner with sub-Angstrom precision. Often, one deposits single molecule of interest (synthetic polymers, DNA, proteins) on a solid surface. The tip is used to pick up the single molecule of interest using nonspecific or specific interactions, the molecule stretches, unfolds, and eventually detaches from the tip at high forces – and then the process repeats. Since only one force probe can be used in AFM experiments, one can only stretch one molecule at a time which is not suitable for data acquisition on large or heterogeneous samples (e.g. different DNA sequences or proteins). AFM is not meant to operate under constant force. The common experimental mode is displacement control (or constant rate of displacement) of the base of the cantilever and the proper analysis of the force data

should be done in Helmholtz ensemble that includes the force probe. The effect of the tip is often ignored by assuming force-controlled conditions (soft cantilever or Gibbs ensemble). The assumption of constant force loading rate is often incorrect due to changing stiffness of the molecule being stretched.

Table 6.1 Comparison of current single-molecule force spectroscopy methods with DEP Tweezers

	Atomic Force Microscopy	Optical Tweezers	Magnetic Tweezers	DEP Tweezers
Features	High maximum force magnitude (~10 nN) High spatial resolution for positioning and imaging Easy calibration for force and extension	Broad force range (~10 fN – 100 pN) High spatial and temporal resolution	Broad force range (~10 fN – 100 pN) Torque sensitive Parallel (~10 ² probes)	Broad force range with high maximum force (~10 fN – 1 nN) Highly Parallel (infinite probes theoretically)
Limitations and drawbacks	Large minimal force (~10 pN) One molecule per experiment Sensitive to mechanical drift	Small forces (< 100 pN) Local heating and photodamage Complicated extension to multiple probes (~10 ¹ probes) Sensitive to mechanical drift	Small forces (< 100 pN) Not a true 3D trap Hysteresis Complicated mapping of extension to imaging Sensitive to mechanical drift	Non-linear forces as position of probes change Complicated mapping of extension to imaging

For optical tweezers, the force probe is optically trapped in a 3-dimensional potential well. There are some technical issues associated with using light to manipulate force probes. In order to apply large forces, one needs to use high power lasers which may

result in photodamage to the sample and local heating. Even with μm -sized beads, relatively low forces are exerted (<100 pN). A complicated trapping configuration is very sensitive to mechanical drift and optical distortions. One can potentially trap more than one probe by either moving a single beam between several beads (using acousto-optic deflectors) or by splitting a single beam into multiple traps (by imposing a spatially encoded phase with holographic masks). These configurations of scanning optical tweezers or holographic optical tweezers, which offer the ability to manipulate multiple force probes, are relatively difficult to set up and operate on a large scale with limited speed to reconfigure among multiple probes. Ultimately, the need to produce tightly focused beams with high numerical aperture (NA) objectives limits the size of the sample area to ~ 100 μm . Expansion to mm- or cm-sized areas required for scale up to 10^3 - 10^6 probes is not feasible.

The most promising method so far for implementing parallel SMFS has been magnetic tweezers. One can use both permanent magnets and electromagnets to conduct magnetic tweezers experiments. Since the distance between force probe and the magnet is much larger than changes in molecular extension, the setup operates as a passive force clamp. To acquire force-distance curves, one has to move permanent magnets with respect to the sample, thus making continuous data capture problematic due to mechanical noise. Magnetic tweezers use μm -sized superparamagnetic beads resulting in relatively low forces (<100 pN). The need to use specially-designed (i.e. magnetic versus simple dielectric) probes available from a select few (1-2) commercial sources is a disadvantage.

Vlaminck *et al.* showed that 357 molecules can be simultaneously pulled or rotated while using permanent magnets⁹⁴. However, maximum 1.8 pN, a very low force, could be applied to all the force probes in this setup. The ability to produce high forces is limited by i) proximity to the magnet, which is external to the fluid cell setup, ii) need for blunt geometry of the ferromagnetic material (permanent magnet bar or the core of electromagnet), since sharp features will result in increase in the gradient in both the desired direction (normal to the surface of support) and undesirable (lateral) direction, and iii) materials properties, such as saturation magnetization in the magnet and domain magnetization of the magnetic material (typically, magnetite nanoparticles) used in the force probes.

DEP Tweezers has a number of advantages over three major types of force spectroscopy platforms: 1) DEP Tweezers can apply relatively high force (~1 nN); 2) The electric field is evenly distributed over the whole sample area so that theoretically DEP Tweezers could conduct force-extension measurements on infinite number of molecules; 3) Fabrication of DEP chips can be easily scale up. 4) No effect of the mechanical drift.

With DEP tweezers technique, both the force and the distance measurements are referenced to the surface of the electrode, thus, *an internal reference is built into each sample by design*. The measurement of molecular extension using an evanescent field is differential in nature – the corresponding signal depends on the probe-surface separation only, not on the relative position of some external handle (such as an AFM cantilever or optical beam). As a result, the effect of the mechanical drift is reduced dramatically.

DEP Tweezers share the same drawback and limitation with Magnetic Tweezers as the complicated mapping of extension to imaging. In addition, since the dielectric particle will disturb the electric field, the electric field changes when particle moves, which lead to a non-linear force when we do force-extension experiments. For stretching short DNA molecules (~ 100 mer), this non-linear effect is not significant since the overall displacement of the particle is about 60 nm. For stretching longer molecule, however, this non-linear effect need to be taking account.

The force that exerted on the force probe for DEP Tweezers and Magnetic Tweezers are all depend on the volume of the particle, which cause the difficulty for force calibration. For genome sequencing purposes, the force calibration is not necessary since we are only acquiring the different extensions under the same forces (which does not need to be a known absolute value). We calibrated DEP forces using several commonly accepted method to investigate the effectiveness of numerical simulation and the magnitude of the DEP force.

We have shown that moving away from TIRF and instead using forward scattering scheme can enlarge the observation area by an order of magnitude. Using smaller force probes (hundreds of nanometers) can also be implemented in DEP tweezers by carefully design the electrodes geometry. Future experiments should investigate the detection of DNA double character by applying DEP tweezers to genomic DNA molecules.

There are other potential applications of DEP Tweezers. One of the important application is studying cell mechanics. Since any dielectric particles has DEP effect, cells can be manipulated in DEP Tweezers. We are using DEP Tweezers to trap specific cells

in the microwells, pull cells from different surfaces and squeeze cells in the bottom of the microwells. We believe DEP Tweezers will be the fourth major molecular force spectroscopy platforms and be useful not only in proposed genome sequencing technique, but also in other biophysical world.

References

1. J. A. Schloss, How to get genomes at one ten-thousandth the cost, *Nat Biotech*, 2008, 26, 1113-1115.
2. R. Mukhopadhyay, DNA sequencers: the next generation, *Analytical Chemistry*, 2009, 81, 1736-1740.
3. J. Shendure and H. Ji, Next-generation DNA sequencing, *Nat Biotech*, 2008, 26, 1135-1145.
4. I. Braslavsky, B. Hebert, E. Kartalov and S. R. Quake, Sequence information can be obtained from single DNA molecules, *P Natl Acad Sci USA*, 2003, 100, 3960-3964.
5. S. L. Cockroft, J. Chu, M. Amarin and M. R. Ghadiri, A single-molecule nanopore device detects DNA polymerase activity with single-nucleotide resolution, *Journal of the American Chemical Society*, 2008, 130, 818-820.
6. T. D. Harris, P. R. Buzby, H. Babcock, E. Beer, J. Bowers, I. Braslavsky, M. Causey, J. Colonell, J. Dimeo, J. W. Efcavitch, E. Giladi, J. Gill, J. Healy, M. Jarosz, D. Lapen, K. Moulton, S. R. Quake, K. Steinmann, E. Thayer, A. Tyurina, R. Ward, H. Weiss and Z. Xie, Single-molecule DNA sequencing of a viral genome, *Science*, 2008, 320, 106-109.
7. J. Eid, A. Fehr, J. Gray, K. Luong, J. Lyle, G. Otto, P. Peluso, D. Rank, P. Baybayan, B. Bettman, A. Bibillo, K. Bjornson, B. Chaudhuri, F. Christians, R. Cicero, S. Clark, R. Dalal, A. deWinter, J. Dixon, M. Foquet, A. Gaertner, P. Hardenbol, C. Heiner, K. Hester, D. Holden, G. Kearns, X. Kong, R. Kuse, Y. Lacroix, S. Lin, P. Lundquist, C. Ma, P. Marks, M. Maxham, D. Murphy, I. Park, T. Pham, M. Phillips, J. Roy, R. Sebra, G. Shen, J. Sorenson, A. Tomaney, K. Travers, M. Trulson, J. Vieceli, J. Wegener, D. Wu, A. Yang, D. Zaccarin, P. Zhao, F. Zhong, J. Korlach and S. Turner, Real-Time DNA Sequencing from Single Polymerase Molecules, *Science*, 2009, 323, 133-138.
8. M. Metzker, Sequencing technologies—the next generation, *Nature Reviews Genetics*, 2009, 11, 31-46.
9. F. Ding, M. Manosas, M. M. Spiering, S. J. Benkovic, D. Bensimon, J.-F. Allemand and V. Croquette, Single-molecule mechanical identification and sequencing, *Nat Meth*, 2012, 9, 367-372.
10. A. Ramanathan, E. J. Huff, C. C. Lamers, K. D. Potamiosis, D. K. Forrest and D. C. Schwartz, An integrative approach for the optical sequencing of single DNA molecules, *Analytical Biochemistry*, 2004, 330, 227-241.
11. J.-B. Fan, M. S. Chee and K. L. Gunderson, Highly parallel genomic assays, *Nat Rev Genet*, 2006, 7, 632-644.

12. D. Branton, D. Deamer, A. Marziali, H. Bayley, S. Benner, T. Butler, M. Di Ventra, S. Garaj, A. Hibbs, X. Huang, S. Jovanovich, P. Krstic, S. Lindsay, X. Ling, C. Mastrangelo, A. Meller, J. Oliver, Y. Pershin, J. Ramsey, R. Riehn, G. Soni, V. Tabard-Cossa, M. Wanunu, M. Wiggin and J. Schloss, The potential and challenges of nanopore sequencing, *Nat Biotechnol*, 2008, 26, 1146-1153.
13. S. W. Kowalczyk, M. W. Tuijtel, S. P. Donkers and C. Dekker, Unraveling Single-Stranded DNA in a Solid-State Nanopore, *Nano Letters*, 2010, 10, 1414-1420.
14. A. Meller and D. Branton, Single molecule measurements of DNA transport through a nanopore, *ELECTROPHORESIS*, 2002, 23, 2583-2591.
15. S. Benner, R. J. A. Chen, N. A. Wilson, R. Abu-Shumays, N. Hurt, K. R. Lieberman, D. W. Deamer, W. B. Dunbar and M. Akeson, Sequence-specific detection of individual DNA polymerase complexes in real time using a nanopore, *Nat Nano*, 2007, 2, 718-724.
16. B. McNally, A. Singer, Z. Yu, Y. Sun, Z. Weng and A. Meller, Optical Recognition of Converted DNA Nucleotides for Single-Molecule DNA Sequencing Using Nanopore Arrays, *Nano Letters*, 2010, 10, 2237-2244.
17. J. Shendure, G. Porreca, N. Reppas, X. Lin, J. McCutcheon, A. Rosenbaum, M. Wang, K. Zhang, R. Mitra and G. Church, Accurate multiplex polony sequencing of an evolved bacterial genome, *Science*, 2005, 309, 1728-1732.
18. K. C. Neuman and A. Nagy, Single-molecule force spectroscopy: optical tweezers, magnetic tweezers and atomic force microscopy, *Nat Meth*, 2008, 5, 491-505.
19. J. Liang and J. M. Fernandez, Mechanochemistry: One Bond at a Time, *ACS Nano*, 2009, 3, 1628-1645.
20. M. Kruithof, F. Chien, M. De Jager and J. Van Noort, Subpiconewton Dynamic Force Spectroscopy Using Magnetic Tweezers, *Biophysical Journal*, 2008, 94, 2343-2348.
21. C. Gosse and V. Croquette, Magnetic Tweezers: Micromanipulation and Force Measurement at the Molecular Level, *Biophysical Journal*, 2002, 82, 3314-3329.
22. A. Noy, D. Vezenov and C. Lieber, in *Handbook of Molecular Force Spectroscopy: Chemical Force Microscopy Nanoscale Probing of Fundamental Chemical Interactions*, ed. A. Noy, Springer US, 2008, DOI: 10.1007/978-0-387-49989-5_3, ch. 3, pp. 97-122.
23. R. Conroy and A. Noy, *Handbook of Molecular Force Spectroscopy: Force Spectroscopy with Optical and Magnetic Tweezers, Ed.*, 2008.
24. P. Cheng, M. J. Barrett, P. M. Oliver, D. Cetin and D. Vezenov, Dielectrophoretic tweezers as a platform for molecular force spectroscopy in a highly parallel format, *Lab on a Chip*, 2011, 11, 4248-4259.

25. M. J. Barrett, P. M. Oliver, P. Cheng, D. Cetin and D. Vezenov, High Density Single-Molecule-Bead Arrays for Parallel Single Molecule Force Spectroscopy, *Analytical Chemistry*, 2012, 84, 4907-4914.
26. S. B. Smith, Y. Cui and C. Bustamante, Overstretching B-DNA: The Elastic Response of Individual Double-Stranded and Single-Stranded DNA Molecules, *Science*, 1996, 271, 795-799.
27. C. Bustamante, Z. Bryant and S. B. Smith, Ten years of tension: single-molecule DNA mechanics, *Nature*, 2003, 421, 423-427.
28. J. Regtmeier, R. Eichhorn, M. Viefhues, L. Bogunovic and D. Anselmetti, Electrodeless dielectrophoresis for bioanalysis: Theory, devices and applications, *ELECTROPHORESIS*, 2011, 32, 2253-2273.
29. B. H. Lapizco-Encinas and M. Rito-Palomares, Dielectrophoresis for the manipulation of nanobiotparticles, *ELECTROPHORESIS*, 2007, 28, 4521-4538.
30. P. M. Oliver, J. S. Park and D. V. Vezenov, Quantitative high-resolution sensing of DNA hybridization using magnetic tweezers with evanescent illumination., *Nanoscale*, 2011, 3, 581-591.
31. O. H. Willemsen, M. M. E. Snel, A. Cambi, J. Greve, B. G. De Grooth and C. G. Figdor, Biomolecular Interactions Measured by Atomic Force Microscopy, *Biophysical Journal*, 2000, 79, 3267-3281.
32. A. Janshoff, M. Neitzert, Y. Oberdörfer and H. Fuchs, Force Spectroscopy of Molecular Systems—Single Molecule Spectroscopy of Polymers and Biomolecules, *Angewandte Chemie International Edition*, 2000, 39, 3212-3237.
33. D. V. Vezenov, A. Noy, L. F. Rozsnyai and C. M. Lieber, Force Titrations and Ionization State Sensitive Imaging of Functional Groups in Aqueous Solutions by Chemical Force Microscopy, *Journal of the American Chemical Society*, 1997, 119, 2006-2015.
34. C. Danilowicz, D. Greenfield and M. Prentiss, Dissociation of Ligand-Receptor Complexes Using Magnetic Tweezers, *Analytical Chemistry*, 2005.
35. F. Assi, R. Jenks, J. Yang, C. Love and M. Prentiss, Massively parallel adhesion and reactivity measurements using simple and inexpensive magnetic tweezers, *J Appl Phys*, 2002, 92, 5584-5586.
36. Y. W. Jun, Y. M. Huh, J. S. Choi, J. H. Lee, H. T. Song, S. Kim, S. Yoon, K. S. Kim, J. S. Shin, J. S. Suh and J. Cheon, Nanoscale size effect of magnetic nanocrystals and their utilization for cancer diagnosis via magnetic resonance imaging, *Journal of the American Chemical Society*, 2005, 127, 5732-5733.
37. J. Park, K. J. An, Y. S. Hwang, J. G. Park, H. J. Noh, J. Y. Kim, J. H. Park, N. M. Hwang and T. Hyeon, Ultra-large-scale syntheses of monodisperse nanocrystals, *Nature Materials*, 2004, 3, 891-895.

38. B. L. Cushing, V. L. Kolesnichenko and C. J. O'Connor, Recent advances in the liquid-phase syntheses of inorganic nanoparticles, *Chemical Reviews*, 2004, 104, 3893-3946.
39. A. S. P. A. Petukhova, Z. Wei, I. Gourevich, S. V. Nair, H. E. Ruda, A. Shik, E. Kumacheva, Polymer Multilayer Microspheres Loaded with Semiconductor Quantum Dots, *Advanced Functional Materials*, 2008, 18, 1-8.
40. J. Pyun, Nanocomposite materials from functional polymers and magnetic colloids, *Polymer Reviews*, 2007, 47, 231-263.
41. F. Caruso, Nanoengineering of particle surfaces, *Advanced Materials*, 2001, 13, 11-22.
42. C. Mangeney, M. Fertani, S. Bousalem, M. Zhicai, S. Ammar, F. Herbst, P. Beaunier, A. Elaissari and M. M. Chehimi, Magnetic Fe₂O₃-polystyrene/PPy Core/shell particles: Bioreactivity and self-assembly, *Langmuir*, 2007, 23, 10940-10949.
43. Z. Y. Ma, Y. P. Guan, X. Q. Liu and H. Z. Liu, Synthesis of magnetic chelator for high-capacity immobilized metal affinity adsorption of protein by cerium initiated graft polymerization, *Langmuir*, 2005, 21, 6987-6994.
44. F. Sauzedde, A. Elaissari and C. Pichot, Hydrophilic magnetic polymer latexes. 2. Encapsulation of adsorbed iron oxide nanoparticles, *Colloid and Polymer Science*, 1999, 277, 1041-1050.
45. Y. Li, E. C. Y. Liu, N. Pickett, P. J. Skabara, S. S. Cummins, S. Ryley, A. J. Sutherland and P. O'Brien, Synthesis and characterization of CdS quantum dots in polystyrene microbeads, *Journal of Materials Chemistry*, 2005, 15, 1238-1243.
46. P. O'Brien, S. S. Cummins, D. Darcy, A. Dearden, O. Masala, N. L. Pickett, S. Ryley and A. J. Sutherland, Quantum dot-labelled polymer beads by suspension polymerisation, *Chemical Communications*, 2003, DOI: Doi 10.1039/B307500a, 2532-2533.
47. N. G. Liu, B. S. Prall and V. I. Klimov, Hybrid gold/silica/nanocrystal-quantum-dot superstructures: Synthesis and analysis of semiconductor-metal interactions, *Journal of the American Chemical Society*, 2006, 128, 15362-15363.
48. W. R. Zhao, J. L. Gu, L. X. Zhang, H. R. Chen and J. L. Shi, Fabrication of uniform magnetic nanocomposite spheres with a magnetic core/mesoporous silica shell structure, *Journal of the American Chemical Society*, 2005, 127, 8916-8917.
49. H. H. Yang, S. Q. Zhang, X. L. Chen, Z. X. Zhuang, J. G. Xu and X. R. Wang, Magnetite-containing spherical silica nanoparticles for biocatalysis and bioseparations, *Analytical Chemistry*, 2004, 76, 1316-1321.
50. S. Mornet, S. Vasseur, F. Grasset, P. Veverka, G. Goglio, A. Demourgues, J. Portier, E. Pollert and E. Duguet, Magnetic nanoparticle design for medical applications, *Progress in Solid State Chemistry*, 2006, 34, 237-247.

51. G. Reiss and A. Hutten, Magnetic nanoparticles - Applications beyond data storage, *Nature Materials*, 2005, 4, 725-726.
52. I. L. Medintz, H. T. Uyeda, E. R. Goldman and H. Mattoussi, Quantum dot bioconjugates for imaging, labelling and sensing, *Nature Materials*, 2005, 4, 435-446.
53. M. Bruchez, M. Moronne, P. Gin, S. Weiss and A. P. Alivisatos, Semiconductor nanocrystals as fluorescent biological labels, *Science*, 1998, 281, 2013-2016.
54. K. E. Sapsford, T. Pons, I. L. Medintz and H. Mattoussi, Biosensing with luminescent semiconductor quantum dots, *Sensors*, 2006, 6, 925-953.
55. J. Lim, S. Jun, E. Jang, H. Baik, H. Kim and J. Cho, Preparation of highly luminescent nanocrystals and their application to light-emitting diodes, *Advanced Materials*, 2007, 19, 1927-1932.
56. J. Il Kim and J. K. Lee, Sub-kilogram-scale one-pot synthesis of highly luminescent and monodisperse core/shell quantum dots by the successive injection of precursors, *Advanced Functional Materials*, 2006, 16, 2077-2082.
57. G. T. Simon M. Joscelyne, Membrane emulsification — a literature review, *Journal of Membrane Science*, 2000, 169, 107-117.
58. O. B. Volker Schröder, Helmar Schubert, Effect of Dynamic Interfacial Tension on the Emulsification Process Using Microporous, Ceramic Membranes, *Journal of Colloid and Interface Science*, 1998, 202, 334-340.
59. C. W. Fuller, L. R. Middendorf, S. A. Benner, G. M. Church, T. Harris, X. Huang, S. B. Jovanovich, J. R. Nelson, J. A. Schloss, D. C. Schwartz and D. V. Vezenov, The challenges of sequencing by synthesis, *Nat. Biotechnol.*, 2009, 27, 1013-1023.
60. P. C. Nelson, C. Zurla, D. Brogioli, J. F. Beausang, L. Finzi and D. Dunlap, Tethered Particle Motion as a Diagnostic of DNA Tether Length, *The Journal of Physical Chemistry B*, 2006, 110, 17260-17267.
61. D. J. Schlingman, A. H. Mack, S. G. J. Mochrie and L. Regan, A new method for the covalent attachment of DNA to a surface for single-molecule studies, *Colloids and Surfaces B: Biointerfaces*, 2011, 83, 91-95.
62. K. A. Burrige, M. A. Figa and J. Y. Wong, Patterning Adjacent Supported Lipid Bilayers of Desired Composition To Investigate Receptor–Ligand Binding under Shear Flow, *Langmuir*, 2004, 20, 10252-10259.
63. M. Wilchek and E. A. Bayer, The avidin-biotin complex in bioanalytical applications, *Analytical Biochemistry*, 1988, 171, 1-32.
64. J. S. Shumaker-Parry, M. H. Zareie, R. Aebersold and C. T. Campbell, Microspotting Streptavidin and Double-Stranded DNA Arrays on Gold for High-Throughput Studies of Protein–DNA Interactions by Surface Plasmon Resonance Microscopy, *Analytical Chemistry*, 2004, 76, 918-929.

65. D. Petrovykh, H. Kimura-Suda, L. Whitman and M. Tarlov, Quantitative analysis and characterization of DNA immobilized on gold, *J Am Chem Soc*, 2003, 125, 5219-5226.
66. A. Opdahl, D. Petrovykh, H. Kimura-Suda, M. J. Tarlov and L. J. Whitman, Independent control of grafting density and conformation of single-stranded DNA brushes, *Proceedings of the National Academy of Sciences*, 2007, 104, 9-14.
67. G. Sánchez-Pomales, L. Santiago-Rodríguez, N. E. Rivera-Vélez and C. R. Cabrera, Control of DNA self-assembled monolayers surface coverage by electrochemical desorption, *Journal of Electroanalytical Chemistry*, 2007, 611, 80-86.
68. W. Kaiser and U. Rant, Conformations of End-Tethered DNA Molecules on Gold Surfaces: Influences of Applied Electric Potential, Electrolyte Screening, and Temperature, *J Am Chem Soc*, 2010, 132, 7935-7945.
69. H. Y. Park, H. Li, E. S. Yeung and M. D. Porter, Single molecule adsorption at compositionally patterned self-assembled monolayers on gold: Role of domain boundaries, *Langmuir*, 2006, 22, 4244-4249.
70. F. Stefani, K. Vasilev, N. Bocchio, N. Stoyanova and M. Kreiter, Surface-Plasmon-Mediated Single-Molecule Fluorescence Through a Thin Metallic Film, *Phys. Rev. Lett.*, 2005, 94, 023005.
71. A. Csaki, R. Moller, W. Straube, J. Kohler and W. Fritzsche, DNA monolayer on gold substrates characterized by nanoparticle labeling and scanning force microscopy, *Nucleic Acids Research*, 2001, 29, art. no.-e81.
72. K. M. Andersson and L. Bergström, DLVO Interactions of Tungsten Oxide and Cobalt Oxide Surfaces Measured with the Colloidal Probe Technique, *Journal of Colloid and Interface Science*, 2002, 246, 309-315.
73. H. Ono and E. Jidai, Stability of polymethyl methacrylate latex dispersions prepared by using mixtures of anionic and nonionic surfactants, *Colloid Polym. Sci.*, 1976, 254, 17-24.
74. G. V. Dedkov, E. G. Dedkova, R. I. Tegaev and K. B. Khokonov, Measuring van der Waals and electrostatic forces for an atomic force microscope probe contacting with metal surfaces, *Tech. Phys. Lett.*, 2008, 34, 17-21.
75. M. Rief, J. Pascual, M. Saraste and H. E. Gaub, Single molecule force spectroscopy of spectrin repeats: low unfolding forces in helix bundles, *Journal of Molecular Biology*, 1999, 286, 553-561.
76. V. Barsegov, D. K. Klimov and D. Thirumalai, Mapping the Energy Landscape of Biomolecules Using Single Molecule Force Correlation Spectroscopy: Theory and Applications, *Biophysical Journal*, 2006, 90, 3827-3841.
77. M. Rief and H. Grubmüller, Force Spectroscopy of Single Biomolecules, *ChemPhysChem*, 2002, 3, 255-261.

78. D. Thirumalai, E. P. O'Brien, G. Morrison and C. Hyeon, Theoretical Perspectives on Protein Folding, *Annual Review of Biophysics*, 2010, 39, 159-183.
79. S. H. Baek, W.-J. Chang, J.-Y. Baek, D. S. Yoon, R. Bashir and S. W. Lee, Dielectrophoretic Technique for Measurement of Chemical and Biological Interactions, *Analytical Chemistry*, 2009, 81, 7737-7742.
80. J. Voldman, ELECTRICAL FORCES FOR MICROSCALE CELL MANIPULATION, *Annual Review of Biomedical Engineering*, 2006, 8, 425-454.
81. K. D. Barbee, A. P. Hsiao, E. E. Roller and X. Huang, Multiplexed protein detection using antibody-conjugated microbead arrays in a microfabricated electrophoretic device, *Lab on a Chip*, 2010, 10, 3084-3093.
82. W. Qiao, G. Cho and Y.-H. Lo, Wirelessly powered microfluidic dielectrophoresis devices using printable RF circuits, *Lab on a Chip*, 2011, 11, 1074-1080.
83. W. D. Ristenpart, I. A. Aksay and D. A. Saville, Electrically Guided Assembly of Planar Superlattices in Binary Colloidal Suspensions, *Physical Review Letters*, 2003, 90, 128303.
84. A. Winkleman, L. S. McCarty, Z. Ting, D. B. Weibel, S. Zhigang and G. M. Whitesides, Templated Self-Assembly Over Patterned Electrodes by an Applied Electric Field: Geometric Constraints and Diversity of Materials, *Microelectromechanical Systems, Journal of*, 2008, 17, 900-910.
85. I. Barbulovic-Nad, X. Xuan, J. S. H. Lee and D. Li, DC-dielectrophoretic separation of microparticles using an oil droplet obstacle, *Lab on a Chip*, 2006, 6, 274-279.
86. H. Chu, I. Doh and Y.-H. Cho, A three-dimensional (3D) particle focusing channel using the positive dielectrophoresis (pDEP) guided by a dielectric structure between two planar electrodes, *Lab on a Chip*, 2009, 9, 686-691.
87. N. G. Green and H. Morgan, Dielectrophoretic investigations of sub-micrometre latex spheres, *Journal of Physics D: Applied Physics*, 1997, 30, 2626.
88. M.-T. Wei, J. Junio and H. D. Ou-Yang, Direct measurements of the frequency-dependent dielectrophoresis force, *Biomicrofluidics*, 2009, 3, 012003-012008.
89. J. J. Juarez, J.-Q. Cui, B. G. Liu and M. A. Bevan, kT-Scale Colloidal Interactions in High Frequency Inhomogeneous AC Electric Fields. I. Single Particles, *Langmuir*, 2011, DOI: 10.1021/la201478y, null-null.
90. P. Cheng, P. M. Oliver, M. J. Barrett and D. Vezenov, Progress toward the application of molecular force spectroscopy to DNA sequencing, *ELECTROPHORESIS*, 2012, 33, 3497-3505.
91. M. A. Bevan and D. C. Prieve, Hindered diffusion of colloidal particles very near to a wall: Revisited, *The Journal of Chemical Physics*, 2000, 113, 1228-1236.

92. H.-J. Wu and M. A. Bevan, Direct Measurement of Single and Ensemble Average Particle–Surface Potential Energy Profiles, *Langmuir*, 2005, 21, 1244-1254.
93. P. Dennis C, Measurement of colloidal forces with TIRM, *Advances in Colloid and Interface Science*, 1999, 82, 93-125.

Curriculum Vitae

Peng Cheng

Department of Chemistry
Lehigh University
6 E. Packer Ave.
Bethlehem, PA 18015

tel: (610) 844-6597
e-mail: pec208@lehigh.edu
web: www.lehigh.edu/~pec208/welcome.html

SUMMARY

PhD level chemist experienced in surface science and surface chemistry, small molecule and polymer synthesis, microscopy, instrument development, and general analytical chemistry. Key strength is integrating multi-disciplinary methods to develop new MEMS for bioanalysis. Specialties include covalent and non-covalent surface modification, nano- and microfabrication, thin film analysis, and single molecule force spectroscopy.

EDUCATION

- 2008 – present Ph.D candidate (degree expected in 2014), Department of Chemistry, Lehigh University, Bethlehem, PA.
Thesis Title: “Dielectrophoretic tweezers: a new tool for molecular force spectroscopy”
Advisor: Prof. Dmitri Vezenov
- 2004 – 2008 B.S., Chemistry, Nankai University, Tianjin, China.
Senior Project: “Assembly of nanometer-sized core-shell polymer particles and spectroscopy characterization”
Advisor: Prof. Zhanyong Li (Institute of Polymer Chemistry)

SELECTED RESEARCH PROJECTS

- Development of massively parallel force spectroscopy platform
 - Numerically simulated electric field distribution and forces in dielectrophoretic (DEP) tweezers
 - Developed surface chemistry for single molecule arrays in micro-fabricated DNA chips

- Designed and fabricated (using CNC machine and lithography) a setup for fluid cell and microscope
- Calibrated DEP forces using method of hindered diffusion and direct comparison to magnetic tweezers
- Applied DEP tweezers to stretch single DNA molecules for genome sequencing
- Synthesis of functional polymer particles
 - Synthesized various acrylate based co-polymers and characterized them using IR, NMR, and GPC
 - Synthesized magnetic and fluorescent nanoparticles (quantum dots)
 - Synthesized fluorescent superparamagnetic polymer microspheres with tunable surface functionality using membrane emulsification and sono-emulsification
 - Characterized physical properties of thin films using ellipsometry and AFM
- Single molecule arrays on solid surfaces
 - Prepared arrays of single DNA molecule on solid surfaces via competitive binding
 - Characterized single molecule spacing using AFM, ellipsometry, scanning electron microscope (SEM) and single molecule fluorescence
 - Modelled kinetics of DNA attachment and its aggregation on solid surfaces with Monte Carlo simulations
 - Studied adhesion forces between polymer particles and solid surface using AFM and magnetic tweezers binding assay
- Cross-departmental collaborations
 - Polar self-assembly for ultra-fast electro-optical modulation (Collaboration with Dr. Ivan Biaggio and Marten Beels, Department of Physics, Lehigh University, 2012-2013) – Synthesized several variants of dipolar molecules that are electro-optically active and have structures enabling directional self-assembly via hydrogen bonding on covalently modified substrates
 - Isolation of rare cells (Collaboration with Dr. Xuanhong Cheng and Bu Wang, Department of Materials Science and Engineering, Lehigh University, 2010-2012) – Applied DEP tweezers to capture single CD4⁺ T cells for HIV diagnosis
 - Optical properties of polyoxometalate assemblies (Collaboration with Dr. Tianbo Liu and Panchao Yin, Department of Chemistry, Lehigh University, 2009-2012) – Characterized the structure of polyoxometalate assemblies and their fluorescence decay using epi-fluorescent microscopy and AFM
 - Emulsifier-free emulsion polymerization of core-shell nanoparticles for bioanalysis (undergraduate research)

SKILLS

- Synthesis: multi-step organic synthesis, radical polymerization, nanoparticles (metal and metal oxide nanoparticles, quantum dots), multi-functional polymer microspheres (emulsion polymerization, sono-emulsification, and membrane-emulsification methods), carbon nanotubes (chemical vapor deposition)
- Single molecule techniques: single molecule fluorescence, FRET, TIRF, single molecule force spectroscopy, surface modification for covalent and non-covalent attachment
- Thin film characterization: variable angle spectroscopic ellipsometry, contact angle, tensiometry
- Analytical techniques: electrochemistry, photoelectrochemistry, potentiometry, zeta-potential measurements, fluorescence spectroscopy, XPS, GPC, DLS, DSC, FTIR, UV-Vis, NMR, HPLC, GC-MS and LC-MS
- Imaging: atomic force microscopy (AFM), electron microscopy (EM) with EDAX, optical microscopy
- Coding, Programming, and Numerical Modelling: Igor Pro, MATLAB, and COMSOL
- Fabrication: microfabrication (photolithography, oxide and nitride film growth, metal evaporation, self-assembled monolayers, chemical/physical vapor deposition and wet/dry etching), CNC machining
- Standard molecular biology techniques: PCR, gel-electrophoresis, and DNA ligation and end-modification

TEACHING EXPERIENCE

Teaching Assistant: General Chemistry I & II Laboratory (6 semesters, laboratory instruction and grading of lab reports); Physical Chemistry Laboratory (2 semesters, pre-lab lectures, supervising experiments and grading of lab reports).

Mentored three undergraduate researchers in independent research projects.

AWARDS AND HONORS

Newton W. & Constance B. Buch Fellowship (Lehigh University)

Departmental scholarship (Nankai University)

PATENTS

Vezenov, D. V.; **Cheng, P.**; Barrett, M.J.; Oliver, P.M. (Filed 8 August 2012). Dielectrophoretic Tweezers for Massively Parallel Manipulation of Microscopic Objects Suspended in Liquid Medium

PUBLICATIONS

1. Yin, P.; Bayaguud, A.; **Cheng, P.**; Haso, F.; Wang, J.; Vezenov, D.V.; Winans, R.E.; Hao, J.; Li, T.; Wei, Y.; Liu, T. "Directional Hydrogen Bonding Leads to the Formation of Catalytically Active 1-D Nano-belts by Polyoxometalate-Organic Hybrids." (submitted to *Angewandte Chemie*)
2. **Cheng, P.**; Park, J.S.; Cetin, D.; Oliver, P.M.; Lim, H. I.; Vezenov, D. V. "Preparation and Characterization of Magnetic Photoluminescent Polymer Microspheres Using Membrane Emulsification." (in preparation, manuscript available upon request)
3. Oliver, P.M.; **Cheng, P.**; Gajsiewicz, J.; Beren C.; Carrion, E.; and Vezenov, D.V. "Immobilization of Thiolated DNA on Gold Surfaces with Controlled Single-Molecule Spacing." (in preparation, manuscript available upon request)
4. Barrett, M.J.; Oliver, P.M.; **Cheng, P.**; Cetin, D.; and Vezenov, D.V. "High Density Single-Molecule-Bead Arrays for Parallel Single Molecule Force Spectroscopy." *Anal. Chem.*, 2012, 84 (11), 4907-4914.
5. **Cheng, P.**; Oliver, P.M.; Barrett, M.J.; Vezenov, D. V. "Progress toward the application of molecular force spectroscopy to DNA sequencing." (invited paper for special issue) *ELECTROPHORESIS*, 2012, 33 (23), 3497-3505.
6. Yin, P.; Jin, L.; Li, D.; **Cheng, P.**; Vezenov, D. V.; Bitterlich, E.; Wu, X.; Peng, Z.; Liu, T. "Supramolecular Aggregation of Conjugated Polymers Containing POM-terminal Side Chains in Polar and Nonpolar Solvents." *Chemistry – A European Journal*, 2012, 18, 6754-6758.
7. **Cheng, P.**; Barrett, M.J.; Oliver, P.M.; Cetin, D.; Vezenov, D.V. "Dielectrophoretic Tweezers as a Platform for Molecular Force Spectroscopy in a Highly Parallel Format." *Lab on a Chip*, 2011, 11, 4248-4259.
8. Wagner, K.; **Cheng, P.**; Vezenov, D.V. "Noncontact Method for Calibration of Lateral Forces in Scanning Probe Microscopy." *Langmuir*, 2011, 27, 4635-4644.
9. Yin, P.; Wu, P.; Xiao, Z.; Li, D.; Bitterlich, E.; Zhang, J.; **Cheng, P.**; Vezenov, D.V.; Liu, T.; Wei, Y. "A double-tailed, fluorescently active surfactant with hexavanadate as giant polar head group." *Angewandte Chemie*, 2011, 50, 2521-2525.

CONFERENCES

1. Dielectrophoretic Tweezers as a Platform for Biomolecular Analysis in a Highly Parallel Format. (Oral presentation) 244th ACS National meeting, Division of Analytical Chemistry, Philadelphia, PA, August, 2012.
2. Kinetic study of self-assembled thiolated DNA on gold surface with controlled single-molecule spacing. (Oral presentation) 244th ACS National meeting, Division of Colloids and Surface Science, Philadelphia, PA, August, 2012.
3. Dielectrophoretic Tweezers as a Platform for Molecular Force spectroscopy in a Highly Parallel Format. (Oral presentation) 86th ACS Colloids and Surface Symposium, Johns Hopkins University, Baltimore, MD, June, 2012.
4. Dielectrophoretic Tweezers as a Platform for Molecular Force spectroscopy in a Highly Parallel Format. (poster presentation) 38th Northeast Bioengineering Conference, Temple University, Philadelphia, PA, March, 2012.
5. Dielectrophoretic Tweezers as a Platform for Molecular Force spectroscopy in a Highly Parallel Format. (poster presentation) APS March Meeting, Boston, MA, February, 2012.